2012-08-31

Nanoscale Surface Patterning and Applications: Using Top-Down Patterning Methods to Aid Bottom-Up Fabrication

Anthony Craig Pearson
Brigham Young University - Provo

Nanoscale Surface Patterning and Applications: Using Top-Down Patterning Methods to Aid Bottom-Up Fabrication

Anthony Craig Pearson

A dissertation submitted to the faculty of

Brigham Young University

in partial fulfillment of the requirements for the degree of

Doctor of Philosophy

Robert C. Davis, Chair
Gus L. W. Hart
Matthew R. Linford
Richard R. Vanfleet
Adam T. Woolley

Department of Physics and Astronomy

Brigham Young University

August 2012

ABSTRACT

Nanoscale Surface Patterning and Applications: Using Top-Down Patterning Methods to Aid Bottom-Up Fabrication

Anthony Craig Pearson
Department of Physics and Astronomy, BYU
Doctor of Philosophy

Bottom-up self-assembly can be used to create structures with sub-20 nm feature sizes or materials with advanced electrical properties. Here I demonstrate processes to enable such self-assembling systems including block copolymers and DNA origami, to be integrated into nanoelectronic devices. Additionally, I present a method which utilizes the high stability and electrical conductivity of graphene, which is a material formed using a bottom-up growth process, to create archival data storage devices. Specifically, I show a technique using block copolymer micelle lithography to fabricate arrays of 5 nm gold nanoparticles, which are chemically modified with a single-stranded DNA molecule and used to chemically attach DNA origami to a surface. Next, I demonstrate a method using electron beam lithography to control location of nanoparticles templated by block copolymer micelles, which can be used to enable precise position of DNA origami on a surface. To allow fabrication of conductive structures from a DNA origami template, I show a method using site-specific attachment of gold nanoparticles to and a subsequent metallization step to form continuous nanowires. Next, I demonstrate a long-term data storage method using nanoscale graphene fuses. Top-down electron beam lithography was used to pattern atomically thin sheets of graphene into nanofuses. To program the fuses, graphene is oxidized as the temperature of the fuse is raised via joule heating under a sufficiently high applied voltage. Finally, I investigate the effect of the fuse geometry and the electrical and thermal properties of the fuse material on the programming requirements of nanoscale fuses. Programming voltages and expected fuse temperatures obtained from finite element analysis simulations and a simple analytical model were compared with fuses fabricated from tellurium, a tellurium alloy, and tungsten.

Keywords: nanofabrication, block copolymer, DNA origami, graphene, lithography, nanoparticle, nanowire, data storage

ACKNOWLEDGEMENT

With much appreciation I would first like to thank my advisor Dr. Robert Davis for his continuing guidance, patience, and support throughout my graduate experience. The advice he has given and lessons he has taught have been crucial to my learning and will continue to help me in my future career opportunities throughout my life. Next, I would like to acknowledge Dr. John Harb for his commitment to the ASCENT project and for his many useful comments and suggestions which have helped me form ideas and overcome obstacles in my research. I would next like to give thanks to: Dr. Barry Lunt, Dr. Matthew Linford and Dr. Adam Woolley for their useful input which has been extremely helpful in progressing my work and overcoming technical challenges; Dr. Richard Vanfleet and Dr. Jeff Farrer for their help and advice regarding TEM and SEM analysis; Dr. Gus Hart for his useful suggestions regarding the statistical analysis of DNA origami surface attachment; and Dr. Dan Millward of Micron Technology for his guidance during my time working for him as an intern and his willingness to give suggestions and answer questions regarding my own research projects.

Additionally, there have been many students which have given useful discussion and made important contributions to this work. Brian Davis and Dr. Kyle Nelson have given useful advice and discussion which has helped generate many good ideas and promising results. Dr. Jianfei Liu and Elisabeth Pound were instrumental in each of my DNA projects. Specifically, they each played important roles in development of portions of the DNA origami metallization process and provided me with technical expertise for much of my DNA origami work.

Most importantly, I would like to give thanks to my beautiful, loving wife Mary for her extreme patience and support during my time as an undergraduate and graduate student. Without her support and motivation I could not have completed this work. Finally, I would like to thank

my children Maddie, Carson, Austin, and Ryder, who have shown me great love and provided me with further motivation to complete this work.

Contents

List of Figures

Chapter 1

Introduction

Due to their interesting structural, physical, and electronic properties, self-assembled nanoscale materials are desirable tools for fabrication of electronic, photonic, and sensor devices.[1-2] The self-assembled materials could allow fabrication of such devices which are smaller, faster, and longer lasting than current devices.[3-7] However, high yield fabrication processes have yet to be developed which enable such self-assembled nanostructures to be integrated into current devices. In self-assembly processes, which are often referred to as bottom-up processes, chemical or physical interactions cause atoms or molecules to assemble into an organized nanoscale structure. In current fabrication facilities nanoscale fabrication processes use top-down fabrication techniques, which require large expensive instruments to control the size, shape, location, and type of material patterned on a surface.

Currently, optical lithography is the tool of choice to create nanoscale patterns on a surface. In this technique, a pattern is projected from a mask to a surface which is coated first with a material of interest, then with light sensitive polymer known as photoresist (see Figure 1.1). The areas where the photoresist is exposed with light are altered chemically in such a way that the exposed resist can be removed selectively from the areas which were not exposed by rinsing in an appropriate solvent. The photoresist is then used as a mask while a wet or dry etch process is used to transfer the pattern into the material of interest. The remaining photoresist is then removed in an appropriate solvent, leaving a surface pattered with the desired material.

The minimum feature size (W_{min}) of this technique is dependent upon the wavelength of light used (λ) and the numerical aperture (NA) of the lens used to project the light onto the surface as follows:

$$W_{min} = \frac{k_1 \lambda}{NA}, \quad (1.1)$$

where

$$NA = n \sin \theta. \quad (1.2)$$

Here k_1 is a constant dependent upon resist properties (typical values of k_1 range from 0.15 to 0.8), θ is the half cone angle of light entering the lens, and n is the index of refraction of the medium the lens is in (ex. water, oil, air).[8] Advances being made to stretch the limits of projection lithography include: (1) water immersion, which increases the numerical aperture of the lens; (2) phase shift masks, which contain regions with different mask thickness causing the light passing through the mask to have a phase shift from light passing through other regions causing destructive interference with light coming through nearby regions on the mask; (3) proximity correction, where the feature shapes are altered to correct for shape distortion from diffraction from small mask features; (4) multiple patterning, where a mask is exposed once and moved slightly and exposed again to create tightly spaced features; and (5) higher resolution resist development. Implementation of these methods has allowed optical lithography techniques using a 193 nm UV light to create patterns and structures with sizes down to 22 nm as a half pitch. However, it is uncertain whether these techniques will allow continued decrease in feature sizes beyond this limit.[9]

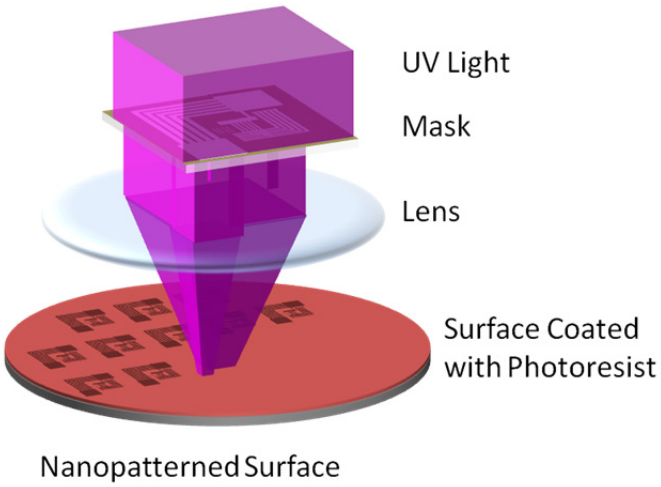

Figure 1.1. Schematic of optical projection lithography. Light is passed through a mask and focused through a lens onto a surface coated with photoresist. The photoresist is chemically changed in locations where it is exposed to the light.

To continue to decrease feature sizes of fabricated nanostructures other methods are being developed as an alternate approach to optical lithography. Many of these techniques are top-down approaches which are not limited by optical diffraction. Some of these approaches which are capable of making sub-20 nm features include: chemomechanical patterning,[10-11] dip pen nanolithography (DPN),[12-13] AFM mechanical scribing and nanoshaving,[14] nanoimprint lithography,[15-16] x-ray lithography,[17] extreme ultra-violet lithography,[18] and electron beam lithography.[19] Despite their ability to create small features, many investigated top-down methods have disadvantages that make them inconvenient for large scale patterning applications. For example, chemomechanical patterning, dip pen nanolithography, AFM mechanical scribing and nanoshaving, and conductive-AFM oxidation use an AFM tip to write the patterns. This requires huge amounts of time for large surface areas to be patterned. This has been addressed by creating arrays of hundreds of tips that can be used in parallel;[20] however, tip wear during patterning, which causes variability throughout the process remains a critical issue. Electron beam

lithography is also slow since it requires the beam to raster over all patterned areas. Nanoimprint lithography is a scalable process which can create features down to 10 nm by forming a pattern in a polymer by pressing a topographically patterned stamp into the polymer at elevated temperatures. Since an imprint stamp can be used repeatedly, it is possible to make a stamp with a slower high resolution patterning technique such as electron beam lithography. As feature sizes are decreased below 10 nm, it becomes difficult to remove the polymer from the stamp without distorting patterns. Additionally, there is difficulty in precisely aligning patterns to existing features on a surface, so the usefulness of nanoimprint lithography may be limited.

As mentioned above, bottom-up methods are also of interest in fabrication of nanoscale structures. Unlike top-down methods, bottom-up processes are controlled by self-assembly via chemical and physical interactions between atoms and molecules.

Examples of proven self-assembly processes that can aid in development of structures and materials for nanofabrication are epitaxy, catalyzed growth (ex. carbon nanotube and graphene growth), self-assembled monolayer formation, block copolymer assembly, and DNA origami. Depending on the nature of the materials used in these processes, self-assembly can either occur on a surface or in solution. In order to be useful in many applications it is important to control the size, shape, location, and orientation of fabricated structures. To date there is no self-assembly process that allows control of each of these simultaneously. However, progress has been made using top-down lithography to direct self-assembly of materials on surfaces.

1.1 Electron beam Lithography

In a research environment electron beam lithography is often used to create patterns with extremely small features. This technique allows researchers to make patterns as small as state-of-the-art optical lithography without needing to buy an expensive projection lithography stepper (up to $100 million). In the electron beam lithography process, first, an electron sensitive polymer (resist) is spin cast from solution onto a surface. Next, the resist surface is exposed to an electron beam by rastering the beam across the surface, which causes a chemical or physical change in the polymer. As in optical lithography, the exposed polymer can then be removed by rinsing in a selective solvent, and depending on the application further processing can be done to transfer the pattern into a desired material.

Electron beam lithography is a powerful tool for nanoscale patterning which has been demonstrated by its ability to produce linewidths below 10 nm.[19] The limitations in the linewidths achievable by electron beam lithography are not limitations in the electron beam itself as electron beams can be smaller than 1 nm in diameter, with the electrons having wavelengths below 10 pm. However, as the beam interacts with the sample there can be electron scattering and emission of secondary electrons causing regions of the resist near the beam to also receive some exposure to electrons. While these electrons are generally lower in energy than the electrons from the beam, they still have potential to expose nearby areas. This effect is dependent upon the energy of the incident electrons and the electron dose (i.e. the time each location is exposed to the beam).

Electron beam lithography can either be done in dedicated electron beam writing tools or many conventional scanning electron microscopes can be modified for this application. Software

and electronics have been developed for doing lithography on SEMs by third parties like J.C. Nabity and Raith. Pattern designs are drawn using conventional CAD design software, which allows versatility in design and enables a quick turn-around time between design and fabrication. However, the main downfall of electron beam lithography is that the patterning time is proportional to the area of the pattern, which means fabrication across entire wafers can take very long, making electron beam lithography not useful as a mass fabrication method. However, it is very useful in research to create processes for creating structures with feature sizes that are also achievable by current optical lithography techniques. Additionally, due to the versatility in the patterns which can be written, in industry electron beam lithography is often used to create patterns on the masks used in optical lithography.

1.2 Controlled Self-Assembly of Nanostructures

Two bottom-up processes which can be used to create controllable sub-10 nm features include: block copolymer (BCP) self-assembly and DNA origami.

1.2.1 Block Copolymer patterning

A BCP is composed of two immiscible polymers bound together with a single covalent bond. Under the right conditions, these blocks will phase separate to form periodic structures.[4, 21-24] The final morphology of the film is dependent upon the length fraction of each polymer block. By increasing the length of a single block the expected morphology can be changed from spherical, to cylindrical, and lamellar (see Figure 1.2).

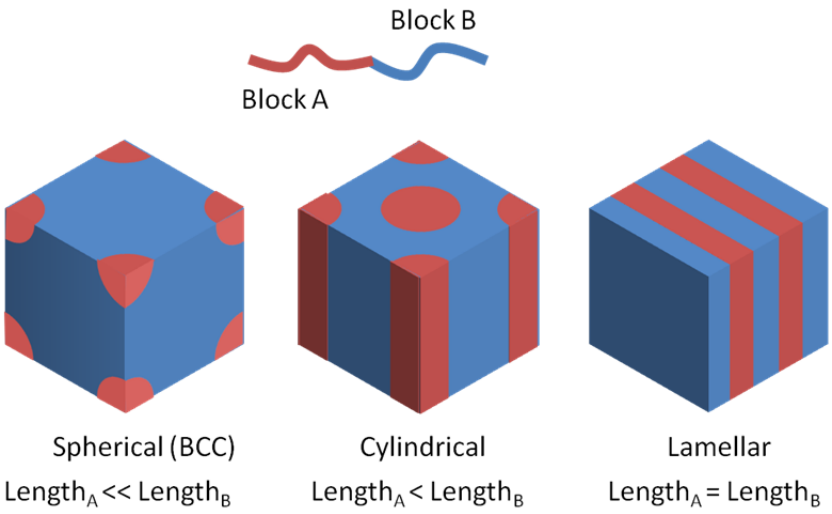

Figure 1.2. BCP bulk morphology based on the length fraction of block A.

When a BCP film is coated on a surface, the interaction energies between the polymer blocks and each block with both the substrate and the atmosphere provide the driving force for the BCP to microphase separate and rearrange into an energetically favorable morphology. Much work has been done to control the orientation of these features with respect to the substrate. For example, BCPs in cylindrical morphologies can arrange so the cylinders are either parallel or perpendicular to the substrate.[23, 25-26] It has been found that cylinders (or lamellae) which are perpendicular to the substrate can be obtained by adjusting the chemistry at the substrate surface so the interfacial energy between the substrate and one of the blocks is the same as the interfacial energy between the substrate and the other block.[27] This allows both blocks to be in contact with the substrate in equilibrium, thus allowing cylinder features to orient perpendicularly to the substrate (see Figure 1.3a-b). Alternatively using solvent annealing with an appropriate solvent allows perpendicular cylinders to form.[28] It is thought that this is due to the gradient in the solvent concentration through the film as it evaporates after removal from the solvent annealing

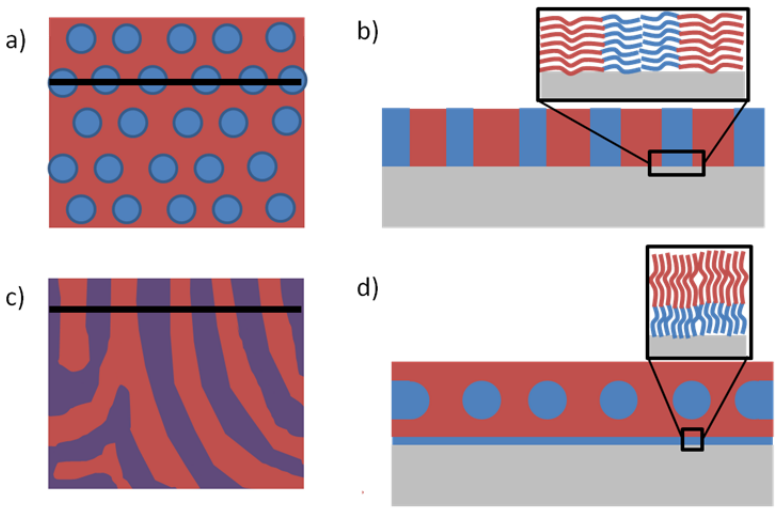

Figure 1.3. Possible orientations of cylinder forming BCPs. a) Shows a top down view of cylinders (blue) which are oriented perpendicular to the surface. b) Shows a cross-section of the surface in (a) along the black line. The inset shows the orientation of polymer chains at the polymer/substrate interface. This orientation occurs when the interfacial energy is equal between the substrate and each polymer block. c) Shows a top down view of cylinders oriented perpendicular to the surface. The purple areas represent the cylinders formed by the blue block beneath a layer of the red block. d) Shows a cross section of the surface in (c) along the black line. Blue circles represent cylinders running perpendicular to the surface. The inset shows the orientation of polymer blocks at the substrate interface. This orientation is obtained by selecting a surface with lower interfacial energy with the blue block than with the red block.

chamber.[29-30] Using appropriate surface and/or environmental conditions cylinders which are parallel can also be obtained as shown in Figure 1.3c-d.

Understanding how to control the orientation of the polymer blocks with respect to the substrate has led to important experiments which have allowed finer control of the direction of BCP pattern orientation on the substrate. One common method to reduce defects and control the orientation of cylinder forming BCPs is known as graphoepitaxy (see Figure 1.4a-c).[23, 31-33] Here a trench can be fabricated into a surface which has lower interfacial energy with block "A" (blue block) of the block copolymer than with block "B" (red block), where it is assumed that the "A" block forms the cylinder portion of a BCP with a cylindrical morphology. When a thin film

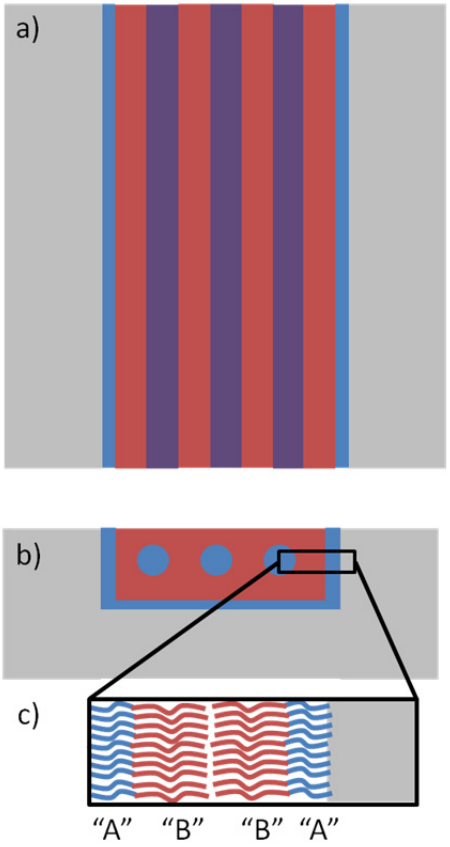

Figure 1.4. A schematic showing graphoepitaxy of cylinder forming BCPs. a) Shows a top down view of cylinders oriented perpendicular to the surface which has assembled parallel with a trench fabricated along the surface (grey). The purple areas represent the cylinders formed by the blue block beneath a layer of the red block. b) Shows a cross section of (a) where the blue circles represent cylinders running perpendicular to the surface. The inset shows the orientation of polymer blocks in contact with the side wall.

of the BCP is coated on the substrate and annealed the blue block wets the substrate, which in turn forces the cylinders to run parallel with the trench wall.

Figure 1.5 shows an example of an alternate method of forming patterns using BCPs. In this method, spherical micelle structures are first formed in solution using a solvent which is selective for one of the blocks. In the presence of a selective solvent it is energetically favorable for the insoluble block to be grouped in the micelle core with the soluble block stretched outward

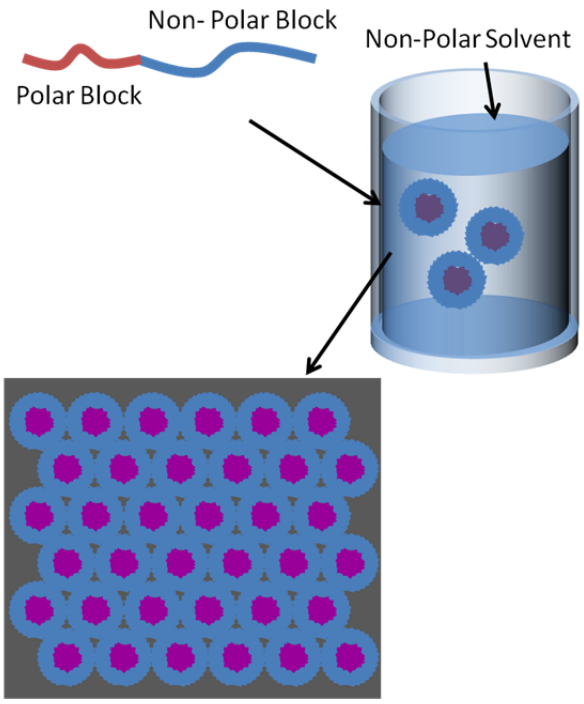

Figure 1.5. BCP micelles are formed in a solvent which is selective for one of the blocks. Micelles are deposited on a surface in a hexagonal array by spin or dip coating. The purple color represents the area where the red block composes the micelle core.

into the solvent, forming the micelle shell.[34] For spherical micelles, the radius of the micelles can be adjusted with the length of the BCP.[35] Spin coating or dip coating can be used to deposit micelles on a surface, which due to their spherical shape, align in a closed packed array on the surface. This method of patterning is interesting since it requires no extra processing such as annealing to form the structures. In addition, for BCPs which self-assemble on a surface it is difficult for larger molecular weight BCPs to reach equilibrium; however, micelle formation is not limited by molecular weight, thus the size of patterns is much more controllable.

In both of these BCP methods one of the main obstacles currently preventing such processes to be used in a manufacturing process is the ability to eliminate defects. Integrated circuit manufacturing requires very precise, defect free patterning. Using surface self-assembly

techniques annealing conditions, alignment to chemical or topographic patterns and polymer selection can help decrease defects, however, it remains difficult to completely remove defects. Since micelle formation is done mainly in solution and the pattern is formed during deposition, there are fewer techniques available which can reduce any defects which occur during assembly; thus, in micelle patterning it is generally more difficult to obtain highly ordered features. However, development of a top-down method to direct micelle placement during deposition may help reduce defects and allow control of micelle location.

1.2.2 DNA origami

In DNA origami, a long (typically > 5000 base) single-stranded DNA molecule (ssDNA) called the "scaffold" is placed in aqueous solution with short ssDNA strands called "staple strands".[36] To form a pattern, the staple strands are predesigned to have base sequences that are complementary with specific locations on the scaffold. Base-pairing between the scaffold and staple strands causes the scaffold to fold into a predetermined shape (see Figure 1.6). A wide variety of 2-dimensional and 3-dimensional shapes can be formed with this method.[37-38] Due to the versatility in the types of shapes that can be formed with this method as well as their nanoscale size it is very interesting as a surface patterning technique. However, since the DNA folding must be done in solution, the ability to create surface patterns with DNA origami relies upon the development of processes that can direct origami surface placement. Additionally, a useful pattern from DNA origami requires the ability to transfer the nanoscale shape made by the DNA origami into a material holding the necessary electronic or other physical properties.

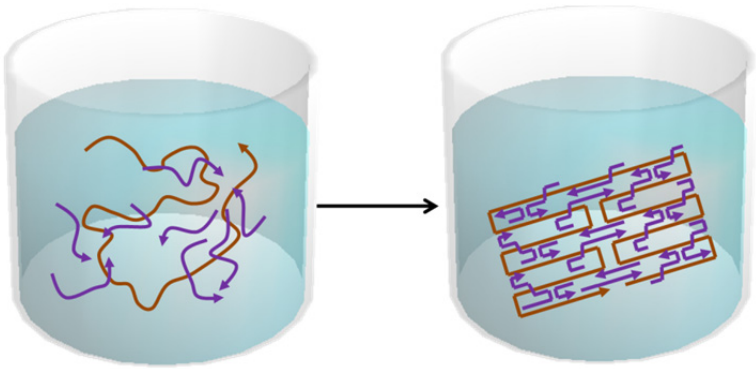

Figure 1.6. Schematic of the DNA origami process. The scaffold strand (brown) is mixed with staple strands (purple) which are each designed to bind with selected portions of the scaffold. Base pairing of the staple strands with the scaffold causes the scaffold to fold into a predetermined shape (a rectangle for example).

Other challenges that may need to be overcome before DNA origami can be incorporated into an integrated circuit fabrication process are that (1) the total surface area of structures is limited because a DNA scaffold strand longer than ~ 10000 base pairs is difficult to form. This means that DNA origami will likely need to be used in combination with another lithographic process to make any larger scale structures which are needed. (2) The flexibility of DNA origami makes precise control of the shape of DNA origami difficult. This could potentially cause defects or malfunctions in electronic devices. (3) Since DNA origami self-assembly occurs in solution, processes must be developed which allow precise placement of DNA origami on an appropriate substrate. (4) Methods must be developed which allow transfer of the DNA origami pattern into an appropriate material for semiconductor devices (metals, semiconductors, etc).

1.2.3 Graphene

Another material of recent interest for fabricating nanoscale electronic devices is graphene. Single layer graphene is composed of a monolayer of sp^2 hybridized carbon atoms, or,

essentially, it is an atomically thin sheet of graphite. Graphene is known for its extremely high electron mobility and electrical conductivity. Additionally, it has good thermal conductivity, an extremely high melting point, and high stability against oxidation.[7, 39-40] These properties make it well suited for electronic devices requiring high stability.

Graphene is generally formed in two manners (1) mechanical exfoliation from a graphite source or (2) chemical vapor deposition (CVD) onto metal substrates, typically copper or nickel. Mechanical exfoliation is done by placing a piece of scotch tape onto a graphite source and removing it, causing a few layers or even a monolayer sheet of graphene to be peeled off the graphite.[41] The material is then removed from the tape and placed on a surface usually in the form of small sheets. These sheets can be incorporated into an electronic device by using lithographic techniques to place the desired electrodes on the surface around the deposited graphene sheet or the graphene sheet can be patterned onto existing electrodes into an appropriate geometry.

CVD is a bottom-up growth technique and allows large sheets of graphene to be formed.[42] This method is shown in Figure 1.7 where a clean metal (generally Ni or Cu) foil is first annealed at temperatures above 700^{o}C in an evacuated furnace in the presence of hydrogen gas to reduce metal oxides on the surface. Next, a carbon based gas such as methane is flowed into the chamber, and the metal surface acts as catalyst to cause carbon atoms from the flow gas to assemble together forming a 2-dimensional sheet of sp^2 hybridized carbon across the entire surface. When a copper substrate is used the reaction is self-terminated after a monolayer graphene film has formed. In this technique graphene nucleation points are formed across the entire surface which grow until they join. Since the crystal orientation of each grain is different

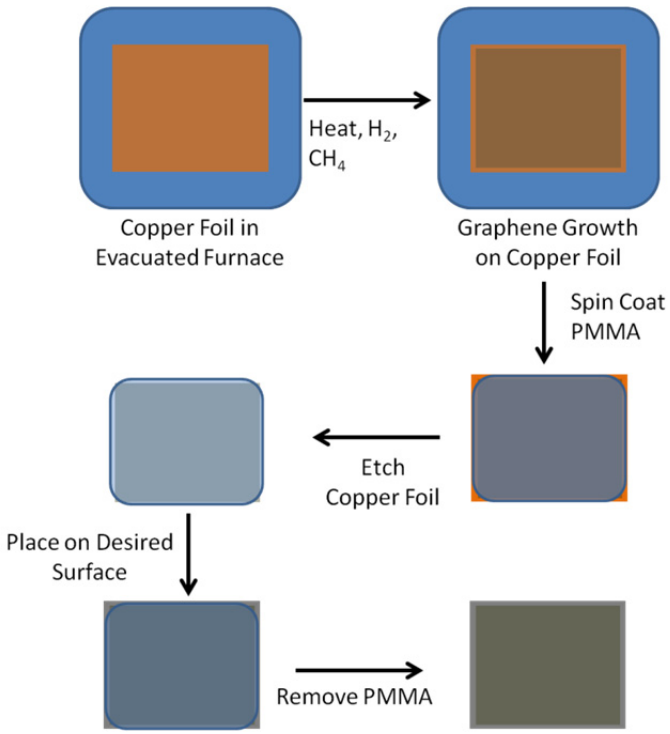

Figure 1.7. Bottom-up graphene growth on copper foil.

there are generally many defects at the boundary where two grains join together. This has been shown to affect the electrical and thermal properties of the film.

Graphene sheets formed by chemical vapor deposition are incorporated into devices by first spin casting a polymer layer on top of the graphene film while it is still attached to the metal foil. The foil is then removed in an etch solution, leaving a free floating polymer/graphene film. The film is then transferred to an appropriate substrate and patterned into the desired geometry using a lithographic technique.

The catalyzed growth method has the advantage of allowing larger graphene sheets to be formed as well as it being a more consistent method to create graphene than the exfoliation method. However, both methods have the disadvantage of needing a transfer step to place the

graphene on an appropriate substrate for electronic device fabrication. This limits the ability to use graphene in a high-volume fabrication facility.

1.3 Top down meets bottom up

Structures formed by bottom-up processes have shown to allow smaller feature sizes (DNA origami and BCP), more complex shapes (DNA origami), or advanced material properties (graphene) for electronic device fabrication; however, each of these processes have limitations preventing them from being brought into production lines. However, for DNA origami and block copolymers these limitations have been addressed by using top-down patterning to direct the location of the self-assembled structure. Using this approach, the benefit of smaller feature sizes available with BCPs and DNA origami is maintained while the control, repeatability, and high yield of top-down methods is utilized. While for CVD grown graphene films, top-down directed patterning is also essential for integrating graphene structures into electronic devices. Examples of the type of control that can be gained for each of these self-assembly processes by implementing top-down techniques are shown in Figure 1.8.

The main difficulty in self-assembly methods is that successful pattern formation is determined by thermodynamics of chemical and physical interactions of molecules, which must be controlled precisely in order to allow the energy of the total system to reach a minimum value, corresponding to a defect free state. This dependence of self-assembly processes on system thermodynamics can hinder the ability to create large areas of defect free structures. Thus self-assembling systems are most successful if there is a large driving force toward the minimum energy state and a minimal energy barrier to reach this state (or systems where the initial state is

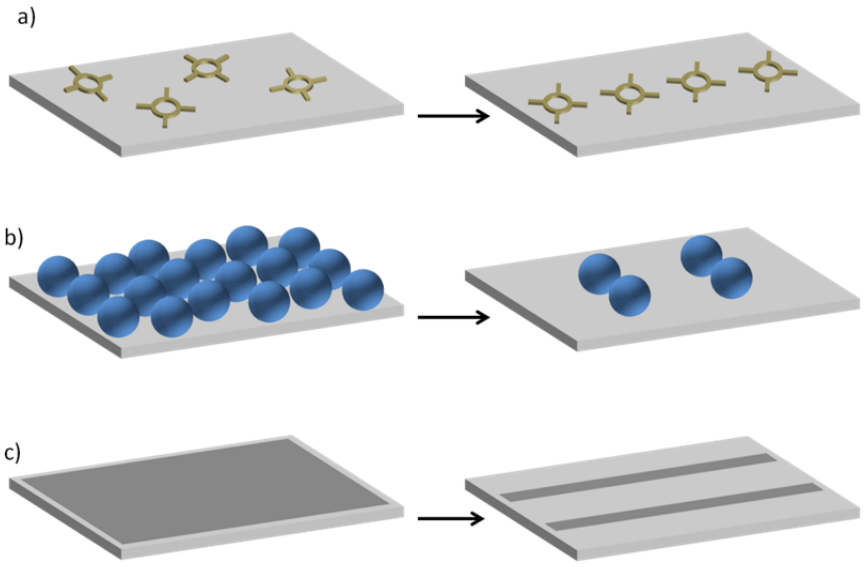

Figure 1.8. Schematics showing examples of resulting structures which can be obtained from bottom-up processes if they are controlled using top-down methods. a) Shows patterning of a possible DNA origami structure. b) Shows patterning of BCP micelles. c) Shows patterning a graphene film.

very unstable). Introduction of top-down patterns to direct the self-assembly process helps reduce defectivity in patterns and is thus essential for precise surface patterning applications.

1.4 Characterization

In order to accurately characterize nanostructures formed by top-down or bottom up methods, high resolution microscopy techniques must be used in order to image structures at the nanoscale. Three particularly useful microscopy techniques are atomic force microscopy (AFM), scanning electron microscopy (SEM), and transmission electron microscopy (TEM). Additionally, highly sensitive surface chemical analysis is important to determine the composition of the materials at each stage of the self-assembly process. A useful tool for

chemical analysis of a surface is x-ray photoelectron spectroscopy (XPS). Each of these analysis techniques are described in detail below.

1.4.1 Atomic Force Microscopy

A schematic of the AFM imaging setup is shown in Figure 1.9. Here an AFM tip is connected to a cantilever, which can be vibrated at its resonant frequency (for tapping mode imaging) by a piezo electric driver. A piezoelectric tube controls the motion of the cantilever and tip in the x, y, and z directions. A laser is reflected off of the cantilever to a 4-quadrant photodiode detector to allow measurement of the change in position of the cantilever during

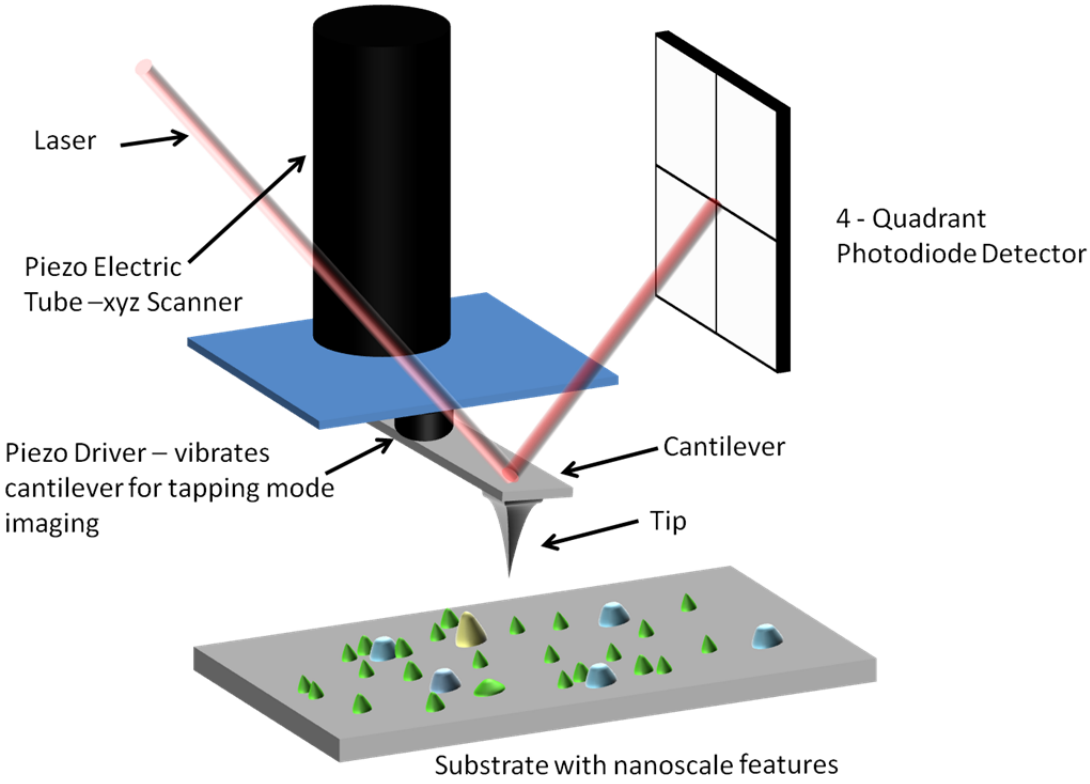

Figure 1.9. Schematic showing the AFM imaging technique.

imaging. Tapping mode is the most common mode of AFM imaging. During this mode the cantilever is vibrated at its resonant frequency and lowered to the sample surface. After the tip contacts the surface it is scanned across the area of interest. The vibration from the piezo driver causes the tip to tap along the surface as it images. As it taps, the photodetector measures the amplitude of tapping motion. As the tip moves across a dip (or bump) in the surface the tapping amplitude increases (or decreases) from the amplitude value set by the user. The piezoelectric tube scanner then lowers (or raises) the tip until the tapping returns to the set amplitude value. The magnitude of movement in the z-direction of the piezoelectric tube scanner is used to map out height data for each location on the surface. Thus the AFM output is three dimensional data of the surface being imaged.

1.4.2 Scanning Electron Microscopy

In SEM imaging, a beam of electrons is focused and scanned across a sample. The structure of the sample can be seen by detecting secondary electrons which are ejected from the surface due to inelastic scattering with the beam electrons. As the surface is scanned, the intensity of secondary electrons ejected from the surface at each location is converted to an image. The intensity of secondary electrons is dependent upon the type of material being imaged. In highly conductive materials more electrons can be emitted than in low conductivity materials; thus, different materials will often have much different contrast in an SEM.

One difficulty in SEM imaging is that it requires a vacuum environment and only can be done on samples which are conductive. For non-conductive samples, beam electrons begin to charge the sample surface. When it gets sufficiently charged the sample begins to repel beam

electrons which makes imaging difficult. Environmental SEMs can overcome these issues to some degree, since they allow vacuum levels to be lower and can more effectively image insulating surfaces.

1.4.3 Transmission Electron Microscopy

In TEM, a beam of high energy electrons is focused on a very thin sample (< 100 nm thick). The beam electrons pass through the sample and are imaged on a phosphor screen or with a CCD camera. Interaction of the beam with the sample allows imaging of the structure of the sample, where the number of transmitted electrons across the sample is affected by the density and thickness of the material. Thus a sample with multiple materials or different thicknesses will have contrast between areas of different composition. In a crystalline sample the diffraction of the electron beam from atomic planes allows determination of the locations of the atoms in the sample.

1.4.4 Comparison of Microscopy Techniques

AFM provides quantitative vertical height data and is therefore advantageous over the electron microscopy techniques for measuring surface roughness and step heights. AFM is often advantageous for imaging soft materials without causing damage to the substrate. A wide variety of samples can be imaged using AFM since it does not require the sample to be conductive as SEM does. Additionally, AFM is not limited to a vacuum environment as with SEM and TEM.

In fact, with AFM, samples can be imaged in a variety of environments such as air, vacuum, or in solution.

SEM provides sub 10 nm resolution, while TEM provides sub-nanometer resolution. Both of these are typically better than can be offered in the x- and y-directions for an AFM, where resolution is hindered by tip size and wear. Additionally, larger surfaces can be analyzed much more quickly with electron microscopy techniques, since the electron beam moves much more quickly than the AFM tip and can scan much larger areas. Movement to different locations on a sample is also much easier with electron microscopy than for AFM since there is no wait time for the tip to be withdrawn and engaged.

In electron microscopy techniques, the resolution of an SEM is not as high as a TEM, but the sample preparation is often much easier since samples are not required to be electron transparent. TEM, however, is highly advantageous if atomic resolution or high resolution chemical analysis is needed.

1.4.5 X-ray Photoelectron Spectroscopy

In x-ray photoelectron spectroscopy, a beam of monochromatic x-rays interact with the sample to be analyzed. The x-rays cause ejection of electrons from the surface of the sample. The photoelectrons are then analyzed by collection in a hemispherical electron energy detector. From the beam energy and measured kinetic energy of the photoelectrons, the binding energy of the electrons in the solid is calculated. Each element has different electron energy levels, thus with the measurement of electron energies the chemical composition of the sample can be

determined. Additionally, shifts in peaks from the expected binding energy values can be used to estimate the oxidation state of the elements of interest.

1.5 Summary of Accomplishments

In the work presented here I show fabrication methods which I have developed to allow the properties of self-assembled materials to be utilized in nanoscale device manufacturing. In chapter two I discuss a technique I have developed using BCP patterned nanoparticles as templates for surface attachment of DNA origami. Briefly, in this work I used BCP micelles to pattern periodic arrays of gold nanoparticles. The gold nanoparticles were then chemically modified to allow DNA origami attachment. This system allowed analysis of DNA origami binding to sites which were smaller than the minimum feature size of the DNA origami, which had not previously been achieved. To study the binding I used statistical analysis to determine that steric hindrance decreases the probability that multiple origami will attach to one gold nanoparticle. This work resulted in the following publication:

> Anthony C. Pearson, Elisabeth Pound, Adam T. Woolley, Matthew R. Linford, John N. Harb, Robert C. Davis; Chemical Alignment of DNA Origami to Block Copolymer Patterned Arrays of 5 nm Gold Nanoparticles; *Nano Letters*, 2011, 11 (5), 1981–1987.

In chapter three I discuss a technique which I have developed which allows control over the location of BCP micelle patterns. With this method single file lines, double lines, oval patches, and pairs of two particles have been shown to be able to be patterned where the location of the patterned was defined by electron beam lithographic patterning on a surface prior to micelle deposition. This work is valuable since it allows the most accurate patterning of BCP micelle arrays of any method to date. It is expected that attachment of DNA origami to the resulting

patterned nanoparticles will allow control of the location and orientation of DNA origami on the surface. This work is being prepared for submission to Langmuir. It will be titled as follows:

> Anthony C. Pearson, Matthew R. Linford, John N. Harb, Robert C. Davis; Block Copolymer Micelle Templated Nanofabrication on an Electron Beam Patterned Polyacrylic Acid Surface; *Langmuir*, in preparation.

In chapter four I discuss a technique which I have developed jointly with graduate students in the Chemical Engineering and Chemistry departments at Brigham Young University which allows site-specific metallization of DNA origami. This is done by attaching gold nanoparticles in solution to select locations on DNA origami. Next, the Au NPs are plated in an Au electroless plating bath until they grow sufficiently large and begin to fuse together. I have conducted electrical measurements to determine the conductivity of the DNA origami templated nanowires formed from this method. This work was important because it was the first demonstration of conductive nanowires fabricated on DNA origami. This work resulted in the following publication:

> Anthony C. Pearson, Elisabeth Pound, Jianfei Liu, Bibek Uprety, Adam T. Woolley, Robert C. Davis, John N. Harb; Site-Specific Metallization and Electrical Characterization of Conductive Nanowires Templated on DNA Origami; accepted to the Journal of Physical Chemistry B. Published online May 2012.

In chapter five I discuss work which I have done to use CVD graphene films for archival data storage devices. For these devices graphene films were patterned into a nanofuse geometry, where joule heating caused the graphene in the fuse to be heated until oxidation of the graphene occurred. Following oxidation electrical conductivity was lost across fuses. A study was performed to show the effect of fuse geometry on the applied voltage and power necessary for oxidation to occur. Additionally, tests were performed to determine the long term stability of the graphene devices. This work has been submitted for publication.

Anthony C. Pearson, Sarah Jamieson, Matthew R. Linford, Barry M. Lunt, and Robert C. Davis; Chemical Oxidation of Graphene Nanofuses for Long Term Write-Once-Read-Many Times Data Storage; *Nano Letters*, submitted.

In chapter six I discuss work that I have done to theoretically predict the performance of nanoscale fuses for solid state data storage. I have used finite element analysis as well as analytical solutions to determine the effect of fuse material properties and fuse geometry on the voltage and temperature required to program a fuse for long archival data storage. In the analytical solution I used Joule's law and Ohm's law to obtain the power flowing into the fuse from Joule heating and Newton's law of cooling was used to obtain the heat flowing out of the center of the fuse. In the steady state condition the power flowing out equals the power coming in. This was used to find the fuse temperature based on the fuse geometry, applied voltage, and fuse material. In finite element analysis simulations, I used the joule heating package in COMSOL Multiphysics, where I defined the fuse geometry, fuse material, and applied voltage to simulate the expected fuse temperature. This work was written up in three conference proceedings.

Anthony C. Pearson, Bhupinder, Singh, Matthew Linford, Barry Lunt, Robert Davis; Fabrication and Characterization of Nanoscale Tellurium Fuses for Long Term Solid State Data Storage; Nanotech Conference Proceedings; June 2012;

Anthony C. Pearson, Bhupinder, Singh, Matthew Linford, Barry Lunt, Robert Davis; The Effect of Geometry on Nanoscale Tellurium Fuses for Solid- State Data Storage; ISOM'12; Sept. 2012.

Anthony C. Pearson, Bhupinder, Singh, Matthew Linford, Barry Lunt, Robert Davis; The Materials Study of Nanoscale Fuses for Solid State Data Storage; ISOM'12; Sept. 2012.

In chapter 7 I provide a summary of the major contributions and advancements in self-assembly fields from the work discussed in chapters 1-6. Additionally, I provide details about important considerations and direction for future work which can be done to further progress the goal of integrating self-assembly processes into nanoscale device manufacturing.

Chapter 2

Chemical Alignment of DNA Origami to Block Copolymer Patterned Arrays of 5-nm Gold Nanoparticles

2.1 Introduction

The ability to pattern surfaces with feature sizes less than 20 nm remains a major challenge of lithography, with no proven optical solution.[9] Bottom-up processes are an interesting option due to their ability to create patterns with feature sizes far below current optical methods. In these controlled systems, fundamental interactions cause molecules to self-assemble into organized structures. Two such self-assembly methods are block copolymer (BCP) patterning and DNA origami. BCPs can create highly regular features on surfaces, but the types of features are limited to arrays of dots or parallel lines.[21, 31, 43] In contrast, DNA origami is capable of creating a broad range of shapes in solution,[36-37] but DNA origami-based surface patterning relies on the development of processes allowing controlled placement of DNA origami on a surface.

Recently, selective DNA origami surface placement has been demonstrated using binding sites which are large compared to the DNA origami feature sizes. In a report by Kershner et al. DNA origami were placed selectively by using optical and electron beam lithography to pattern hydrophilic regions where DNA origami adsorbed with higher stability than on the hydrophobic background.[44] Following a surface rinse, DNA origami remained selectively within the hydrophilic patterns. Gerdon et al. functionalized e-beam patterned gold pads placed with 11-mercaptoundecanoic acid, which binds ionically with magnesium ions in the DNA origami solution.[45] In this case, the Coulomb attraction between DNA origami and magnesium ions caused selective DNA origami deposition. Ding et al. covalently attached DNA origami to a

surface by using consistently spaced 60 and 80 nm diameter gold islands made by e-beam lithography.[46] DNA origami nanotubes which were modified by addition of thiol functionalized staple strands near each end, were attached between gold island pairs. This method allows orientation control of DNA origami by alignment with the patterned gold islands.

The ability to align DNA origami accurately on a surface is dependent on the binding mechanism and the binding site geometry. Weak attachment mechanisms allow enough mobility for the DNA origami to align with larger binding sites, but more stable attachment mechanisms do not provide such mobility. In state-of-the-art optical lithography, the alignment tolerance is much less than the smallest feature size of the pattern. To achieve both alignment accuracy comparable to lithography and a highly stable attachment, binding sites must be smaller than the minimum DNA origami feature size, which could be as small as 2, 5, or 8 nm for 1, 2, or 3 rows of double helices in planar geometries, respectively, where the alignment accuracy cannot be better than the size of the binding site. Examples of DNA origami structures with feature sizes in this range are DNA origami nanotubes[47] and thin branched structures, which was shown previously by the ASCENT group.[38]

Here the focus is to study for the first time the chemically directed assembly of DNA origami to nanoscale binding sites and specifically to chemically functionalized BCP generated nanoparticles. BCP nanoparticles present an attractive test bed for this study since the minimum BCP surface feature size is a good fit to origami binding site requirements. I also analyze the results to determine the effects of steric hindrance on multiple origami attachment to a single BCP nanoparticle.

BCPs can self-assemble into periodic domains which are a few nanometers to tens of nanometers across and spaced between tens and hundreds of nanometers.[48] Additionally, the

location and orientation of BCP patterns can be controlled by alignment to chemical or topographic features patterned by top-down methods.[4, 21, 31, 43, 49-51]

A well known method of DNA attachment uses thiol functionalized single-stranded DNA (ssDNA-SH) reacted with Au and base paired with complementary ssDNA in solution.[52-53] This interaction has been used previously to attach gold nanoparticles (AuNPs) to DNA origami, where ssDNA functionalized AuNPs base paired with selected staple strands which had been extended with a complementary sequence.[54-55] This base paired attachment method provides a stable, chemically specific binding mechanism to attach DNA origami to BCP patterns, since BCPs can be used to control the location of gold features on a surface. As an example, Chai and Buriak have shown incorporation of metal ions from a dilute HCl solution into the poly-2-vinyl pyridine (P2VP) domain of a self-assembled polystyrene-b-poly-2-vinyl pyridine (PS-P2VP) film.[23] Park et al. showed selective gold incorporation into the P2VP domain in a self-assembled PS-P2VP film through surface reconstruction in ethanol, evaporation of Au onto the surface, and surface recovery by heating.[26] In each example a plasma etch was used to remove the polymer, leaving behind patterned arrays of metallic features in the place of the P2VP block. Here the Au/ssDNA-SH reaction was used in combination with 5 nm BCP patterned AuNPs to chemically direct the placement of DNA origami.

2.2 Methods

A process schematic of the BCP patterning and DNA origami attachment methods used here is shown in Figure 2.1. Here patterned AuNPs are formed from spherical BCP micelles in solution (Figure 2.1a).[34, 51, 56] A gold salt ($HAuCl_4$) is added and migrates selectively to the micelle core

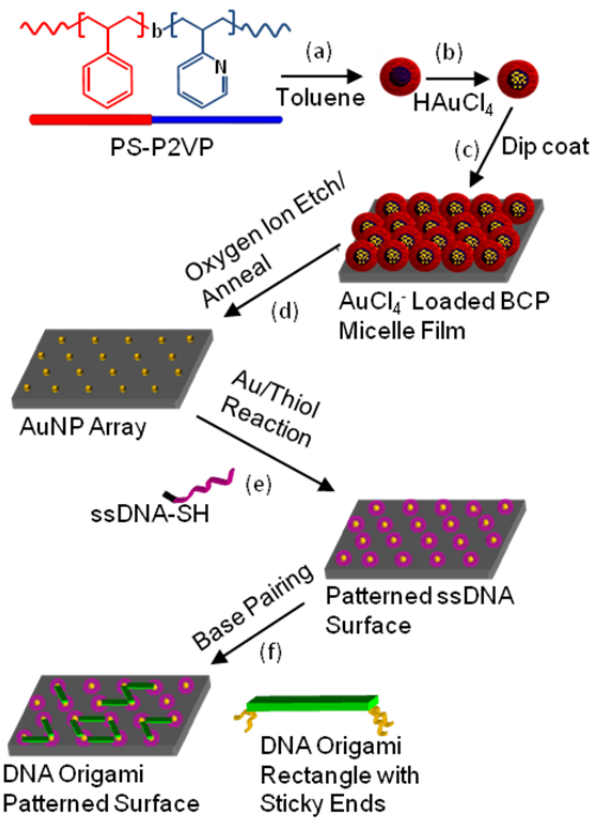

Figure 2.1. Process schematic showing DNA origami attachment using BCP micelle patterning. (a) Polystyrene-b-poly-2-vinylpyridine (PS-P2VP) micelles are formed in a toluene solution. (b) Gold salt is added to the solution and migrates to the center of the micelles. (c) Dip coating causes micelles to arrange in a close-packed monolayer on the surface. (d) Surfaces are placed in O_2/ Ar plasma to remove the polymer and annealed, leaving an AuNP lattice. (e) Next, the AuNPs are functionalized with an ssDNA-SH thiol. (f) Finally, DNA origami, which have been modified with sticky ends by extending appropriate staple strands on each end, are placed on the surface, where the modified staple strands base pair with the ssDNA-SH.

(Figure 2.1b). Micelles are then dip coated onto a SiO_2 surface in a close-packed monolayer (Figure 2.1c). The polymer film is removed and pure AuNPs are formed when the surface is exposed to oxygen plasma followed by a subsequent high temperature anneal (Figure 2.1d). Next, the AuNPs are reacted with ssDNA-SH, creating a patterned ssDNA surface (Figure 2.1e). Finally, a drop of solution containing DNA origami rectangles with complementary sticky ends was placed on the surface to allow base pairing (Figure 2.1f).

Here the BCP micelle method is used to pattern 5 nm AuNPs with an average center-to-center particle spacing of 62 nm. A DNA origami rectangle, 64 nm in length and 11 nm in width was modified with ssDNA at each end (sticky ends) by extending selected staple strands with a 10-base (3.3 nm in length) poly-adenine chain. Attachment studies were performed by functionalizing patterned AuNPs with ssDNA-SH (8-base poly-thymine), which is complementary to the origami sticky ends and exposing DNA origami to these surfaces and to several control surfaces. Results showed high attachment selectivity, where greater than 200 times more DNA origami were attached to surfaces patterned with complementary ssDNA-SH. On these surfaces, up to 74% of the AuNPs formed an attachment with a DNA origami rectangle.

My experimentation has suggested that proper surface preparation is vital in avoiding non-specific DNA origami attachment. It was observed that DNA origami exposed to clean, hydrophilic SiO_2 could be rinsed from the surface. However, contaminated surfaces allowed adsorption of DNA origami. Thus, surface cleanliness was maintained throughout each process step. Initial cleaning was done on 1 cm^2 silicon pieces using RCA standard cleans 1 and 2. The clean surfaces were dipped into and withdrawn from a $AuCl_4^-$ loaded micelle solution[34] at a rate of approximately 75 μm/s. Surfaces were then exposed to an oxygen plasma (40 W, 50 mTorr) followed by a hydrogen anneal.

To functionalize AuNP arrays, the thiols were reduced by reaction with 4 mM TCEP in water held at 40^{o}C for 2 hours. The reduced ssDNA-SH solution (10 μM) was then purified by dialysis using a slide-a-lyzer 3.5K MWCO mini dialysis unit. The solution was dialyzed for a total of 2 hrs, with the solution being exchanged with fresh 0.5X TBE buffer (44.5 mM Tris, 44.5 mM boric acid, 1 mM EDTA, 50 mM NaCl) every 30 minutes. Surfaces patterned with non-complementary ssDNA were formed by reacting AuNP arrays with a 25-base ssDNA-SH (see

supplementary information), while patterned complementary ssDNA surfaces were formed by functionalizing AuNP arrays with an 8-base poly-thymine ssDNA-SH. In both cases, the AuNPs were functionalized by placing a drop of the dialyzed ssDNA-SH solution on the patterned surfaces and incubated for 18 hours.

DNA origami rectangle structures were prepared as previously reported,[38] using 4 extended staple strands. Briefly, purified single-stranded scaffold was mixed with staple strands in a 1:10 molar ratio in 1X TAE-Mg^{2+} buffer (40 mM Tris, 20 mM acetic acid, 1 mM EDTA, 12.5 mM magnesium acetate). The DNA origami was folded by denaturing (95^{o}C for 3 min) and slowly annealing from 75^{o}C to 4^{o}C in 70 minutes.

Following DNA origami preparation filtration was required prior to surface attachment. The solution was filtered with 30 kDa Amicon ultra-0.5 mL centrifugal filters to remove excess staple strands. Following preparation of the patterned ssDNA surfaces, a 30 μL drop of approximately 2 nM DNA origami solution was placed on the surfaces at room temperature to allow hybridization. During all reactions surfaces were placed on an inverted glass dish in an enclosed container with enough standing water to keep solutions from evaporating. Following all reactions, surfaces were rinsed thoroughly in Millipore water and dried in a stream of air.

2.3 Results and Discussion

In initial experiments, $AuCl_4^-$ loaded micelle surfaces were etched in a plasma containing 25% O_2 and 75% Ar for 10 minutes and annealed in hydrogen (1.5 hours, 200^{o}C). Upon exposure to an alkanethiol solution, AFM results showed either a decrease in nanoparticle height or complete removal of nanoparticles from the surface. However, this decrease in height was not seen in

samples where the etch time was increased to 30 minutes. X-ray Photoelectron Spectroscopy (XPS) was used to analyze surfaces coated with $AuCl_4^-$ loaded micelle films that had been plasma etched for 10 and 30 minutes, and annealed for 1.5 hours in H_2 at 200°C. These surfaces were analyzed along with a control film, which had not been etched or annealed. XPS results of surfaces etched for 0, 10, and 30 minutes are displayed in spectra (a), (b), and (c) of Figure 2.2, respectively. In spectrum (a) ($AuCl_4^-$ micelle film), XPS shows a peak at 87.5 eV, indicating that the gold is in a highly oxidized state, as expected for gold chloride. Additionally, a smaller peak is seen in spectrum (a) with a lower binding energy than the gold chloride peak. This indicates that some reduced gold exists in the micelle core as seen in previous reports.[56] Spectrum (b) (10 minute plasma plus anneal) shows a peak at 84.5 eV, and spectrum (c) (30 minute plasma plus anneal) gives a peak at 84 eV, the expected binding energy of Au $4f_{7/2}$ electrons. Surfaces prepared as in spectrum 3 showed much higher stability during an alkanethiol reaction, as measured by AFM. Generally, a height increase was seen after reaction with thiol.

It is expected from reference [56] that a short (~ 2 min) oxygen plasma treatment converts the gold salt to a single gold oxide particle, which can be easily reduced to elemental gold in an annealing process. The XPS data confirms removal of gold chloride from plasma etched surfaces since the gold chloride peak (87.5 eV) shown in spectrum (a) of Figure 2.2 is absent in spectra (b) and (c). Additionally, survey scans show a clear Cl 2p peak in the un-etched sample and no peak on either surface which had been plasma etched. It also appears that the gold oxide was effectively reduced before XPS since there is no peak seen at 87 eV, the expected peak position for Au_2O_3.[57] However, despite the apparent reduction to elemental gold, the peak in spectrum (b) of Figure 2.2 is shifted by 0.5 eV from the bulk gold value. Since reference [58] shows a peak shift of 0.5 eV or greater in XPS spectrum of AuNPs < 2 nm, the shift is likely caused by formation of clusters

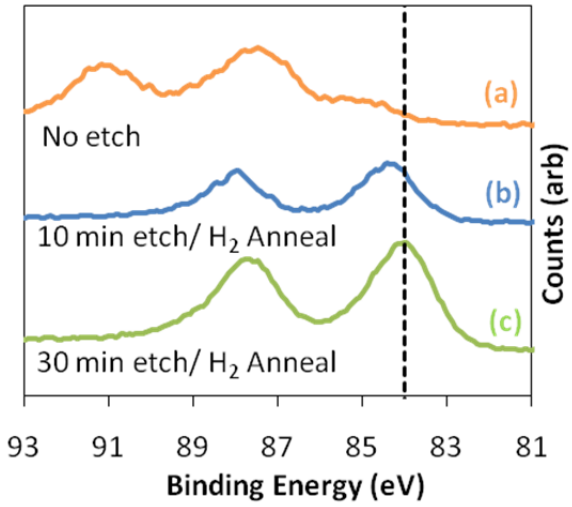

Figure 2.2. XPS spectrum on BCP micelle patterned surfaces. The expected location of the Au $4f_{7/2}$ peak (84 eV) is marked by the dashed vertical line. Spectrum a shows the XPS data of an $AuCl_4^-$ loaded BCP micelle film, with peak position at 87.5 eV. Spectrum b shows data of a $AuCl_4^-$ loaded BCP micelle film plasma etched for 10 min. with a subsequent hydrogen anneal (200°C, 1.5 hours). Spectrum c shows data of an $AuCl_4^-$ loaded BCP micelle film after a 30 minute plasma exposure and a hydrogen anneal (200°C, 1.5 hours).

of smaller gold particles during the 10 minute plasma etch process. Since clusters are likely less stable on the surface than a single particle, this could explain the particle height decrease during thiol reaction. This shift is not seen in spectrum (c) of Figure 2.2, showing that the 30 minute plasma exposure time allowed formation of single gold particles. Although a short oxygen plasma etch was sufficient in reference [56], the plasma system used here required 30 minutes; it is clear that the plasma time must be adjusted for differing plasma systems to ensure complete formation of single AuNPs.

Surface attachment experiments were done by exposing rectangular DNA origami to the patterned complementary ssDNA surfaces and SiO_2 controls for times varying from 30 to 240 minutes. AFM imaging was done on each surface following the reaction with DNA origami. For patterned complementary ssDNA surfaces, results show an increase in the DNA origami

surface concentration from 90 to 230 DNA origami/μm^2 over the investigated reaction period (see Figure 2.3). However, the DNA origami surface concentration on SiO_2 controls was independent of reaction time, with nearly 1 DNA origami/μm^2 for all reaction times (see Figure 2.3e). The attachment yield, which is defined as the percentage of AuNPs having at least one DNA origami attached, on patterned complementary ssDNA surfaces increased from 31% for the shortest reaction time to 74% for the longest reaction time, and the trend in Figure 2.3e indicates that higher yields may be achieved by increasing the reaction time further. Interestingly, analysis of AFM data showed that over 90% of DNA origami had attached between two AuNPs, while the remaining DNA origami had only attached to one AuNP. This shows that enough rotational freedom is maintained following the binding of a single end of the DNA origami that the DNA origami is generally able to bridge and bind between two AuNPs.

Control experiments were used to probe the attachment mechanism. The following three DNA origami/surface combinations were used: (1) DNA origami deposited on a SiO_2 surface, (2) DNA origami deposited on a patterned non-complementary ssDNA surface, and (3) DNA origami with no sticky ends deposited on a patterned ssDNA surface. These experiments were performed by exposing surfaces to a solution containing ssDNA-SH, where the 8-base poly thymine-thiol was used in all controls except the patterned non-complementary ssDNA surface (in this case the 25-base ssDNA-SH was used). The surfaces were then exposed to DNA origami for 4 hours. The controls were run in parallel with a patterned complementary ssDNA surface, where base paired attachment of the DNA origami was expected. AFM analysis showed similar low DNA origami surface concentrations for all control surfaces (see Figure 2.4a-c). The number of attached DNA origami was approximately 200 times greater on the surface with base

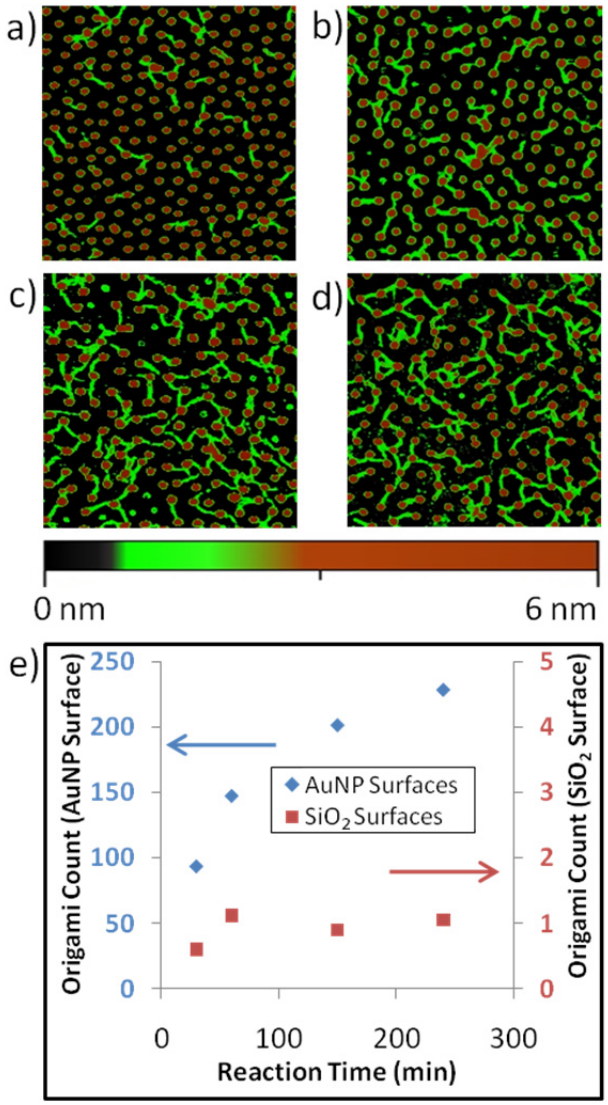

Figure 2.3. a)-d) Tapping mode AFM images of DNA origami on patterned complementary ssDNA surfaces. Reactions were carried out for 30, 60, 150, and 240 minutes for a), b), c), and d) respectively. e) Shows the DNA origami surface density (DNA origami/μm^2) on patterned complementary ssDNA surfaces and SiO_2 controls for all reaction times. The right axis shows the DNA origami count for the SiO_2 surface, while the left axis shows the DNA origami count for the AuNP surfaces. Images in a) – d) are 750 nm on each side. A custom height scale, displayed below (c) and (d), is used to show DNA origami rectangles more clearly.

paired attachment than on control surfaces with non-specific attachment. As earlier noted, substrate cleanliness is the most important parameter to control non-specific DNA origami attachment on SiO2 surfaces. By maintaining clean SiO2 surfaces and using vigorous rinses in

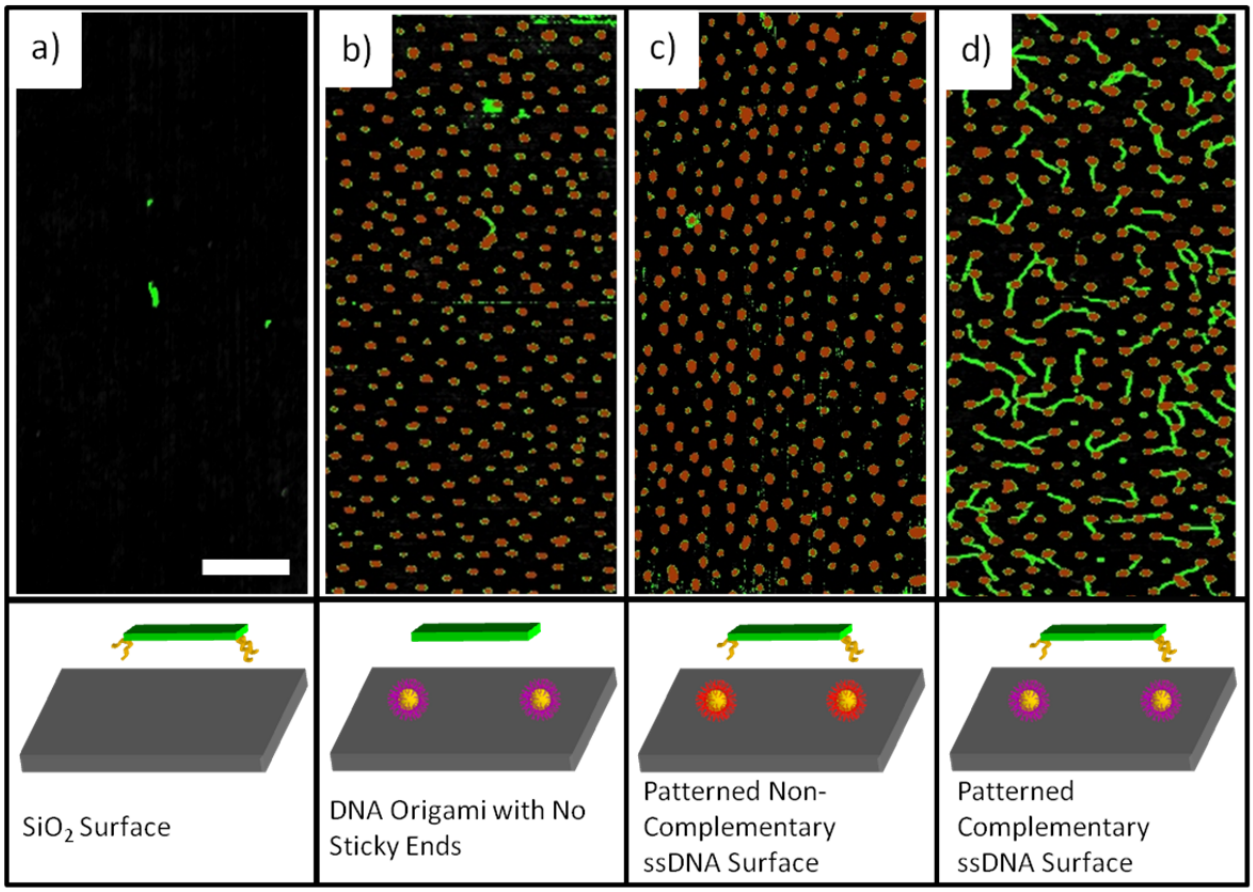

Figure 2.4. Control experiments used to probe the mechanism of DNA origami attachment. a) Sticky end modified DNA origami were placed on a clean SiO_2 surface. b) Non-modified DNA origami rectangles were placed on a patterned ssDNA surface. c) Sticky end modified DNA origami were placed on a patterned non-complementary ssDNA surface. d) Modified DNA origami were placed a patterned complementary ssDNA surface. All reaction times were 4 hours. The scale bar is 200 nm and applies to all images. Here the height scale is the same as in Figure 2.3.

water after both the thiol reaction and the DNA origami reaction only 1 non-specifically attached DNA origami/μm^2 was seen on control surfaces for all investigated reaction parameters.

As mentioned above, AuNPs formed using the optimized plasma and annealing conditions are generally stable during the thiol reaction. Successful binding of ssDNA-SH on these surfaces was verified by the highly selective attachment of DNA origami to ssDNA-SH reacted AuNP surfaces. The physical and chemical stability of the base-pair or thiol attachments have not been thoroughly investigated; however, the ability of the DNA origami to remain on the surface

following the vigorous rinsing technique shows that the overall attachment is fairly robust. The AuNPs are generally very difficult to remove from the surface even by sonication. However, some samples did show some instability as seen in Figure 2.3b-c where there are a few open areas where AuNPs have been removed from the surface. Perhaps on these surfaces some particle clusters had not yet combined into single AuNPs during the plasma process.

While the BCP patterns here exhibit some order, a high degree of order and alignment can be achieved by forming BCP arrays on lithographically patterned surfaces.[4, 21, 23, 31, 43, 48-50] The formation of highly ordered BCP nanoparticle arrays was not the intent here; instead, the focus of this work was to study the attachment of DNA origami to nanoscale binding sites, specifically BCP generated nanoparticles.

Using BCP micelle patterning I have shown alignment of DNA origami between nearest-neighbor pairs of 5 nm AuNPs. Previous methods using a strong chemical binding mechanism do not allow attachment of DNA origami to pairs of binding sites which are less than 60 nm in diameter,[46] due to a low probability of the DNA origami finding and binding with smaller sites. In this method, alignment of DNA origami with the 5 nm ssDNA patterns is possible since block copolymer patterning forms binding sites with both small size and close spacing. This gives a high enough density of available binding sites to make it probable that DNA origami will interact and bind with the patterned ssDNA.

In AFM data, binding of multiple DNA origami to a single AuNP is often seen. In fact, a 4:5 ratio of DNA origami to occupied AuNPs (considering only AuNPs with at least one DNA origami attachment) was seen consistently on surfaces prepared as in Figure 2.4d. A 1:2 DNA origami to occupied AuNP ratio is expected if all binding sites contain only one attachment. While multiple binding could be useful in some applications, it could also be problematic. It is

possible that multiple binding is limited by the steric hindrance between DNA origami in solution and an occupied AuNP. Here the influence of steric hindrance on multiple binding is analyzed by comparing binding statistics obtained from AFM data to a standard "balls in boxes" statistical distribution used to calculate the expected number of attachments per binding site if DNA origami binding is completely random (i.e., not affected by the presence of other DNA origami). If the attachment is random, the probability, P, that a given binding site will be attached to J DNA origami is given by:

$$P = \binom{N}{J} \frac{(M-1)^{N-J}}{M^N}$$

Two types of binding events were analyzed: (1) the attachment of one end of a DNA origami to an AuNP and (2) the attachment of a DNA origami between a pair of AuNPs. The binding site in case (1) is a single AuNP, while in case (2) the binding site consists of a pair of nearest neighbor AuNPs. Thus, for case (1) M is the total number of AuNPs, and N is the total number of DNA origami attachments to AuNPs; and for case (2) M is the total number of nearest neighbor AuNP pairs, and N is the number of DNA origami attached between particle pairs. The values of N and M were obtained by counting AuNPs and attached DNA origami on AFM images of samples prepared as in Figure 2.4d. The expected number of binding sites with J attachments was obtained by multiplying the probability distribution, P, by the total number of binding sites, M. Comparison of experimental data with the random attachment (RA) distribution for cases (1) and (2) is shown in Figure 2.5a and Figure 2.5b, respectively. Figures 5c-d show a subtraction of the RA distribution from experimental results for each value of J in figures 5a-b, respectively.

A possible problem in comparing this statistical distribution with the DNA attachment results is that it assumes each binding event to be random and equally likely to occur at any

binding site on the surface. For case (1) each DNA origami accounts for two binding events, which are constrained to occur between nearest neighbor AuNPs. To determine if the model can truly predict random attachment for case (1), it must be determined whether the nearest neighbor attachment constraint causes any given AuNP to be more likely to receive an attachment. For convenience I will define two types of binding events. Binding event (a) is the case where one end of a DNA origami attaches to an AuNP while the other end of the origami remains free, and binding event (b) is the second end of a DNA origami attaching to a nearest neighbor AuNP (both ends of the DNA origami are attached following binding event (b)). A lattice of K AuNPs, labeled 1 through K is considered. Here $P_a(m)$ and $P_b(m)$ will be called the probability that the m^{th} AuNP, where $1 \leq m \leq K$, will undergo binding event (a) and (b), respectively, and $P_a(mNN)$ is the probability that one of the nearest neighbors to the m^{th} AuNP will undergo binding event (a). Assuming that each AuNP has 6 nearest-neighbors, $P_a(mNN) = 6P_a(m)$ and $P_b(m) = \frac{1}{6}P_a(mNN)$. This leads to $P_b(m) = P_a(m)$.

The above analysis assumed that all AuNPs have 6 nearest neighbors. Defects in the hexagonal lattice will change the number of nearest neighbors for some sites which could result in a different statistical distribution. Simulations were performed to determine the impact of defects on the statistical distribution, which showed that it did not vary significantly from the RA distribution until the defect density was greater than 50% (see supplementary information for details). As the defect density in my system is much less than this, the RA distribution is a reasonable model for case (1).

In case (2), an imperfect lattice could also affect the applicability of the RA distribution since DNA origami may be more likely to attach between optimally spaced AuNP pairs. However, evidence for this is not seen in the AFM data since binding between particles appeared to be

relatively insensitive to particle separation as origami was seen to bind to particles spaced from 35 to 75 nm. Additionally, in cases where DNA origami were only attached on one end nearly all had a nearest neighbor within a reasonable attachment range. Thus it can be assumed that the particle spacing does not significantly influence the ability of DNA origami to bind between a AuNP pair, which implies that the RA distribution is reasonable for case (2).

Comparison of experimental data with the RA distribution for case (1) shows that experiments have more AuNPs with both 1 and 2 DNA origami attachments than expected in the RA distribution and less AuNPs with 0, 3, 4, 5, and 6 DNA origami attachments. The presence of more single attachments in my experiments shows that steric hindrance may be limiting multiple binding. However, the fact that there are also more double attachments to one AuNP indicates that steric hindrance in this geometry does not significantly influence attachment until there are 2 or more DNA origami already bound.

For case (2) experimental results show more nearest neighbor pairs with a single DNA origami attached and less with 0, 2, and 3 attachments when compared with the RA distribution. The large difference (nearly 9 standard deviations) between the random distribution and the experiment in the case of double attachment between AuNP pairs shows that steric hindrance influences the ability of a DNA origami to attach between an occupied AuNP pair. This is likely because a DNA origami attempting to bridge between an occupied AuNP pair interacts with the entire attached object, rather than just the ends, where the sticky ends are located. Thus it appears that increasing the DNA to DNA interaction area decreases the probability of multiple attachments. Therefore, increasing the influence of steric hindrance further at individual AuNP binding sites may be possible by decreasing the AuNP size, increasing the DNA origami size, or

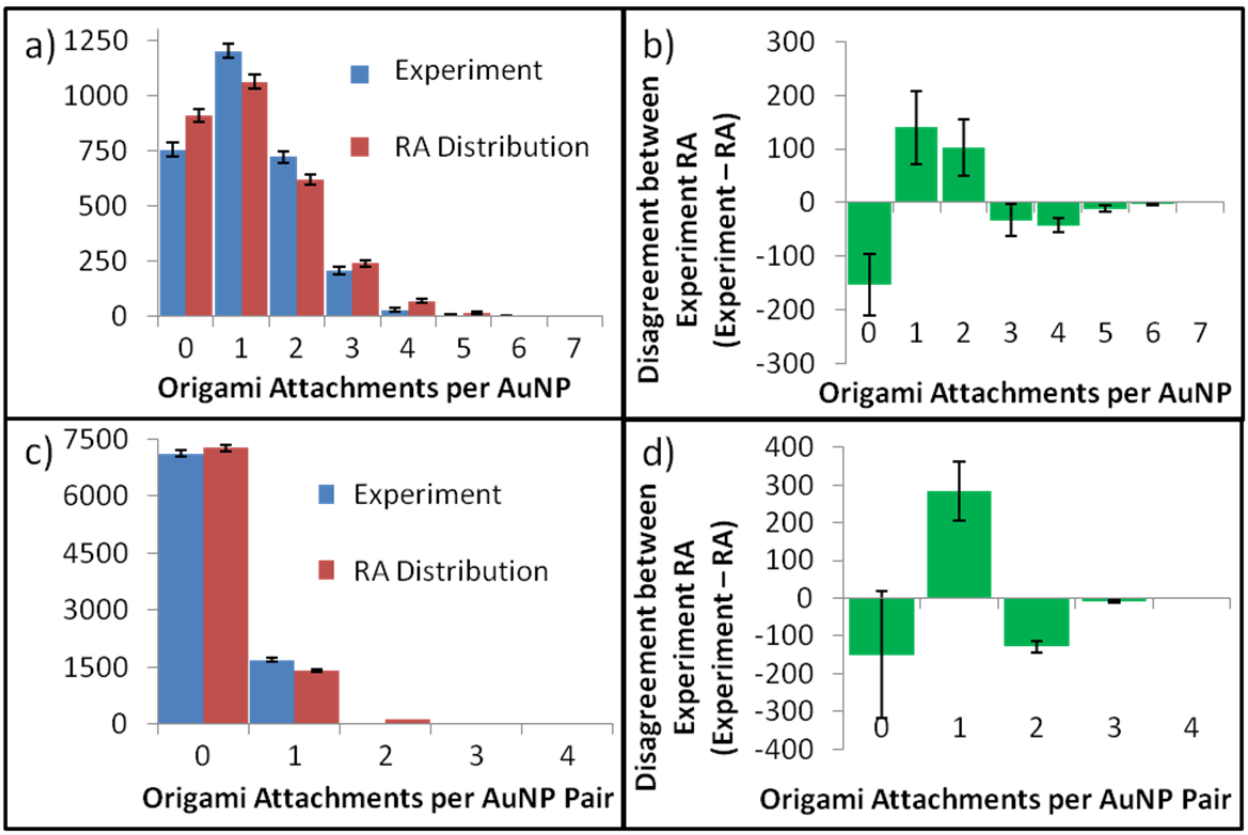

Figure 2.5. Here the influence of steric hindrance on multiple binding is analyzed by comparing binding statistics obtained from AFM data to a standard "balls in boxes" statistical distribution used to calculate the expected number of attachments per binding site if DNA origami binding is completely random. Results of the RA distribution were compared with statistics obtained from AFM data to determine the influence of steric hindrance in multiple attachment of DNA origami to one binding site, where a binding site is considered to be either one AuNP or a pair of nearest-neighbor AuNPs. a) Shows a histogram of the number of attachments per AuNP for the random attachment distribution and experiment. b) Shows the random distribution subtracted from the experimental results in a). c) Shows a histogram of the number of attachments between nearest-neighbor pairs for both the random attachment distribution and experiment. d) Shows the random distribution subtracted from the experimental results in c).

moving the sticky ends further away from the ends of the structure, so the AuNP is completely covered once one DNA origami is attached.

In conclusion, I have demonstrated the ability to align DNA origami to ~ 5 nm binding sites through DNA base pairing onto a patterned AuNP surface, fabricated by BCP micelle lithography. This is the first time BCP patterning has been used to fabricate DNA origami

attachment sites. Individual binding sites fabricated with this method are at least an order of magnitude smaller than binding sites used previously. Binding sites on this size scale are important to meet the alignment tolerance requirements for nanoscale DNA origami surface patterning. I have seen that the base pairing of DNA origami rectangles with patterned ssDNA-SH surfaces results in a stable, highly selective attachment to the surface. The chemically specific nature of the base-paired attachment may be useful to further control the location or orientation of attached DNA origami. Any patterning method allowing discrete regions in an AuNP array to each be modified with a unique ssDNA-SH sequence, would then allow location controlled attachment of multiple DNA origami shapes. Further orientational control may also be possible if individual DNA origami have two or more sticky end regions with different base sequences.

Chapter 3

Dual Patterning of a Polyacrylic Acid Layer by Electron Beam and Block Copolymer Lithography

3.1 Introduction

State-of-the-art optical surface patterning methods can produce feature sizes down to 22 nm; however, it is expected that non-optical techniques will be necessary in order to decrease feature sizes beyond this point.[9] Molecular self-assembly has been shown to create structures with feature sizes far below current optical limitations.[23, 34, 55, 59] Recently, the ability to create controlled self-assembled patterns on a surface has been enhanced by using top-down methods to direct the location and orientation of the self-assembling systems such as block copolymers (BCP).[21, 31, 51]

Several methods have been shown to direct BCP assembly by alignment with chemical or topographic features fabricated using top-down lithography techniques. For example, Yang et al. showed alignment of cylindrical forming BCPs to periodic SiO_2 pillars fabricated using electron beam lithography.[43] This technique allows a reduction of defects in the self-assembled patterns and control over the direction of parallel oriented cylindrical BCPs. Additionally, chemical patterns or physical trenches can be used to direct BCP assembly.[32-33, 49, 60]

Similarly, top-down techniques have also been used to control the location of arrays of BCP micelles.[51, 61-62] Micelle patterning is a promising technique that enables well ordered nanoscale patterns without the necessity of an annealing process. Often, the micelle patterns are used as

templates for a functional material such as metallic nanoparticles. These patterned nanoparticles can be used as catalysts for nanowire or nanotube growth,[63] etch masks to transfer the pattern to other materials, masks for pattern reversal to create porous surfaces,[61] or chemical attachment points for biological molecules or DNA nanostructures, which I discussed in chapter two.[64] In such applications it is generally desirable to have precise control over the location of particle arrays or even individual particles on a surface.

The techniques that control the location of micelle patterns with the highest accuracy use optical or electron beam lithography processes to remove micelles or nanoparticles from undesired areas. In one method an electron or focused ion beam is scanned over a micelle film, pinning the exposed micelles to the surface.[51, 65] A subsequent rinse with an appropriate solvent removes micelles which have not been exposed to the beam. The remaining micelles are then introduced to oxygen or hydrogen plasma, which removes the polymer and leaves an array of nanoparticles in areas which were exposed by the electron beam. In another method, an array of nanoparticles is formed from a micelle template. The surface is then coated with electron beam resist and patterned with electron beam lithography.[66] The nanoparticles which have been uncovered from the patterning process are then removed from the surface in an etchant. The resist is then stripped to uncover the remaining nanoparticles. Both of these methods are capable of patterning nanoparticles generated by BCP micelles with below 100 nm accuracy.

Both of the above mentioned techniques are used to pattern micelles or nanoparticle arrays after the micelle array is deposited. Thus, their accuracy is limited by the positions of micelles, which is unknown during the subsequent patterning processes and cannot be changed after micelle deposition. In order to remove this limitation and allow higher accuracy in patterning, a technique is needed which will direct the placement of micelles in desired locations as they are

deposited. Previous reports have shown the ability to place micelles within pre-patterned surface features on the 500 nm to micron scale.[67-68] To achieve higher control, here I demonstrate a method where self-alignment of micelles to electron beam patterned surfaces and pattern transfer allows accurate positioning of nanoparticle arrays.

To control the location of the BCP generated nanoparticles BCP micelles are used to template a PAA surface similarly to previous reports,[69] except prior to BCP micelle deposition I have patterned the PAA layer using electron beam lithography. Following deposition of a monolayer of micelles over the entire surface, a subsequent oxygen plasma treatment removes the substrate, and the micelle pattern is transferred to the PAA features. The resulting location controlled micelle templated PAA patterns are then loaded with metal salt and etched in a plasma to form 4.5 nm nanoparticles (see Figure 3.1).

These results indicate that as the BCP micelles are deposited onto the surface, they align and orient to the PAA features. I have found that by optimizing sizes of the PAA features this technique can be used to create straight lines of accurately positioned particles 4.5 nm in height in single and double file lines as well as particle pairs with controlled location and orientation.

3.2 Experimental Methods

The fabrication process is outlined in Figure 3.1. A solution of 250 kg/mol initially 25 % (w/w) PAA in H_2O was neutralized with NH_4OH and diluted with deionized H_2O until the solution contained 1% PAA by weight. The solution was then spin cast to a thickness of 20 nm onto a silicon surface with a 200 nm thick layer of thermally grown SiO_2. Next a 700 nm thick film of 7% w/w polymethyl methacrylate (PMMA; 950kg/mol) in dichlorobenzene was spun cast

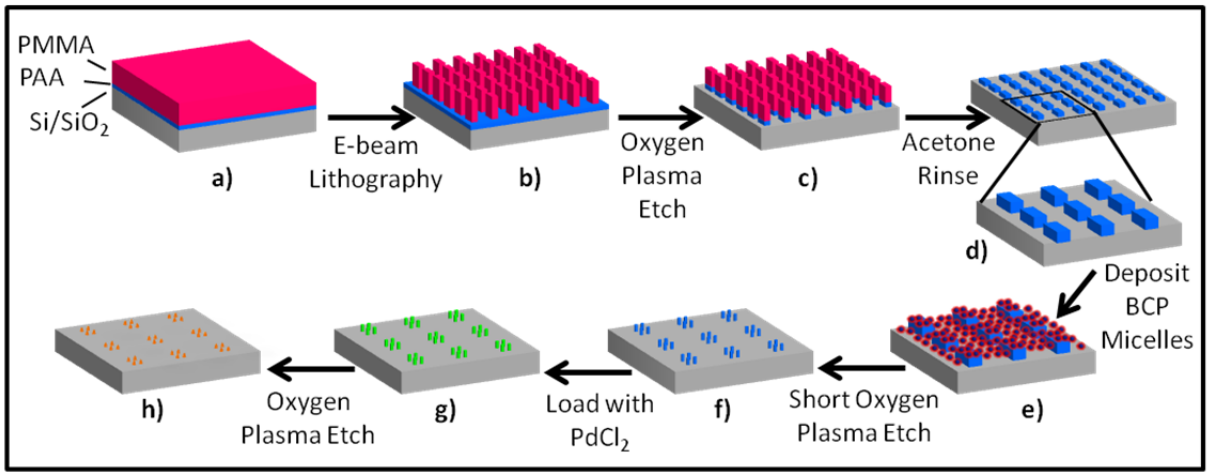

Figure 3.1. Schematic of the micelle templated nanofabrication process. a) A 20 nm thick film of PAA followed by PMMA electron beam resist are coated on a Si/SiO_2 substrate. b) Electron beam lithography is used to pattern the PMMA film. c) The PMMA pattern is transferred into the underlying PAA film. d) The PMMA is then removed by rinsing in acetone. The zoom in shows a closer view of the patterned PAA. e) Next, a monolayer of BCP micelles is deposited on the surface and assemble into a closed-packed array. f) The sample is then etched briefly in oxygen plasma, causing the pattern from the BCP micelles to be transferred into the remaining PAA. g) The resulting nanopatterned PAA features are then loaded with $PdCl_2$ in an IPA solution. h) The sample is then etched in an oxygen plasma for 20 min to remove the remaining PAA and form Pd nanoparticles.

onto the surface. The surface was then baked at 105 ^{o}C for 10 min on a hot plate. Electron beam lithography was used to expose the PMMA layer (Figure 3.1a-b) in the desired pattern. The exposed PMMA was developed away by dipping the sample in a solution of refrigerated 3:1 isopropyl alcohol: methyl isobutyl ketone for 1 min. The sample was then rinsed in a stream of isopropyl alcohol (IPA) and blown dry with air. The resulting lithographic patterns were transferred from the PMMA into the PAA with an oxygen plasma etch performed for 1.5 min at a power of 50 W and pressure of 300 mTorr. (Figure 3.1c). The PMMA film was then removed by rinsing for ~10 s in acetone held at 60^{o}C (Figure 3.1d), and the sample was rinsed in IPA and dried in a stream of nitrogen. The pattern geometries chosen were PAA zigzags, ovals, and stripes. The zigzags had a line-width of 270 nm, while the width of the ovals and stripes was

varied between 130 nm to 60 nm. Lengths of the features were 50 μm for lines and zigzags and varied from 500 nm to 125 nm for ovals.

Micelles were formed by dissolving polystyrene-b-poly-2-vinylpyrridine (PS-P2VP; PS: 57 kg/mol, P2VP: 57 kg/mol) in toluene to a concentration of 0.5% w/w and stirred for at least 6 hours. Micelles were then spin cast at 5000 rpm onto the patterned PAA surface to produce a monolayer of micelles over the entire surface (Figure 3.1e). A brief (20 s) oxygen plasma etch (40 W, 50 mTorr) was then used to transfer the micelle pattern into the electron beam patterned PAA (see Figure 3.1f). The etch time was chosen to be long enough to remove the micelles and etch completely through the PAA in areas not covered by the micelle. Palladium nanoparticles were formed by placing samples in a solution of 10 mM $PdCl_2$ in IPA for 15 min (Figure 3.1g). The samples were then removed and rinsed in a stream IPA for 30 s. The PAA was removed in a 20 min oxygen plasma etch (40 W, 50 mTorr; see Figure 3.1h).

3.3 Results and Discussion

Figure 3.2 shows an image of micelles deposited on a PAA zigzag structure. Micelles generally appear to be spherical however, there are some that appear to be elongated. This effect may be corrected by using higher purity solvent during micelle formation. Some disorder is introduced from the elongated micelles; however, generally micelles tend to align well with the edges of the PAA zigzags. This indicates that during deposition, the assembly of micelles is directed by the patterned surface.

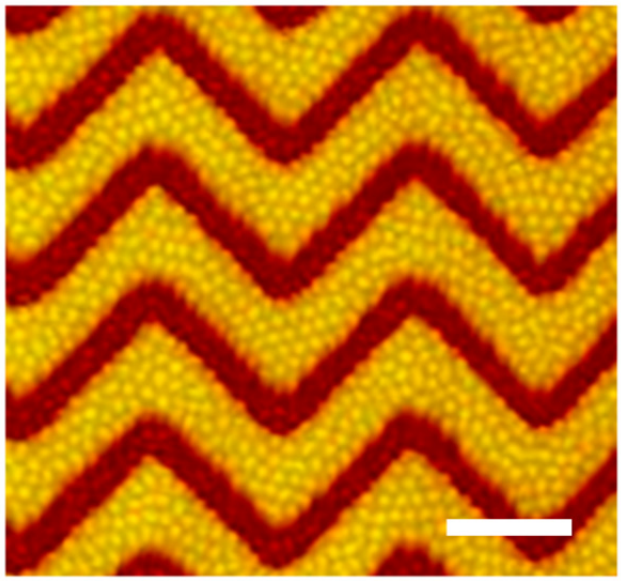

Figure 3.2. Tapping mode AFM image of BCP micelles deposited on PAA zigzag structures. Images suggest that deposited micelles tend to align with these structures. The scale bar is 500 nm.

Figures 3.3a shows an example of PAA oval structures (dimensions of 130 nm X 220 nm) after micelle deposition. The resulting Pd nanoparticles formed from structures of the same dimensions as in Figure 3.3a are shown in Figure 3.3b. Figures 3.3c,d show examples of PAA stripes (115 nm in width) after micelle deposition and after Pd nanoparticles are formed, respectively. AFM images in Figure 3.3a and c show that micelles form a packed monolayer across the surface, where ordering on top of PAA films appears to be as good as on the SiO_2 substrate. As expected from Figure 3.2, micelles on top of the PAA are generally well aligned to the PAA features. This effect is most prominent in Figure 3.3c, where generally micelles have lined in double file along the edges of the PAA. However, occasionally there is a switch from two micelles to a single micelle along the width, which indicates some variability in micelle positioning during the deposition process.

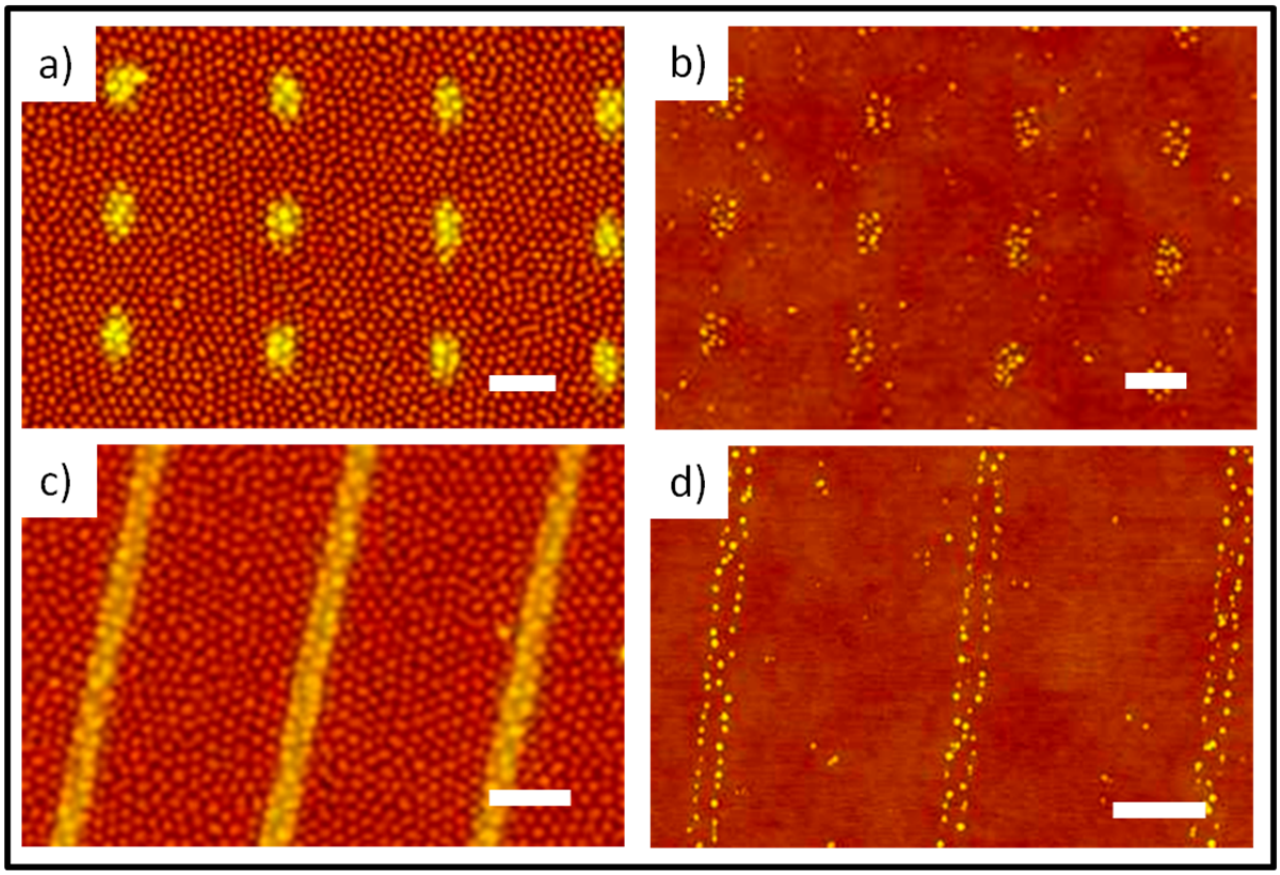

Figure 3.3. Tapping mode AFM images of BCP micelles after deposition on the electron beam patterned surfaces and the resulting nanoparticles formed. a) Shows BCP micelles deposited on patterned PAA ovals which had dimensions of 130 nm X 220 nm. b) Shows the Pd nanoparticles formed from PAA ovals shown in a) after transferring of the micelle pattern into the PAA, loading the resulting PAA with $PdCl_2$, and plasma etching. c) Shows micelles spin coated onto 115 nm wide PAA lines. Micelles on PAA lines of this width generally line up in double file. d) Shows double file lines of Pd particles following the fabrication process. All scale bars are 300 nm.

AFM analysis of the generated nanoparticles shown in Figure 3.3b and d shows a particle height of 4.5 nm ± 1.5 nm. The location of the nanoparticles is consistent with the expected location based on micelle alignment with PAA lines as shown in Figure 3.3a and c.

To study the effect of patterned PAA feature sizes on the alignment of micelles, PAA stripes were fabricated with widths ranging from 130 nm to 60 nm. An image of the nanoparticles generated after micelle patterning of these stripes is shown at the top of Figure 3.4. To analyze

the degree of alignment of these particles to the PAA stripes, the displacement (d) of each particle from an axis running parallel and through the center of each stripe was measured. The lengths of all lines of particles measured was at least 3 μm (entire length not shown). Resulting histograms of these measurements are shown in Figure 3.4a-f, where the line of particles corresponding to each histogram is labeled a-f, respectively. From these results from Figure 3.4a (130 nm wide line) there are two major peaks which are ~ 60 nm apart which is consistent with the micelle center-to-center spacing. This indicates that generally the line is two particles wide; however, the slight peak in the center is interpreted to mean that at some points it may be either 3 particles or 1 particle wide. Additionally, the non-zero values near the center are indicative of some disorder in the organization. In Figure 3.4b (line width ~115 nm), the two largest peaks are ~ 60 nm apart, where nearly 80 % of the particles are included in these peaks. The non-zero values near zero are a result of some switching along the line between two particles and one particle as discussed above. Figures 4c-f each show a single peak as expected from single file rows of particles. The width of the peak narrows as the line width is decreased from 100 nm to 60 nm. The standard deviation of particle displacement is 16.5, 12.5, 11, and 9 nm for Figures 3.4c,d,e, and f, respectively. For PAA lines with widths smaller than 60 nm there was inconsistent micelle adsorption to the PAA stripes, where following nanoparticle formation there were some locations with single file particles, while in other locations there were no particles generated.

The PAA stripes which generated the straightest lines of particles were 60 nm and 115 nm wide (Figure 3.4b and f). For the PAA stripes which generated single file lines of particles, this is expected since slightly larger widths than the micelle center-to-center spacing (~60 nm) would allow some freedom in micelle position across the width of the stripe, which caused variation in

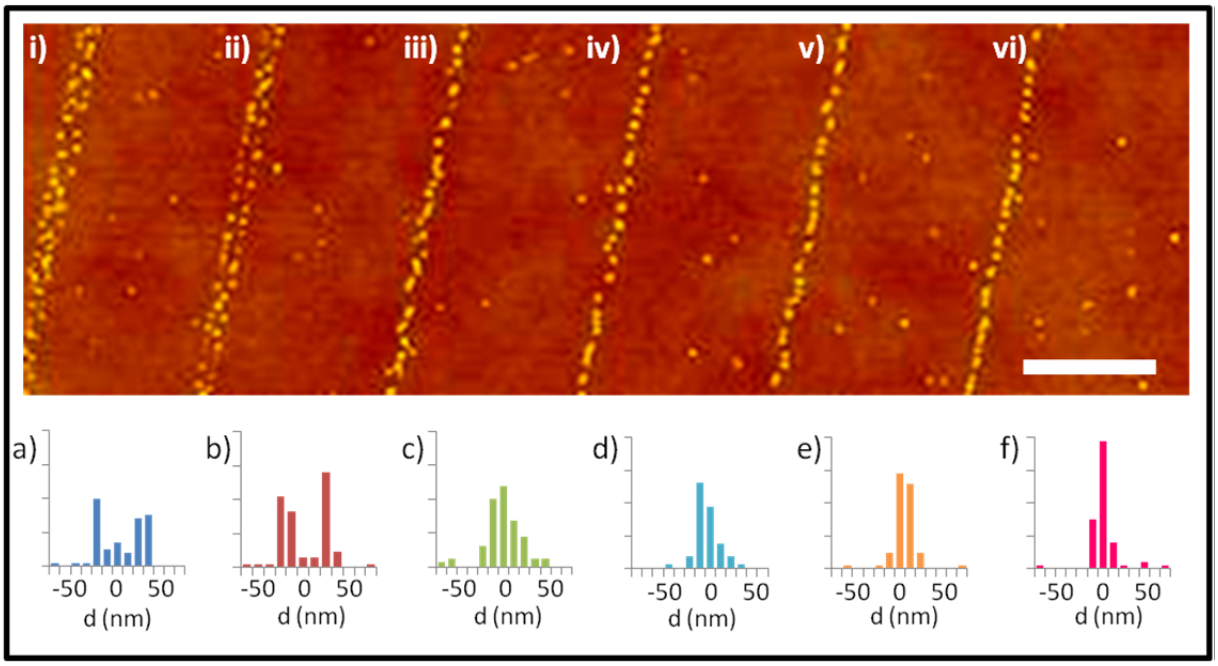

Figure 3.4. Pd nanoparticles formed by micelle templating of PAA lines with widths of 130 nm, 115 nm, 100 nm, 85 nm, 70 nm, and 60 nm for lines i), ii), iii), iv), v), and vi), respectively. Graphs a)-f) represent histograms of the displacement (d) of each nanoparticle along lines i)-vi), respectively. Here the value of the displacement is the measurement of the position of a given particle from the center of the line. In a) and b) there are two peaks, indicative of a double file line. In c)-f), a single peak is seen. In these histograms there is a general trend of peak narrowing for decreasing widths of PAA stripes. The scale bar is 500 nm.

position of the generated nanoparticles. For double file particle alignment, it is expected that hexagonally packed micelles will align best to a stripe which is $\left(\sqrt{3}/_2 + 1\right)L$ in width, where L is the expected center-to-center spacing between micelles. For L = 60 nm this corresponds with a width of 112 nm. For the slightly larger line width of ~115 nm, I see some hexagonal packing however, many of the particles appear to be arranged more similarly to a square array. This phenomenon, which can also be seen in Figure 3.3c-d, is interesting since square arrays are difficult to form using BCP self-assembly methods, since hexagonal packing is more energetically favorable. I expect that this is possible in this confined micelle system as a result of micelle alignment occurring preferentially to the edge of the PAA stripes, rather than to other

micelles. While the micelle-micelle interaction causes arrangement similar to a hexagonal array, preferential alignment with the edges would allow a square array to form if the width of the stripe is the correct width.

To achieve a higher degree of position control, PAA features capable of controlling micelle position in two dimensions must be optimized. To test two dimensional positioning, PAA ovals were fabricated with dimensions of 115 nm X 180 nm and 75 nm X 125 nm. Pd nanoparticles were then formed using the above procedure. Figure 3.5a and b show results from the 120 nm X 200 nm PAA ovals, and Figure 3.5c and d show results for the 75 nm X 125 nm ovals. The 120 nm X 200 nm PAA ovals often had two particles in width, however, due to narrowing of the ovals at each end often patterns were one particle in width on one or both ends. Generally there were 3 or 4 particles along the 200 nm length of these patterns, while the 75 nm X 125 nm PAA ovals generally generated 1 X 2 arrays of nanoparticles.

In Figure 3.5a, the ovals (120 nm X 200 nm) most often generated 5 nanoparticles (40% of the time), while they also frequently generated 4 or 6 nanoparticles (20% of the time, each). The 75 nm X 125 nm ovals (Figure 3.5 c-d), generated two particles 70% of the time, one 20% of the time, and 3 particles 10% of the time. The alignment of the particle pairs seen in Figure 3.5c was seen to vary by $\pm 15^{o}$, which based on the results shown in Figure 3.4, would likely decrease if the oval width were decreased to 60 nm.

The greater consistency in particle formation with the ovals in Figure 3.5c-d is expected, since there seems to be a much wider range of widths which can result in single file rows of particles than double file rows, as illustrated with the trend in Figure 3.4. Thus, a slight variation from the

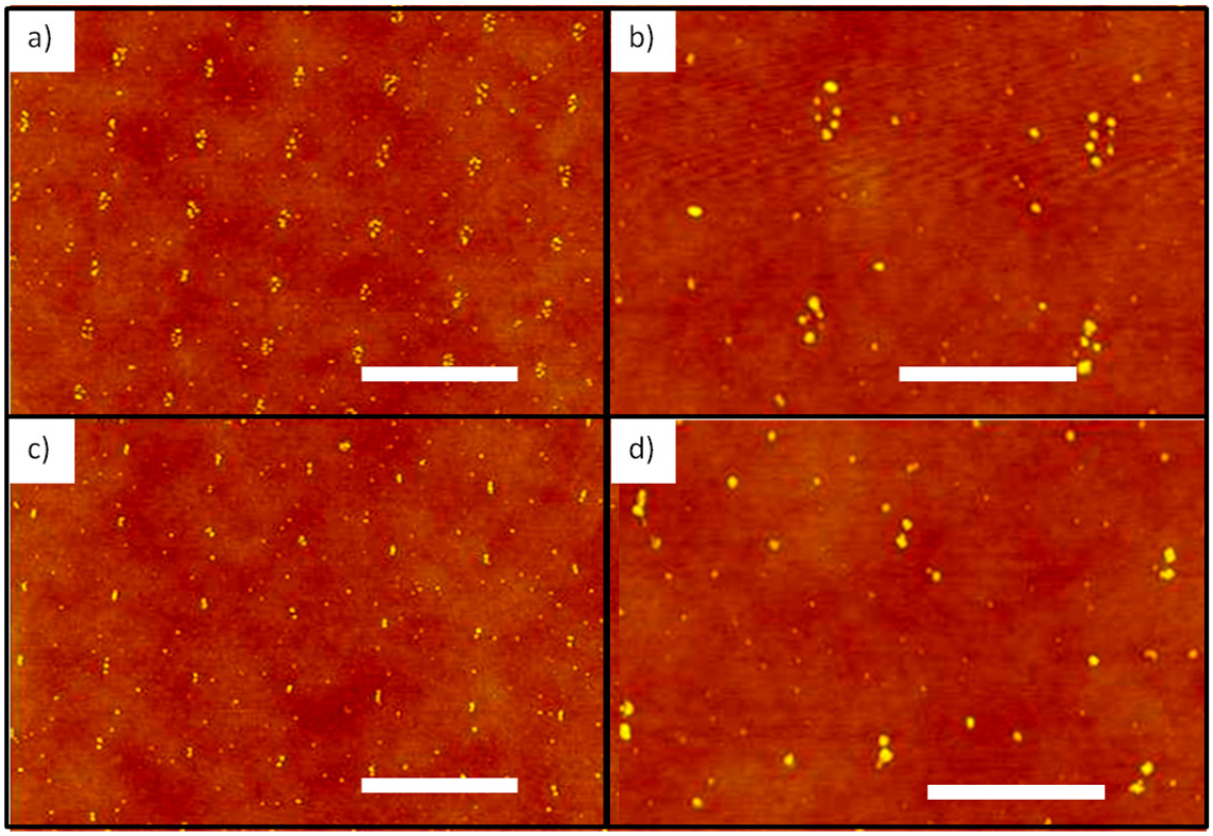

Figure 3.5. Tapping mode AFM image of nanoparticles obtained from micelle pattern transfer into PAA ovals of 120 nm X 200 nm in a) and b),and 75 nm X 125 nm in c) and d). b) And d) show close up images of patterns in a) and c), respectively. 70% of groups in c) and d) contain two particles. d) shows a zoom-in of the particles in c). Scale bars are 1 μm for a) and c) and 500 nm for b) and d).

optimal width may bring some disorder to the double-file particle lines. If double file lines or greater are desired, precise control of the PAA feature sizes must be achieved.

In conclusion, I have developed a method combining top-down electron beam lithography and bottom-up BCP micelle assembly methods to accurately pattern arrays of 5 nm Pd nanoparticles. It was determined that this method is useful to control the location of particle arrays that are down to one particle in width. Here the geometry was tuned to increase the accuracy of the particle position to within ± 9 nm. Additionally, I showed that with this method I could accurately place pairs particles in a two dimensional array.

This technique can be used to enable controlled attachment of DNA origami to a surface by utilizing the surface attachment techniques shown in chapter two. Specifically, generating particle pairs as shown in Figure 3.5 c-d will allow location and orientation control of DNA origami rectangles.

Chapter 4

Site-Specific Metallization and Electrical Characterization of Conductive Nanowires Templated on DNA Origami

4.1 Introduction

Self-assembly methods have shown promise for the fabrication of complex structures with extremely small feature sizes.[70-71] Scaffolded DNA origami, in particular, provides a robust and simple method for designing patterned shapes in the sub-100-nm regime. The DNA origami technique can produce a wide variety of two-dimensional,[36, 72] as well as three-dimensional,[5, 37, 73-75] structures by folding a long single-stranded DNA "scaffold" into a designed shape with use of a large number of shorter "staple" strands consisting of synthetic DNA. A distinct advantage of DNA origami is that the staple strands can be adjusted to engineer site-specific attachment points throughout the structure. Location-selective variability can be achieved either by direct chemical modification at the ends of staple strands or by extending staple strands with additional nucleotides and hybridizing these "sticky ends" with a complementary sequence containing the desired functional group or moiety. Using these techniques a variety of materials have been controllably attached to DNA origami such as RNA probes,[76] proteins,[77-80] carbon nanotubes,[81] and metallic nanoparticles.[54-55, 64, 82-84]

The use of DNA origami structures as templates for metallization is potentially enabling for technologies such as nanoelectronic circuits[2] and plasmonics,[85-86] among others. Although there is a considerable body of literature describing the metallization of linear, double-stranded DNA,[87-90] my group was the first to report the continuous metallization of DNA origami,[91] which was followed by a few more recent reports.[92-94] One particularly attractive aspect of molecularly

templated nanofabrication is the possibility of dictating the precise location of metallization. Site-specific metallization is possible with DNA origami where the recognition properties of DNA can be used to create the complex structures needed, for example, for nanocircuit formation. Also, for many applications it is imperative that the metallized structures are continuous and conductive. While much work has been done previously to characterize the conductivity of nanowires templated by linear DNA, this study is, to my knowledge, the first to verify continuity and conductivity of nanowires templated by DNA origami. This is due to difficulties in both fabrication and measurement. Fabrication of conductive nanowires on a DNA origami template is complicated due to the difficulty of achieving high seed density, plating precision, and high stability of the DNA origami during the plating process.[91] Site-specific placement of seeds causes limitations in seed density since the spacing between available attachment points is controlled by the staple strand spacing. Additionally, the seeds must be chemically modified prior to attachment and metallization, which may affect the metallization process. The focus of the present study is on the fabrication and characterization of conductive nanowires by site-specific metallization of origami templates.

Recently, site-specific metallization of a modular, 100 nm X 100 nm DNA origami tile was reported by Pais *et al*.[93] In that report metal structures of a few different shapes were formed by electroless plating of silver onto gold nanoparticles placed at specific sites on the DNA origami tiles. The work presented here provides at least three distinct advances toward enabling functional electronic device fabrication using site-specific metallization of DNA origami: 1) the metallization process used here was developed to create conductive nanowires needed for devices and includes experimental verification of conductivity; 2) the thin, branched DNA origami structures which my group has previously reported[38, 91-92], allow for considerably longer

wires than is possible with a modular and dense tile motif; and 3) the high seed density achieved herein permits the fabrication of continuous nanowires of very small diameter.

4.2 Materials and Methods

4.2.1 Materials

M13mp18 and streptavidin-coated magnetic beads for DNA scaffold preparation were purchased from New England Biolabs. Staple strands for DNA origami folding and PCR primers were ordered from Operon Biotechnologies (100 μM in TE buffer). Single-stranded DNA thiol was purchased from Operon Biotechnologies with PAGE purification and diluted to 1 mM in water. PCR purification kits were acquired from Qiagen. DNA polymerase and PCR buffers were purchased from Invitrogen or New England Biolabs. 30 kDa Amicon ultra-0.5 mL centrifugal filters were obtained from Millipore. 5 nm Au nanoparticles and mica for AFM imaging were purchased from Ted Pella. BSPP (bis(p-sulfonatophenyl)phenylphosphine dihydrate dipotassium salt) was obtained from Strem Chemicals. (100) n-type silicon wafers were purchased from Silicon Wafer Enterprises, LLC. The silicon monoxide film supported on copper TEM grids were purchased from Ted Pella (Product # 01830). The commercial Au plating solution was acquired from Nanoprobes (GoldEnhance EM, Catalog # : 2113). Gold(III) chloride trihydrate (≥ 99.9%) and hydroxylamine (98%) were purchased from Sigma-Aldrich. ZEP-520 electron beam resist and ZED-N50 developer were obtained from Zeon Chemicals. The 1165 MICROPOSIT^{TM} Remover was purchased from MicroChem.

4.2.2 DNA origami designs

Branched ("T") shaped DNA origami structures were formed using a 2,958 base scaffold, amplified from M13mp18 as previously reported.[38] To enable Au NP attachment, select staple strands from the previously reported design were modified to contain a sequence of 10 adenine nucleotides on the 3' end. In the initial experiments, 33 staples on one half of the top section of the "T" structure were modified. For conductivity measurements, the entire top section consisted of modified staple strands (67 in total). For the 'T" structure with a gap, 39 staples were modified. The prototype logic gate structure was folded using M13mp18 for the scaffold with 246 staple strands. 156 of the staple strands contain the extra 10 adenines on the 3' end for gold nanoparticle attachment.

4.2.3 DNA origami folding

Both types of DNA origami structures were folded by heating a mixture of the scaffold and staple strands (2 nM scaffold and 20 nM of each staple strand in 1X TAE-Mg^{2+} buffer) to 95^{o}C for 3 min and then slowly cooling to 4^{o}C over 90 min. DNA origami solutions were filtered with 30 kDa Amicon filters, to remove most of the excess staple strands, by centrifuging for 10 min at 13,000 rpm. Samples were rinsed twice with 450-500 μL of either 1X or 10X TAE-Mg^{2+} buffer (10 X was used for DNA origami surface seeded samples) by centrifuging for 10 min. at 13,000 rpm and recovered by spinning for 3 min at 3,500 rpm.

4.2.4 Au NP preparation

We followed steps similar to those reported previously[54, 95] to phosphinate and concentrate the Au NPs with BSPP. More specifically, 1.5 mg BSPP was added to 5 mL of Au NPs and shaken overnight. 100 mg of NaCl was added and the solution was centrifuged to pellet the Au NPs. The supernatant was removed and the Au was resuspended with an aqueous BSPP solution (100 μL, 2.5 mM). Methanol (100 μL) was added and the solution was centrifuged again to pellet the Au. After removing the supernatant again, the Au was resuspended in aqueous BSPP solution (100 μL, 2.5 mM). The concentration of Au NPs was estimated by comparing the absorption at 520 nm to the absorption of the original gold solution using a Nanodrop 1000 spectrophotometer.

4.2.5 Au NP-DNA conjugates

Thiolated DNA was used without deprotecting the disulfide bond as it was found that the reaction worked either with or without deprotection. Au NPs and thiolated DNA were combined in a 1:200 molar ratio and left to react at room temperature (RT) for at least 19 hrs. The Au NP DNA conjugates were filtered using 30 kDa Amicon filters to remove unbound thiolated DNA. Samples were rinsed twice during the filtration using 450-500 μL 0.5 X TBE buffer. About 30-35 μL were recovered, with Au NP concentrations around 1 - 3.5 μM.

4.2.6 Attachment of Au NPs to DNA origami structures

For solution attachment of Au NPs to DNA origami structures, DNA origami was combined with the Au NP-DNA conjugates with varying Au NP to DNA origami ratios (of about 1:1, 12:1, 19:1, and 27:1) and cooled from 37 ˚C to 20 ˚C over about 17 min. Then the solution was deposited onto a mica surface for AFM imaging.

For Au NP surface attachment to DNA origami on SiO_2, DNA origami structures were placed on silicon surfaces using a method reported by Kershner *et al*.[44] Silicon dioxide surfaces were plasma cleaned (Harrick Plasma Asher; PDC-32G) for 30 sec at 18 W to remove contaminants on the surface. Then, 3 μL of filtered DNA origami (2 nM or 0.67 nM), in 10X TAE/$MgAc_2$ buffer, was allowed to adsorb onto the cleaned surface for 2 hrs in a humid chamber at RT. The sample was then dipped in a 50% ethanol solution (5 sec) and a 90% ethanol solution (1 hr). Next, the surface was dried by a stream of filtered air and put back into a humid chamber. Subsequently, 12 μL of seeding solution (Au NP-DNA conjugates diluted in 10X TAE/$MgAc_2$ buffer, 33 nM) was added onto the surface and allowed to seed DNA for 30 min at RT. Afterward, the surface was rinsed in 10X TAE/$MgAc_2$ buffer (5 sec), 50% ethanol solution (5 sec), and 90% ethanol solution (1 hr). Finally, the surface was dried with a stream of filtered air.

4.2.7 Electroless Au plating

The commercial Au plating solution was prepared according to the manufacturer's instructions. This plating solution was then mixed with an equal volume of $MgCl_2$ solution to yield a final Mg^{2+} concentration of either 2 mM or 10 mM. The plating was conducted by putting

60 μL of plating solution onto a SiO_2 sample surface at RT. The plating was allowed to proceed for 1 min, 2 min, 5 min, 10 min, or 20 min. The plating was quenched by rinsing the surface with $MgAc_2$ solution (4 mM Mg^{2+}) for a few seconds, then with water for 2 s, and dried in a stream of filtered air.

Natan's Au plating solution consists of 0.01% (by weight) of $HAuCl_4$ and 0.001% (by weight) of NH_2OH. For this plating process, 60 μL of Natan's Au plating solution was put onto a sample surface (either seeded DNA origami or DNA origami that was plated for 1 min with commercial Au plating solution) and allowed to plate for 2 min. Afterward, the surface was rinsed with a $MgAc_2$ solution (4 mM Mg^{2+}) for a few seconds, then with water for 2 seconds, and dried with a stream of filtered air.

4.2.8 Conductivity measurements

Electrode sets were fabricated using standard electron beam lithography methods with ZEP-520 electron beam resist using a Philips XL30 S-FEG scanning electron microscope. Following electron exposure the resist was developed using ZED-N50 developer. Next, a CHA-600 thermal evaporator (CHA industries) was used to deposit a 5 nm chromium adhesion layer and 40 nm of gold on to the patterned resist. Lift-off of resist was done overnight in 1165 Microposit remover at RT. Elevated temperatures were avoided since many origami were removed from the surface when the lift-off temperatures were above 60^{o} C. Following lift-off, surfaces were rinsed in 2-propanol and dried in a stream of air.

Electrical measurements were performed by using micromanipulator probes to connect two measurement electrodes across a power source. LabVIEW was used both to control the applied

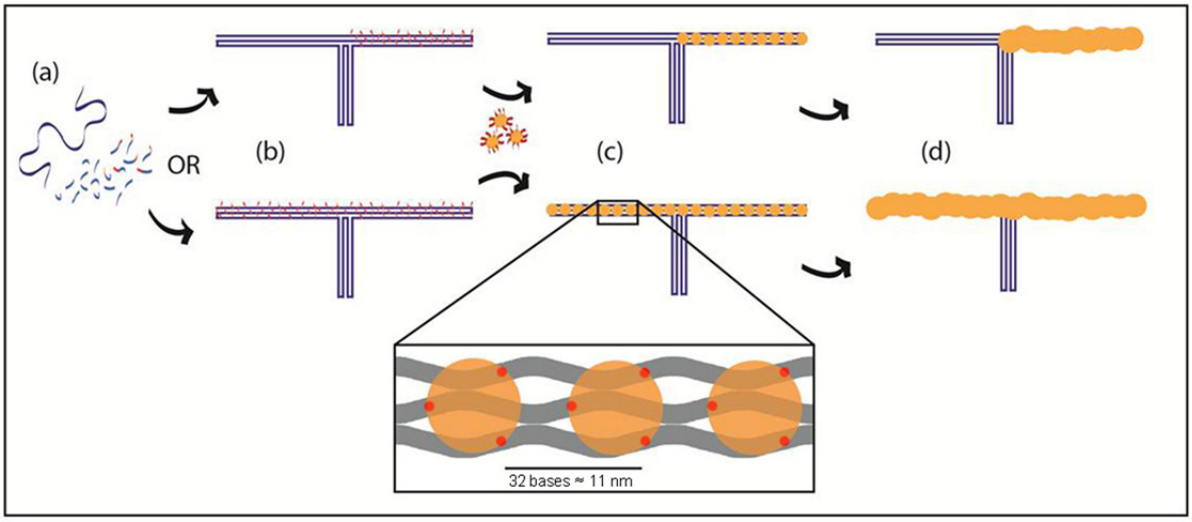

Figure 4.1. Process used for site-specific seeding by attachment of Au NPs and subsequent metallization. a) Regular (blue) and modified (red portion) staple strands are used to fold a branched "T" DNA origami structure. b) The location of modified staple strands is programmed based on desired regions for particle attachment. c) Au NPs coated with DNA complementary to the modified staples are added and attached to the DNA structure. A section is enlarged to show spacing of attached Au NPs along the DNA structure. d) A subsequent metallization procedure grows the particles until a continuous metal wire is formed across the locations seeded by Au NPs.

voltage and read the current measured from a picoammeter (Ithaco). The voltage was generally ramped from -100 to 100 mV across electrodes. However, to test the stability, up to 1.5 V was applied across some nanowires.

4.3 Results and Discussion

Figure 4.1 demonstrates the assembly process for site-specific metallization of DNA origami structures to form metallic nanowires. The DNA origami structure shown is a branched "T" structure, which was formed as previously reported[38] except where staple strands are extended by an A_{10} sequence on the 3' end in selected locations (Figure 4.1a-b). After folding the DNA

origami, excess staples were removed by filtering. Gold nanoparticles (Au NPs) nominally 5 nm in diameter were conjugated with thiolated T_8 DNA according to established protocol[54, 95] and combined with the DNA origami (Figure 4.1b-c). Attachment of the T_8 DNA-linked Au NPs to the extended A_{10} staple strands on the DNA origami creates "seeds" along specific sections of the DNA structure for further metal deposition (Figure 4.1c-d).

The attachment sites, or A_{10} extensions, on the DNA origami were positioned on every staple strand within the desired sections, making them about 11 nm apart along each double helix and in a staggered pattern with adjacent helices (see red dots in zoomed region of Figure 4.1c). Since multiple thiolated DNA strands are attached to each Au NP and each staple strand extension on the DNA origami contains the same DNA attachment sequence, a 5 nm Au NP could bind easily to the DNA origami through as many as three (and perhaps four) of the extended staple strands. In initial Au NP seeding experiments, "T" origami structures were designed to have Au NPs bind to only one half of the top section of the DNA origami (see upper structure in Figure 4.1b). This portion is ~120 nm long and contains 33 positions for approximately 11 Au NPs to attach.

When Au NPs were mixed in solution with the DNA origami at a ratio of about 12:1 Au NPs to DNA origami, the section with Au NPs attached almost always appeared significantly shorter by atomic force microscopy (AFM) than before Au NP seeding. To explore this phenomenon, ratios of Au NPs to DNA origami of about 1:1, 19:1, and 27:1 were also tested. The 1:1 ratio samples looked very similar to the seeded samples with a 12:1 ratio. In both samples, instead of a Au NP (or a few Au NPs) spread somewhere along the portion of the "T" which contained attachment points, the modified section generally looked truncated with the Au NPs near the junction of the "T" structure (see supporting information for AFM images). Increasing the ratio of Au NPs mixed with DNA origami to ~19:1 yielded some longer seeded segments and

increasing the ratio to ~27:1 gave even more seeded segments close to the unseeded length (see Figure 4.2a and supporting information). It is possible that when an insufficient number of Au NPs are available for attachment the DNA origami can wrap or fold around attached Au NPs, causing it to appear shorter. Occasionally, in samples with the highest Au NP to origami ratio, there are what appear to be origami aggregates. It is possible that in some of these instances Au NPs are binding and connecting two origami structures together. However, since origami were also seen lying very close together in some samples of unseeded origami, it is difficult to quantify this effect.

To increase the length of the seeded region, the DNA origami design was modified so the staple strands were extended across the entire top section of the "T" structure (see bottom structure in Figure 4.1b). This section is ~240 nm long and contains 67 total extended staple strands for approximately 22 Au NPs to attach. When Au NPs were attached in solution to this structure, the two sides of the top section usually folded together with some Au NPs attached to both sides (see Figure 4.2b). Since the entire top section contains the same attachment sequence and the "T" structure is somewhat flexible, this was a reasonable, but undesired, result. The problem of simultaneous attachment may be addressed in multiple ways, for instance, by using staple strands with different binding sequences on each arm. In this study, the matter was resolved by depositing DNA origami first on a thermally grown silicon dioxide surface, and then exposing the surface to the Au NP solution to permit gold particles to interact with the deposited DNA origami.

To achieve stable adsorption of the DNA origami on the oxide surface the process reported by Kershner *et al.* was used.[44] Specifically, a solution of DNA origami (0.67 nM) containing sticky ends modified as shown in the bottom design of Figure 4.1b, was left on the surface for 2

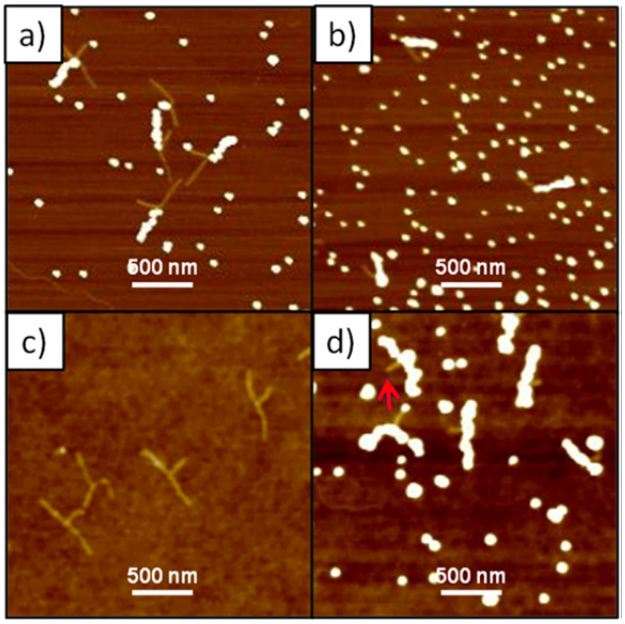

Figure 4.2. Tapping mode AFM images of "T" DNA origami structures. a) "T" DNA origami with modified staple strands along half of the top section after the Au NP attachment process was done in solution. Here a ratio of ~27:1 Au NPs to DNA origami was used. b) "T" DNA origami with modified staple strands along the entire top section after the Au NP attachment process. For a) and b) samples were deposited on mica surfaces for imaging. (c) Unseeded "T" DNA origami deposited on a SiO_2 surface. (d) "T" DNA origami seeded with Au NPs after surface deposition on SiO_2. The red arrow points to the unseeded portion on the origami. The height scale in all images is 6 nm.

hours to allow magnesium ions to bind the negatively charged DNA structures to a plasma cleaned, negatively charged silicon dioxide surface.

Figure 4.2c shows an AFM image of "T" DNA origami on a SiO_2 surface prior to seeding with Au NPs, and Figure 4.2d shows the DNA origami following Au NP attachment. It is clear that the particles have attached to the top portion of the "T" origami as intended, since the region not modified for Au NP attachment (marked with an arrow in Figure 4.2d) is clearly seen. Comparison of Figure 4.2c and 2d shows that the shape of the "T" origami is well conserved during the Au NP attachment processes, since the top portion has consistent curvature and length before and after attachment. The purpose of the attachment of Au NPs is to create sites on the

origami which can be further metallized to form a conductive segment or nanowire. In order to obtain nanowires with the smallest possible dimensions it is essential to have Au NPs which are spaced as closely as possible in the desired region on the origami. Since, AFM imaging cannot resolve spacing between particles because of tip effects (Figure 4.3a), scanning electron microscopy (SEM) and transmission electron microscopy (TEM) were used to examine particle location and spacing, and to provide quantitative measurements of the size of gaps between Au NPs.

SEM samples were prepared using surface seeding of "T" DNA origami on thermally grown SiO_2 surfaces as explained above, and TEM samples were prepared by surface deposition and seeding of the DNA origami on a 40 nm silicon monoxide film supported on a copper TEM grid. SEM data (Figure 4.3b-c) shows the average length of the seeded portion of the DNA origami to be 195 nm. On average there were 16 Au NPs attached to each DNA origami, and the median center-to-center spacing was 11.7 nm. A mean Au NP diameter of 7.6 nm, found by measuring particle sizes from high resolution TEM images, was used to estimate the corresponding gap size between particles, (see inset of Figure 4.3c). Thus, I estimate the median gap between Au NPs to be 4.1 nm. However, often in one or more locations there were larger gaps between Au NPs (see Figure 4.3d).

Interestingly, this microscopy analysis has shown that the Au NPs generally line up in single file along the DNA origami with a median center-to-center spacing (11.7 nm) that nearly matches the sticky end spacing on each of the three double helices on the top portion of the "T" origami (10.5-11 nm). This likely means that the Au NPs are attaching to sets of 3 sticky ends as indicated in the zoomed region of Figure 4.1c. When all Au NPs attached to the DNA origami are considered, the ratio of total extended staple strands to Au NPs is 4.19. However, when only

the regions with no large gaps between Au NPs are considered the ratio becomes 2.75. It can be concluded that the Au NPs are generally attached to three sticky ends, although some attachment of Au NPs to only two sticky ends also must occur.

These results show closer Au NP spacing than previously reported techniques. This may be due to the use of a short T_8 strand to link the Au NPs to the DNA origami. Because of the short persistence length of single-stranded DNA, the length of the T_8 strand is ~2 nm in solution.[96] Thus, the effective diameter of the particle is ~ 11.6 nm, similar to the median center-to-center spacing. Additionally, the high density of available binding locations that have been used increases the probability that a Au NP will attach when it interacts with the DNA origami, making it more likely that particles will attach with the minimum possible spacing.

Following seeding, the goal of my group was to selectively plate the Au NP seeds with gold until continuous wires formed. The minimum possible wire width following the plating step is limited by the largest gap between Au NPs. To fill a gap with a plating process, the width of the Au NP seeds must increase by at least the gap size, or equivalently, the radius of each seed must increase by at least half of the gap size. From Figure 4.3d it was found that the maximum gap sizes on each DNA origami ranged from 12 to 37 nm (median value was 19 nm). Assuming hemispherical growth of the seeds, it is expected that most wires 26.6 nm (7.6 nm Au NP width + 19 nm gap size) or larger in width would be continuous across the length of the seeded portion of the branched origami. However, continuous wires of 11.7 nm in width could be achieved if all gaps between Au NPs equaled the median gap size (7.6 nm Au NP width + 4.1 nm median gap size). Optimization of seeding parameters such as Au NP size, Au NP:origami ratio, seeding temperature and time will be necessary in order to achieve this result.

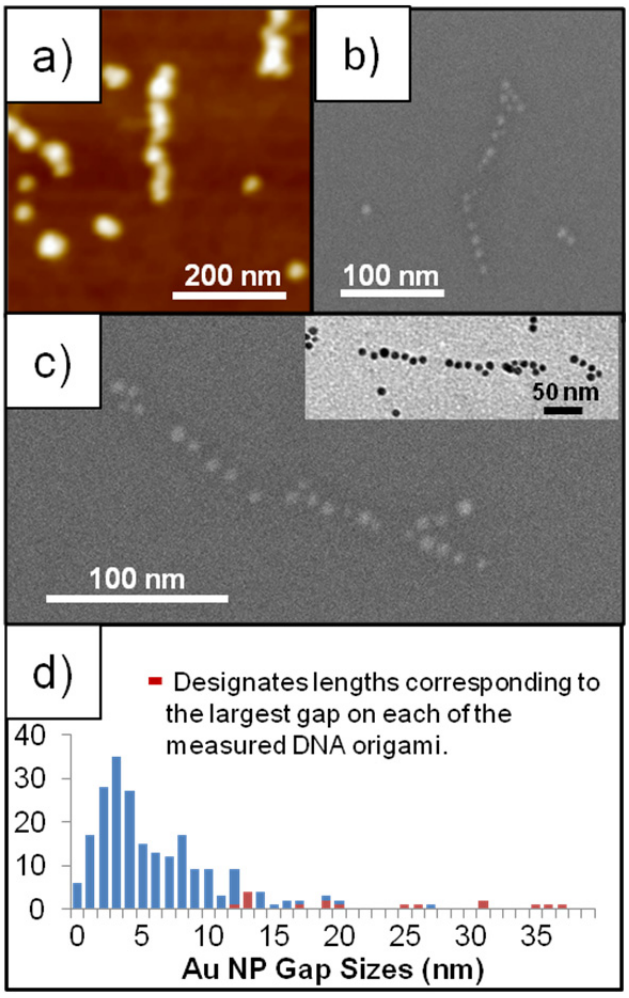

Figure 4.3. a) Tapping mode AFM image of Au NP seeded DNA origami (zoomed and adjusted height scale from Figure 4.2d; height scale 20 nm). b)-c) Examples of high resolution SEM images used to determine the center-to-center spacing of Au NPs seeded on DNA origami. The inset in c) shows a bright field TEM image of a Au NP seeded DNA origami. d) Histogram of the gap sizes between particles on the seeded DNA origami. The red bars correspond to the largest gap size in each of the measured DNA origami.

To selectively plate the Au NP seeds a modified commercial Au plating solution was used to which 10mM $MgCl_2$ was added (see methods above). Figures 4a-h show SEM results for samples plated for 1, 2, 5, and 20 minutes, respectively. Figure 4.4i shows the width of DNA nanowires plated for 5, 10, and 20 minutes, since these times were long enough for many nanowires to appear continuous by SEM.

After 1 min of plating, the average width of the Au NPs on the DNA origami increased by 5.4 nm from the initial seeded width (7.6 nm). SEM imaging (Figure 4.4a-b) showed that the nanowires formed were not continuous at this stage. This is not surprising since the amount of growth was not sufficient to fill in the larger gaps ($\geq$ 12 nm) that occurred periodically between the seeds. After 2 min of plating, metallization appeared continuous for some of the origami since the increase in the plated width was sufficient to span the "large" gaps that were on the order of 12 or13 nm (Figure 4.4c-d, see also histogram in Figure 4.3d). The general trend towards increased connectivity continued with the longer plating times (Figure 4.4); in addition, the plating rate decreased with plating time (5.4 nm/min after 1 min and 0.87 nm/min after 20 min) and the uniformity of the nanowires appeared to get worse as the plating time increased.

The substantial decrease in the plating rate with time indicates the potential importance of reactant transport. In fact, the observed rate of metal accumulation was close to that calculated by assuming that the plating process was diffusion limited. To further explore the role of mass transfer in the plating process, plating was done on a control surface with no DNA origami and sparse Au seeds, which were prepared and coated with DNA-thiol as discussed above. The sparse seed spacing (less than 15 Au seeds in an area of 10 μm by 10 μm) permitted a much higher rate of transport to the seeds. When plated for 2 min the seeds grew to an average height of 49 nm, much taller than that on the surfaces with a high density of seeded DNA origami, and consistent with expectations.

The depletion of reactants during plating of the DNA origami implies that a higher plating rate might be achieved if multiple plating steps, each using a fresh plating solution, were done for each sample. When a surface containing seeded DNA origami was plated twice with fresh

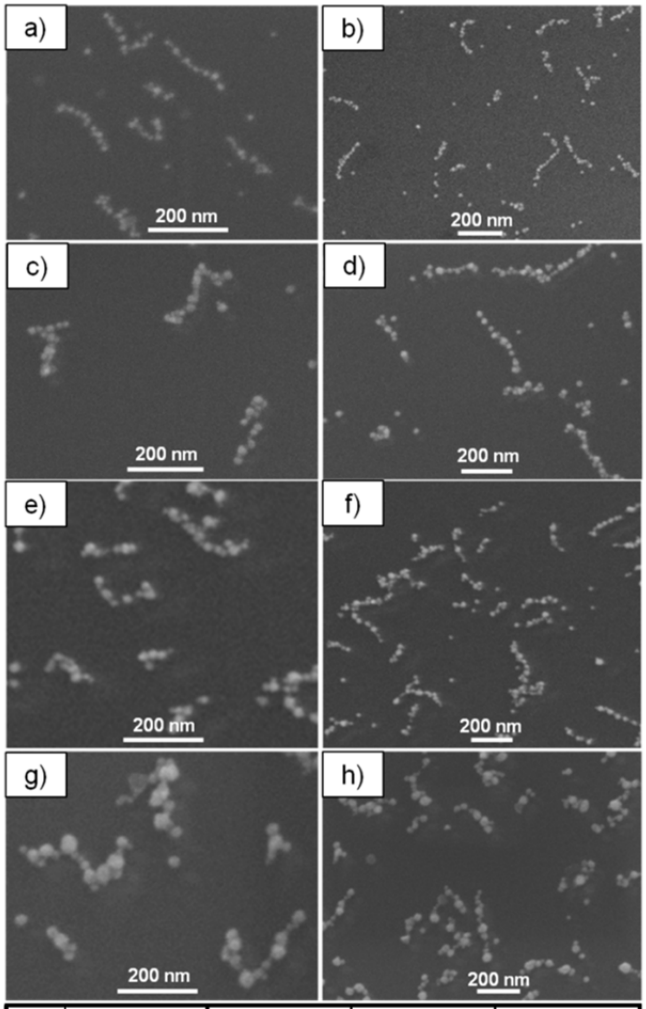

i)

Time (min)	5	10	20
Nanowire Width (nm)	18.3 ± 6.1	19.8 ± 7.2	25.0 ± 11.4

Figure 4.4. SEM images following Au plating of the Au NP seeds on the "T" DNA origami with a modified commercial plating solution. a-b) DNA origami plated for 1 min. c-d) DNA origami plated for 2 min. e-f) DNA origami plated for 5 min. g-h) DNA origami plated for 20 min. i) A table of the average widths (measured from SEM data) of the plated DNA origami for the plating times indicated.

plating solution, each time for 3 min, the average width of the plated DNA origami was 35.0 $\pm$14 nm, significantly larger than samples plated for 20 minutes with one solution (Figure 4.5a-b). However, the width across individual wires varied substantially from 10 nm to 65 nm causing the morphology of the nanowires to look similar to beads on a string, since some sections plated at a

much higher rate than others. This is similar to the morphology seen in the sample plated once for 20 min shown in Figure 4.4d. While the plating rate was significantly increased by plating in two steps, the nanowires were still non-uniform reflecting the possible limiting role of mass transport.

Because of limitations with the Au plating solution demonstrated above, that solution is unlikely to result in uniform deposition under the conditions of interest to this work. In contrast, Satti *et al*. [97] observed more uniform plating of gold on λ-DNA with a solution consisting of $HAuCl_4$ and NH_2OH that had been used earlier by Natan *et al*. [98] to enlarge Au NPs. This plating solution did not appear to work in initial experiments, which showed no observable increase in the size of Au NPs exposed to the solution. Apparently, the functionalization of the Au NPs with oligonucleotides or perhaps residual citrate or BSPP inhibited plating. However, substantial plating was observed when DNA origami were plated for 1 min with the modified commercial solution and then plated for 2 min with the new solution (Natan's solution). The width of the metallized origami ranged from 19.4 nm to 38.9 nm with an average value of 33.0 nm and a standard deviation of 7.3 nm. This standard deviation is about half that observed for DNA origami plated to a similar width in multiple steps with the previous plating solution. Thus, the use of Natan's Au plating solution increased the uniformity of plating and yielded continuous structures as shown in Figure 4.5c-d.

Electrical measurements were performed to determine the continuity of the DNA origami templated nanowires following metallization using Natan's plating solution. Sets of gold measurement electrodes were fabricated using electron beam lithography on SiO_2 surfaces which contained randomly oriented metallized DNA origami. The Au electrodes were formed by thermal evaporation of a 5 nm chromium adhesion layer followed by 40 nm of Au onto the

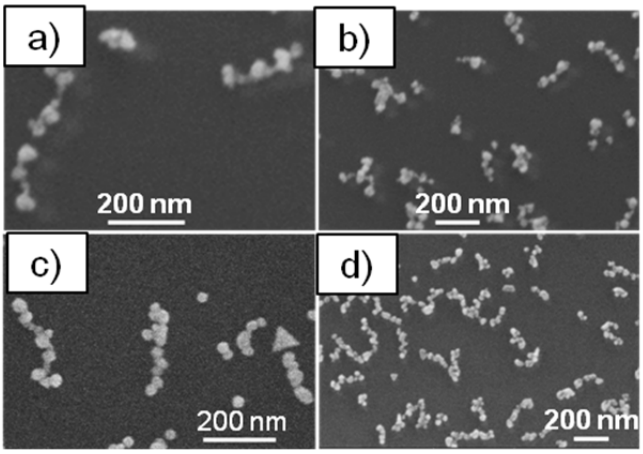

Figure 4.5. SEM images of plated "T" DNA origami. a-b) DNA origami plated twice for 3 min each using the modified commercial plating solution (with Mg^{2+} added). c-d) Origami plated with the modified commercial Au plating solution for 1 min and Natan's Au plating solution for 2 min.

lithographically patterned surface. The resist was removed by immersion in 1165 MICROPOSIT™ Remover at room temperature overnight. Each electrode set consisted of eight 50 μm X 50 μm Au pad (Figure 4.6a) connected to 100 nm wide measurement electrodes in parallel (see Figure 4.6b), with a gap between measurement electrodes of 160 nm. This geometry allowed measurement electrodes, which had been fabricated on top of the metallized origami, to make connection across correctly oriented DNA origami. To measure the resistance between two electrodes, micromanipulator probes were placed on the corresponding 50 μm pads. The voltage between the electrodes was generally ramped from -100 mV to 100 mV, and up to 1.5 V was applied across some electrodes. The resulting electric current was measured with a picoammeter (Ithaco). As a control, electrode sets were fabricated on a SiO_2 substrate containing no metallized DNA origami, and voltages were applied across electrodes as in samples which contained metallized DNA origami.

To ensure that contact resistance between the micromanipulator probes and 50 μm Au pads did not substantially affect the measured resistances, two adjacent electrodes in a set of measurement

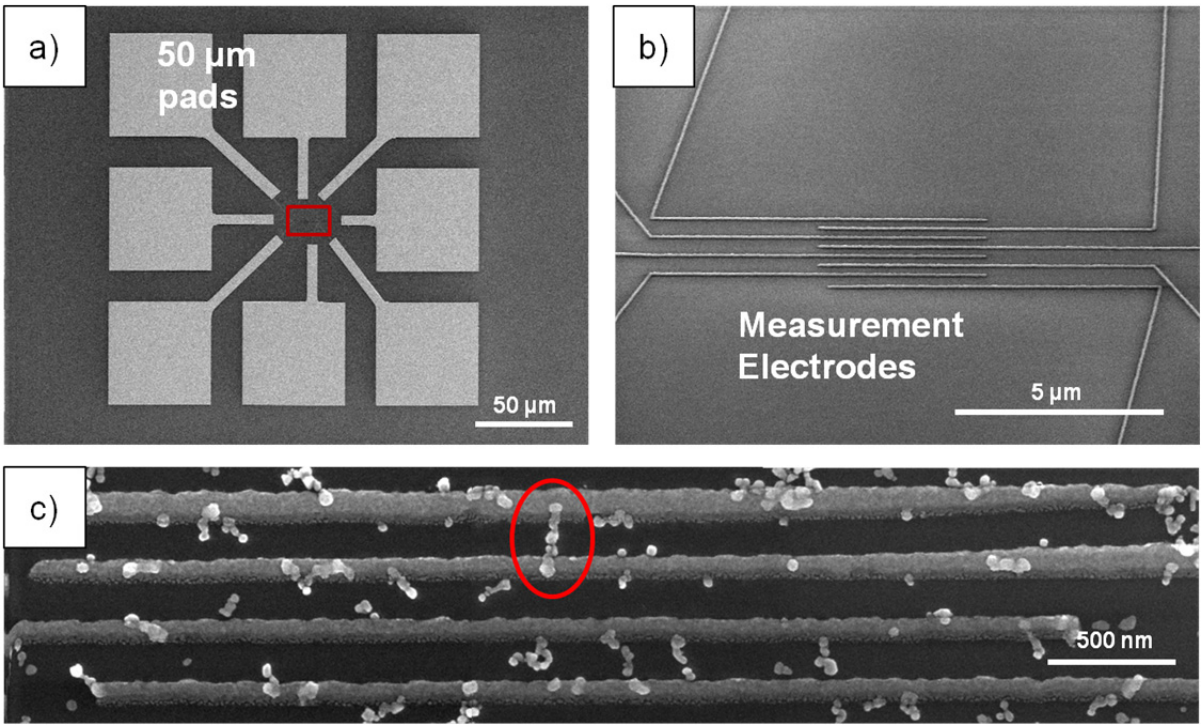

Figure 4.6. Electrode set geometry for electrical measurements of metallized DNA origami. (a) 50 µm pads allowing electrical connection by micromanipulator probes. (b) Zoom in of the region enclosed in the box in (a) showing 100 nm electrodes running parallel. Parallel Au electrodes are 4 µm long with a gap of about 160 nm between electrodes. Image is on a sample containing no DNA origami. (c) Close up of electrode set on a surface containing metallized DNA origami. Between the top two electrodes, marked with a red circle, is a single metallized DNA origami bridging the gap. Electrical measurements showed this origami to have a 2 kΩ resistance.

electrodes were intentionally connected during the lithography step. Following the evaporation of chromium and gold and resist lift-off, the resistance across the connected measurement electrodes was 4 Ω, which I have assumed is the maximum possible value of the contact resistance.

As voltages were applied across electrodes fabricated on a surface of metallized DNA origami, the number of electrically connected electrode pairs in a given electrode set was dependent on the local DNA origami surface concentration. In regions of high DNA origami surface concentration, electrode sets contained multiple locations where adjacent electrodes were

connected by one or more metallized DNA origami. Electrode sets in DNA sparse regions often contained either zero or only one conductive origami bridging between electrodes, and electrical measurement of a control sample where electrode sets were fabricated on a SiO_2 surface containing no conductive origami, did not show any adjacent electrodes which were electrically connected. Since the density of metallized DNA origami tended to decrease slightly during lithographic processing a 2 nM solution of "T" DNA origami was used during initial deposition onto SiO_2 surfaces to achieve a surface density of metallized DNA origami sufficient for successful electrical measurements.

An example of a metallized DNA origami nanowire connecting between adjacent electrodes is circled in the upper middle of Figure 4.6c. The resistance between the top two electrodes in Figure 4.6c was 2.0 kΩ. The nanowire connecting the two electrodes measured 260 nm in length and 40 nm in width at the widest point. Figure 4.7a shows an example of an I-V curve obtained during electrical probing. The linearity of the plot suggests that the DNA origami nanowires exhibit typical ohmic behavior up to 1 volt. The breakdown current density was measured by ramping the voltage above 1 V. At 1.4 V the current dropped to zero. Right before failure the current density was 1.26×10^{12} A/m^2, which is similar to other breakdown current density measurements on DNA templated Au nanowires.[99]

The separation between the measured maximum and minimum resistances was approximately 1 kΩ as shown in Figure 4.7b. Half of the measurements gave resistance values of ~1.5 kΩ. Upon SEM inspection, the resistance values scaled roughly with the number of DNA origami bridging the gap. The values between 1.75 and 2 kΩ correspond to electrode sets with one origami nanowire bridging between electrodes, while measurements below 1.75 kΩ generally came from electrode pairs with two origami nanowires bridging the gap. Electrodes with

resistances near 1.5 kΩ generally were connected by two metallized DNA origami in which one (or both) had a region where the metallization was narrow (< 15 nm). Due to narrow regions in the nanowires, the resistance across the electrodes was larger than electrodes connected by two uniformly metallized DNA origami (~1 kΩ) but still less than electrode pairs with a single uniformly metallized DNA origami (~2 kΩ). It was determined that on average the resistance per DNA origami was 2.3 kΩ with a standard deviation of 0.6 kΩ (18 total metallized DNA origami were measured). Using the average resistance and the average measured nanowire width of 33.0 nm a resistivity value of 6.2 X 10^{-6} Ωm was calculated, which is in the same range as other reported values for both gold nanorods (3 X 10^{-6} Ωm)[100] and gold nanowires fabricated on linear double stranded DNA (values range from 4 X 10^{-8} Ωm to 2 X 10^{-4} Ωm).[97, 101] The resistivity value of nanowires demonstrated here is over 2 orders of magnitude higher than the bulk resistivity of gold (2.2 X 10^{-8} Ωm). Some resistivity increase can be expected from electron scattering from grain boundaries in the nanowires; additionally, poor connection between grains, defects, and impurities, possibly from the presence of nucleotides, could also contribute to the high resistivity. This is the first report showing the fabrication and electrical characterization of electrically conductive metallic structures templated by DNA origami. Thus, these results represent an important step towards enabling the use of DNA origami in the fabrication of functioning nanodevices.

Using DNA origami, my group members and I have demonstrated the ability to fabricate electrically conductive structures in a controlled geometry with feature sizes approaching the limitations of current industrial nanofabrication.[8] Such a technology can be useful in the fabrication of nanodevices for many applications. For example, in nanoelectronics this technique could be used to fabricate separated source, drain, and gate electrodes for transistors. In order to

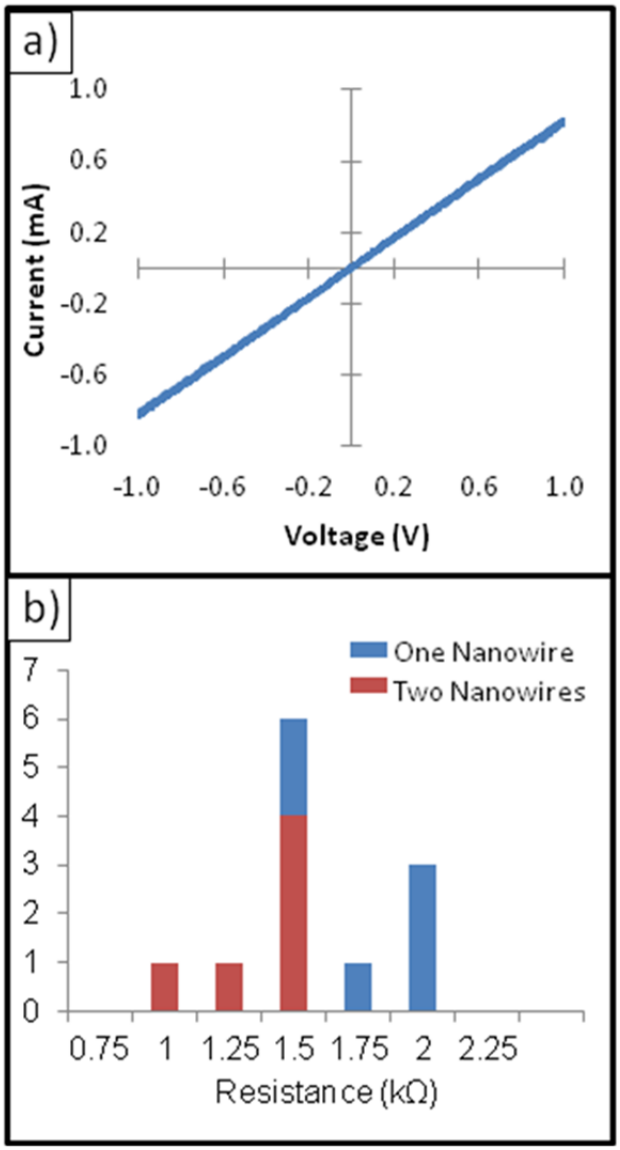

Figure 4.7. (a) Current-Voltage plot of an electrode pair with resistance of 1.25 kΩ, where the voltage was ramped from -1 V to 1 V. The device shows typical ohmic behavior over these voltages. (b) Histogram of 12 measured resistance values. SEM images show that devices with resistances less than 1.75 kΩ generally have two metallized DNA origami connecting between the two measurement electrodes.

create geometries useful for nanodevice fabrication, it is important to have the ability to design and control the location of separate metallized regions in the DNA origami structure. Here it is demonstrated that this is possible using the "T" DNA origami. The design of the DNA origami was adjusted so that the A_{10} extensions are only located on staple strands toward the ends of the

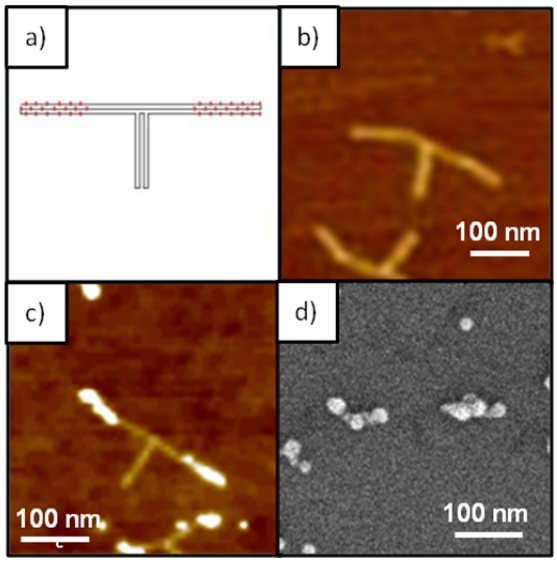

Figure 4.8. Images of the "T" shaped DNA origami with a programmed gap in which a semiconducting material could be deposited. a) A schematic of the "T" structure where the red markings show the location of attachment. b) Tapping mode AFM image of the unseeded "T" structure. The height scale is 4 nm. c) Tapping mode AFM image of seeded "T" structure where a gap is seen between seeded regions. The height scale is 6 nm. d) SEM image of the "T" DNA origami with a gap following metallization.

top portion of the "T" as shown in Figure 4.8a. Seeding and metallization of this structure results in a ~100 nm gap between metallized portions. AFM images of the unseeded and seeded, and metallized structure are shown in figures 8b, c, and d, respectively. A geometry such as this could be used to form a transistor if a semiconducting material, such as a semiconducting carbon nanotube, were inserted between metallized regions.

We have also designed a DNA origami structure for site-specific metallization that can serve as a template for a simple logic device. Each staple strand of the structure was extended on the 3' end with an A_{10} sequence with the exception of two gaps as shown in Figure 4.9a. The Au NP seeding and metallization steps described for the "T" DNA origami were repeated for this structure. AFM images of the unseeded and seeded structure are shown in figures 9b and 9c, respectively. As shown in Figure 4.9d, following metallization structures that have been formed

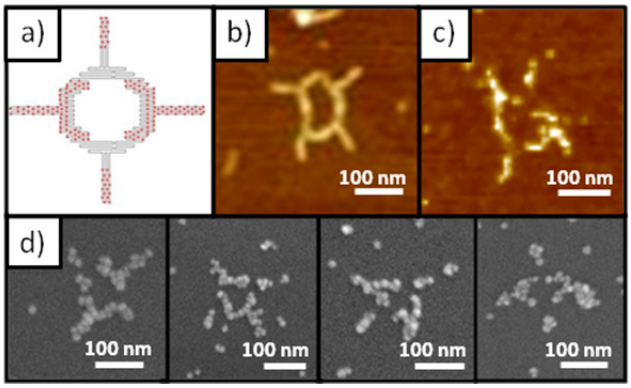

Figure 4.9. Logic gate prototype. a) The structure of the DNA origami design, where the red markings show the location of staple strand A_{10} extensions for attachment. b) Tapping mode AFM image of the DNA origami prior to seeding and metallization. Height scale is 4 nm. c) Tapping mode AFM image of seeded DNA origami. Height scale is 16 nm. d) SEM images of the prototype structure after the plating process.

and metallized correctly; however, in some cases leads appear to have linked with a neighboring electrode due to over metallization.

Some optimization of the metallization may be required to enhance the ability to create large numbers of successful structures. However, the attachment to the surface prior to seeding and plating, the structural stability, and aggregation of the DNA origami seem to be the most important parameters to increase the percentage of correctly formed structures. While the yield of correctly folded origami is high (~70%), fewer than 15% of the DNA origami are seen in a geometry similar to that shown in Figure 4.9a. The remaining DNA structures appear to have twisted or folded during the deposition process, which prevents the formation of a high yield of metallized structures after seeding and plating. To increase the yield, the stability of the DNA origami must be enhanced or alternate attachment mechanisms must be used which will help maintain the desired DNA origami shape and decrease aggregation. Additionally, further increase in yield may be possible by removing background Au NPs which are adsorbed to the surface and may affect the plating geometry if located near an origami structure. If the surface

contains binding sites in controlled locations where the origami are able to form a stable bond, the background could be cleaned using an aggressive rinsing technique. Optimization of these processes will enhance the ability to simultaneously fabricate very large numbers of successful structures as a basis for nanosystem fabrication and assembly.

In conclusion, my collaborators and I have demonstrated a method that uses site-specific attachment of gold nanoparticles and subsequent metallization to fabricate conductive wires from DNA origami templates. An important aspect of the work is the attachment of high densities of Au NPs onto branched DNA origami structures. These closely spaced Au NPs serve effectively as seeds for metallization to create continuous metallized segments or nanowires on origami templates. Continuity was verified via electrical measurements. Additionally, selective metallization was demonstrated on DNA origami to create geometries with controlled gaps, enabling future fabrication of a wide variety of nanodevices.

Chapter 5

Oxidation of Graphene Nanofuses for Long Term Write-Once-Read-Many Times Data Storage

5.1 Introduction

Current data storage technologies have limitations which prevent their use in archival data storage applications. For example, CDs, DVDs, flash memory, and hard disk drives generally provide data retention times of less than 10 years. [102-104] Members of my group have previously reported an archival data storage solution using optical techniques.[105] However, due to the high data density available in solid state devices a large part of the market share in memory has gone to electronic storage techniques. Flash memory specifically, has become increasingly popular, however, as device size has decreased, increasing efforts have been required in error correction methods to compensate for increasing error rates.[106-109] Here I investigate electronic solutions which can utilize the high data densities possible with solid state devices and have sufficient stability for archival applications.

Electronic archival data storage devices must maintain the high data density standards of flash memory, be highly stable in both the on and off states, ideally have a high on/off current ratio, and require a relatively low programming power.

Write-once-read-many (WORM) memory devices are promising for archival solutions. Generally, WORM devices store data by a physical change which alters the electronic properties of the device. This is in contrast to flash memory which uses electronically controlled changes in charge storage to alter electronic properties. In devices which use electronic changes to store

data, the programmed state is generally reversible, allowing the device to be erased and rewritten, while physical changes in WORM devices cannot easily be reversed. However, the irreversible programmed state of WORM devices makes it a good candidate for archival storage, where the goal is high stability.

Micro or nanoscale fuse (or antifuse) structures have often been proposed or used in WORM devices. With a large enough applied voltage, Joule heating causes the temperature of the fuse to increase until a change occurs in the fuse material (ex. melting, oxidation, reduction, etc) which causes the conductivity through the fuse to reduce (or increase) by many orders of magnitude.

Recent WORM fuse devices have been shown using conductive polymers and graphene oxide.[110-113] Conductive polymer fuses were shown to be programmed as they were heated between 100 ^{o}C and 200 ^{o}C by joule heating, where the conductive species was shown to be neutralized at elevated temperatures.[110] Graphene oxide has been shown to behave as an antifuse, where electron flow through the graphene oxide allows empty electron states are filled by the conduction electrons. Once the empty states are filled the conductivity of the graphene oxide increases drastically.[113] WORM fuse devices have also been fabricated using metals, oxides, and silicides.[114-116] However, inconsistencies in the conductivity of the off state, reconnection across programmed fuses, and environmental degradation has shown to limit the usefulness of many nanoscale WORM fuse devices for archival data storage.[117-120]

In order for nanoscale fuses to be stable for archival data storage needs the fuse material must have high chemical stability and low atomic or molecular mobility, which will prevent reconnection of the fuses or degradation of the fuse in both the on and off states. Additionally, fuse materials must have high enough electrical conductivity for Joule heating to generate high fuse temperatures without requiring too large a write voltage.

Graphene has a low atomic mobility illustrated by its high melting point (nearly 5000 ^{o}C),[6] is chemically resistant to any oxidation at temperatures up to 400 ^{o}C in an oxygen environment ,[7] and has good electrical conductivity.[121] These properties make graphene a strong candidate for applications in WORM devices with archival data storage applications. Here I report a study of graphene WORM devices which can be read and written electronically, can potentially have very high data densities, and can be programmed with low voltage and power.

A reversible graphene switch was shown recently by Standley et al, where it was found that by applying a sufficiently high voltage in a vacuum environment, a small break could be formed through a graphene ribbon.[122] After the break was formed, reconnection could be achieved by applying a voltage across the ribbon. The break could then be reformed by further increasing the voltage. In contrast, the goal of this work is to create a permanent break in the graphene rather than a reversible switch, where reconnection will not occur. From these results it is seen that by programming in an air environment nanoscale graphene fuses can be programmed with an applied voltage below 5 V at a power of 2 mW, where reconnection was not seen across any programmed fuse. Additionally, I have determined that decreasing the fuse size decreased the required programming voltage and power. Following programming, all fuses showed an on/off current ratio greater than 2 X 10^{6}. Finite element analysis was used to estimate the temperature required to program a fuse to be 400 ^{o}C.

5.2 Experimental Methods

Graphene was grown using chemical vapor deposition (CVD) on a copper substrate. This was done using previously reported techniques with a few modifications as follows.[42] First,

clean copper foils were annealed in an evacuated tube furnace at 900 ^{o}C in a hydrogen environment to reduce any copper oxide which had formed on the surface of the copper foil. Next, methane gas was flowed into the tube for 30 min to allow graphene to grow on the surface of the copper foil. The samples were then slowly cooled to room temperature. After the samples were removed from the furnace, PMMA was spin coated onto the copper/graphene surface at 3000 rpm. Next, the copper was removed as the samples were placed in a 83 mg/ml solution of sodium persulphate in water for ~15 hrs. PMMA/graphene films were removed from the copper etching solution and placed in a container of deionized H_2O where they were stored until use.

Fuses were fabricated on a (100) silicon substrate containing 200 nm of thermally grown SiO_2. First, pairs of 100 μm Au contact pads were fabricated on the substrate using electron beam lithography (see Figure 5.1a-b). A PMMA/graphene film was then placed on the surface and allowed to dry overnight. The PMMA was removed by placing the samples in a solution of 1165 Microposit Remover for 1 hr. The sample was then rinsed by immersion in a 1:1 solution of 1156 Microposit Remover and acetone for 1 min. Next, the sample was immersed in pure acetone for 1 min, removed from the solution, and allowed to dry for at least 1 hr. To form fuses from the graphene sheet, aluminum was patterned in the desired fuse geometry using electron beam lithography (see Figure 5.1c) on top of the graphene. The fuse geometry was transferred from the aluminum to graphene as previously reported by placing the sample in an oxygen plasma (2 min) to remove graphene which was not covered by aluminum. [123] The aluminum was removed by immersing the sample in a 100 mM KOH solution for 5 min (see Figure 5.1d). Samples were then rinsed by immersing in a bath of deionized H_2O for 1 min. To dry the sample without damaging fuse structures, the sample was removed from the bath and exposed to

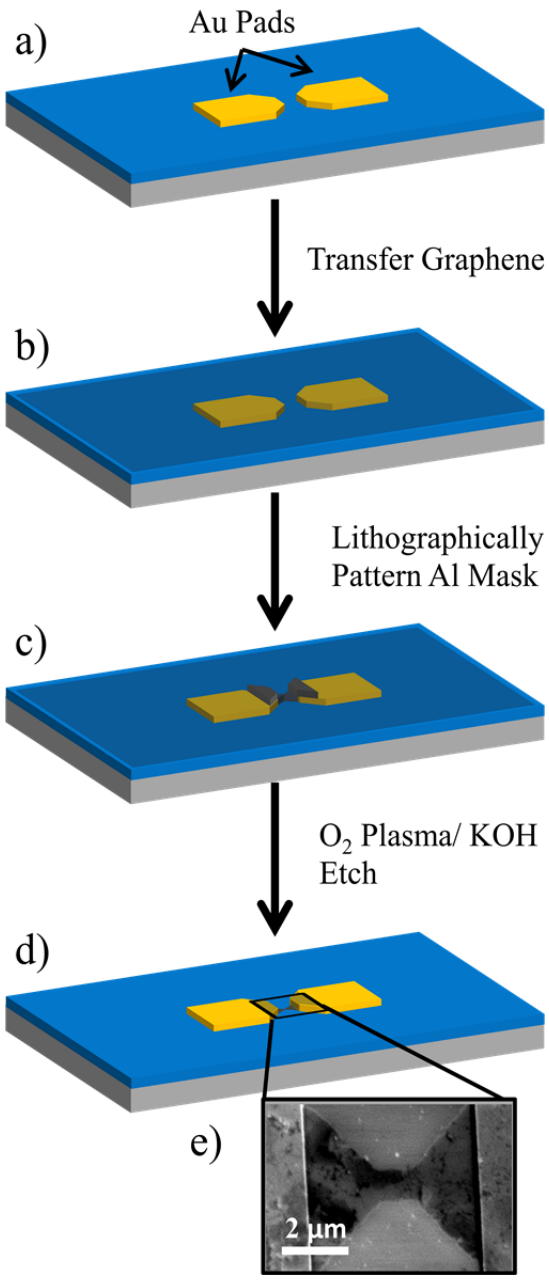

Figure 5.1. Schematic of graphene fuse fabrication. a) shows the Au pads prefabricated on the Si/SiO_2 substrate. b) Shows the substrate following transfer of sheet of CVD grown graphene. In c) an Al mask was patterned on top of the graphene layer in the desired geometry and location of the fuses. d) Shows the transfer of the Al pattern to graphene fuses using oxygen plasma cleaning and KOH etching. e) Shows an SEM image of a graphene fuse following the fabrication process.

isopropyl alcohol vapor until the remaining water had been driven off the surface. A scanning electron microscopy (SEM) image of a graphene fuse fabricated with this method is shown in Figure 5.1e.

The fuse geometry was varied as shown in Figure 5.2, where the width of the center narrow region (w) was either 1 μm or 250 nm. The distance between the Au pads (d) was also varied between 2.5 μm and 20 μm. To apply a voltage across the fuses, micromanipulator probes were placed on each gold pad and connected to either LabView (0 to 10 V) or an HP Harrison 6289A DC power supply (> 10 V). The voltage was ramped (~ 100 mV/s) while the current was measured either with an Ithaco picoammeter or a multimeter connected in series. During voltage testing, fuses were left in open lab air, so oxidation of fuses could occur when Joule heating had raised the fuse temperature sufficiently. SEM imaging was used to analyze fuse structures both before and after programming.

5.3 Results and Discussion

As the voltage was ramped across the fuses and the current monitored, in each fuse there was a point where the current dropped from a high to a low value (see Figure 5.3a), where the low value was always below that which could be measured by my ammeter (< 50 pA). I will refer to the voltage which caused this large change in resistance as the programming voltage. For fuses which had a 20 μm distance between Au pads I found that the programming voltage was 13.8 ± 3.5 V (@ 28 mW) for the 1 μm wide fuses and 9.5 ± 4.4 V (@ 8 mW) for the 250 nm wide fuses. Figure 5.3b,d show SEM images of a 1 μm and 250 nm fuse, respectively, before

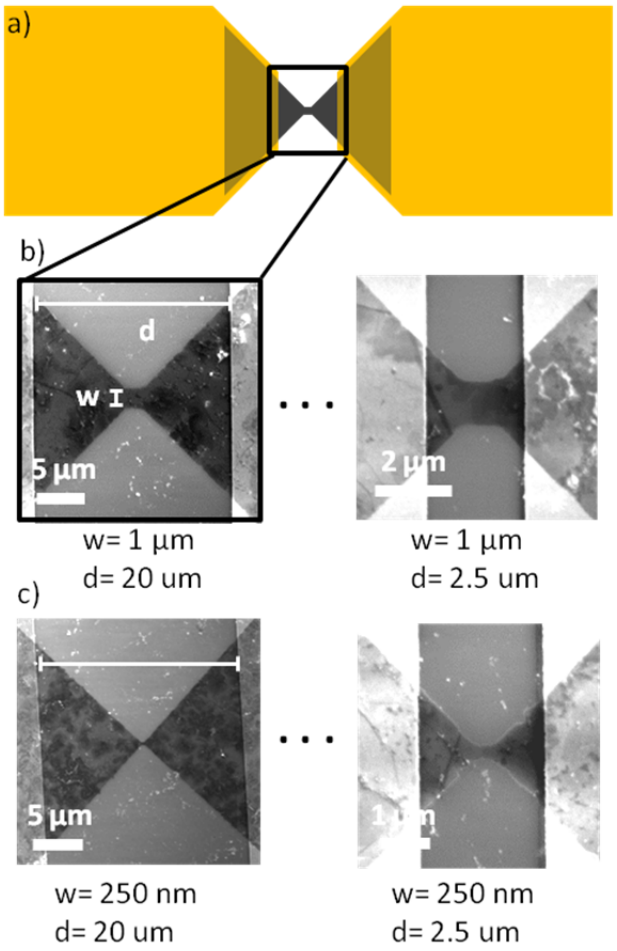

Figure 5.2. Schematic showing the fuse geometries used in graphene fuse tests. a) Schematic of the fuse structure where the Au contact pads are on the left and right sides and the graphene fuse is marked with the box. The light grey areas show where the graphene overlaps the Au pads to form electrical contact. b) As shown in the left image, w is the width of the narrowest region of the fuse, while d is the distance between Au pads. Marked below each image is the corresponding d values used for the w = 1 µm fuses. c) Marked below each image is the corresponding d values for the displayed w = 250 nm fuses. Additionally, for both the w = 1 µm and 250 nm fuses, fuses were fabricated with d = 10 µm, 5 µm, and 2.5 µm.

programming; Figure 5.3c,e show images of the same fuses in Figure 5.3 b,d, respectively after programming. In both of the programmed fuses there is a clear crack through the center. Interestingly, in both Figure 5.3c and e there is a contrast difference between the left and right side of the crack through the fuse. This was caused by the electron beam interacting with one side for a longer period of time, causing it to charge and appear brighter. This phenomenon was

not seen for non-programmed fuses, indicating that the gap formed during programming prevents flow of charge across the fuse.

As the voltage was ramped across 1 μm and 250 nm wide fuses which had distances between Au pads of 10, 5, and 2.5 μm the same programming behavior was seen with the required programming voltage and power being lower for the 250 nm fuses than the 1 μm fuses and decreasing with the distances between Au pads (see Figure 5.4a-b). The lower power and voltage necessary for fuses with smaller dimensions indicates a trend favorable for scaling fuses down to dimensions available with state-of-the-art optical lithography.

The voltage and power needed to program a fuse is dependent on the electrical and thermal properties of the graphene, and the temperature required to oxidize the fuse. The exact temperature necessary for oxidation of individual fuses may be influenced by the presence of grain boundaries, which can influence electrical and thermal properties of the graphene, and likely contain a high density of non-bonded carbon atoms, which may be more susceptible to oxidation. This could account for some of the variation in the programming voltage and power shown in Figure 5.4a-b. Additionally, following programming, the gaps across some fuses were seen to follow grain boundaries, indicating that the presence of these boundaries does have an effect on the programming process.

From the presented results I have found that scaling down the fuse geometry also affects the voltage required to program a fuse, where decreasing fuse width and separation between Au pads has shown to decrease required programming power. This indicates favorable scalability of graphene fuses, and gives evidence that graphene fuses are good candidates in high density data storage.

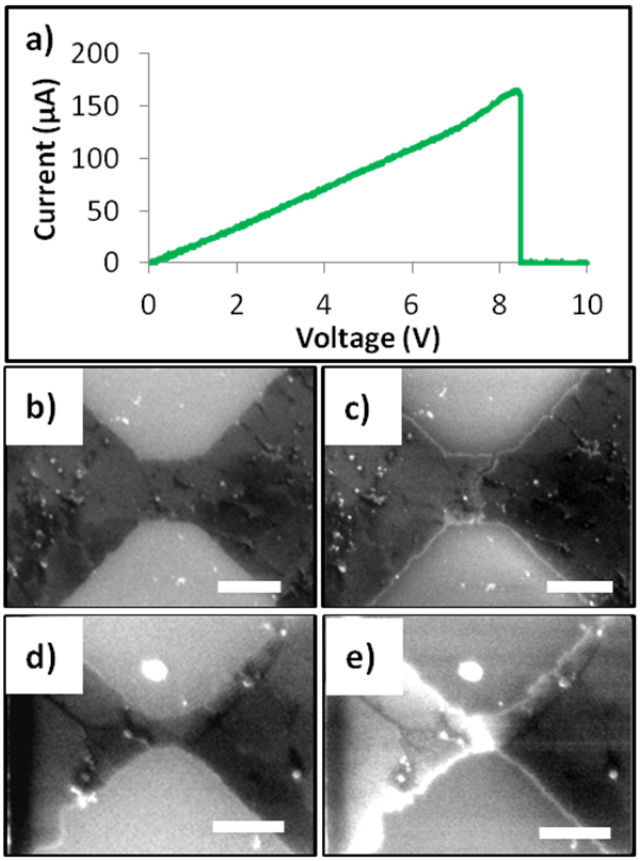

Figure 5.3. Programming graphene fuses using a ramped voltage. a) Shows a current-voltage curve for a typical graphene fuse, where the current dropped to zero at 8.5 V. The total current drop here is approximately 7 orders of magnitude. b) And d) show intact fuses that are 1 μm and 250 nm wide at the narrowest point, respectively. c) And e) show the fuses from b) and d), respectively, after programming. For these fuses the voltage was ramped at a rate of 100 mV/s. There is a clear break through the center of each fuse after programming. Due to higher electron emission at the edges, the break in e) appears as a bright line. Scale bars in b) and c) are 1 μm and scale bars in d) and e) are 500 nm.

In order to estimate the temperature of the fuses as they blow I have simulated fuses under an applied voltage using finite element analysis. In these simulations the steady-state temperature was determined for each fuse geometry using the programming conditions shown in Figure 5.4a-b. To match the simulated with the measured programming power, the electrical conductivity of the fuses was adjusted in the simulations so the electric current at the programming voltage was equal to the average measured electric current for each fuse as it was programmed. An estimate

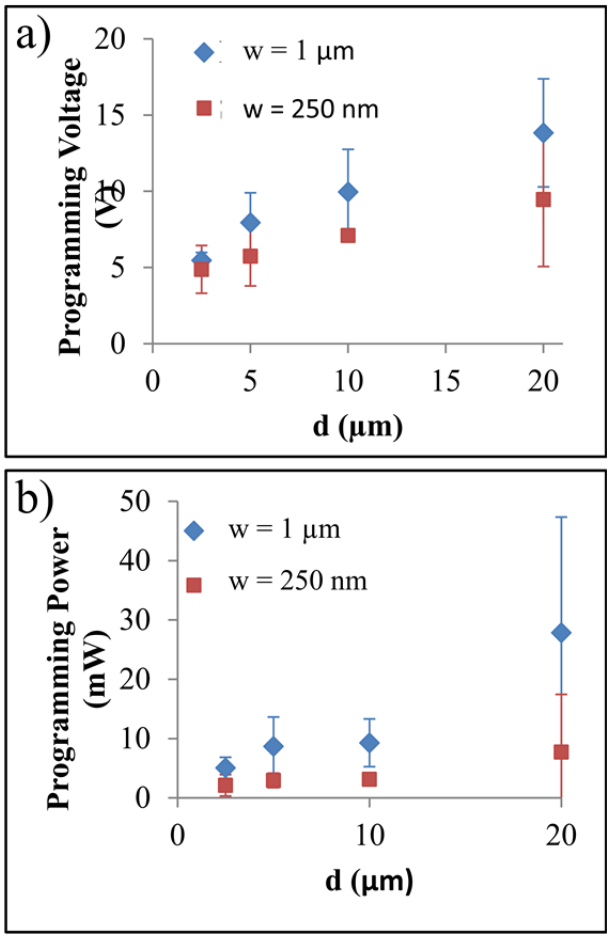

Figure 5.4. Programming characteristics based on fuse geometry. a) The programming voltage for fuses with widths of 1 µm and 250 nm for all tested values of d. The programming voltage consistently decreases for decreasing values of d. b) The programming power for fuses which are 1 µm and 250 nm in width for all tested values of d. The power decreases consistently as d decreases.

of the thermal conductivity value was obtained from the literature .[39] However, I found that the steady-state temperature of the 250 nm fuses was very sensitive to the thermal conductivity, so a more accurate value for the CVD graphene which we have grown was necessary. This was obtained by adjusting the thermal conductivity value in the simulation until the temperature of the 250 nm fuses matched the temperature of the 1 µm fuses, using the assumption that all fuses would be programmed at approximately the same temperature. Using this method I found the thermal conductivity to be approximately 3700 W/mK. Finally, the interfacial thermal

conductivity between the graphene and the thermally grown SiO_2 substrate was obtained from a report by Cai et al. and accounted for in the simulation by adding a thin thermally resistive layer between the graphene and SiO_2.[40]

Figure 5.5a shows the results of a simulation for a 250 nm fuse, where the gold pads were separated by 10 μm with a bias of 7.1 V. The temperature scale is shown above Figure 5.5a. From this graph it is seen that the heating is tightly localized in the center of the fuse, likely due to the fuse geometry and the thermal properties of graphene. Figure 5.5b shows a plot of the simulated steady-state temperature for each fuse geometry. To verify that these temperatures are in a range where oxidation of the CVD graphene occurs, I placed a sheet of graphene on an Si/SiO_2 substrate containing no Au pads and measured the sheet resistance (R_s) using a 4-point probe apparatus. Next, the substrate was heated to 350°C, 400°C, 450°C, and 500°C for 10 min each in a furnace open to the atmosphere. Between each temperature step, the sample was removed from the furnace and the sheet resistance was measured. Figure 5.5c shows the measured sheet resistance at each temperature. Here a slight decrease in sheet resistance is seen following heating to 350°C. At 400°C the sheet resistance nearly tripled and continued to increase as the temperature was increased further. At 500°C the film was too resistive to measure using the 4-point probe device (>1MΩ/sq).

From these measurements, it appears that oxidation began to occur between 350°C and 400°C. While the damage caused by oxidation to the graphene sheet was not sufficient to remove all conductive paths on the mm scale, it is reasonable that oxidation in a very small region would be sufficient to program the small scale fuse structures presented here.

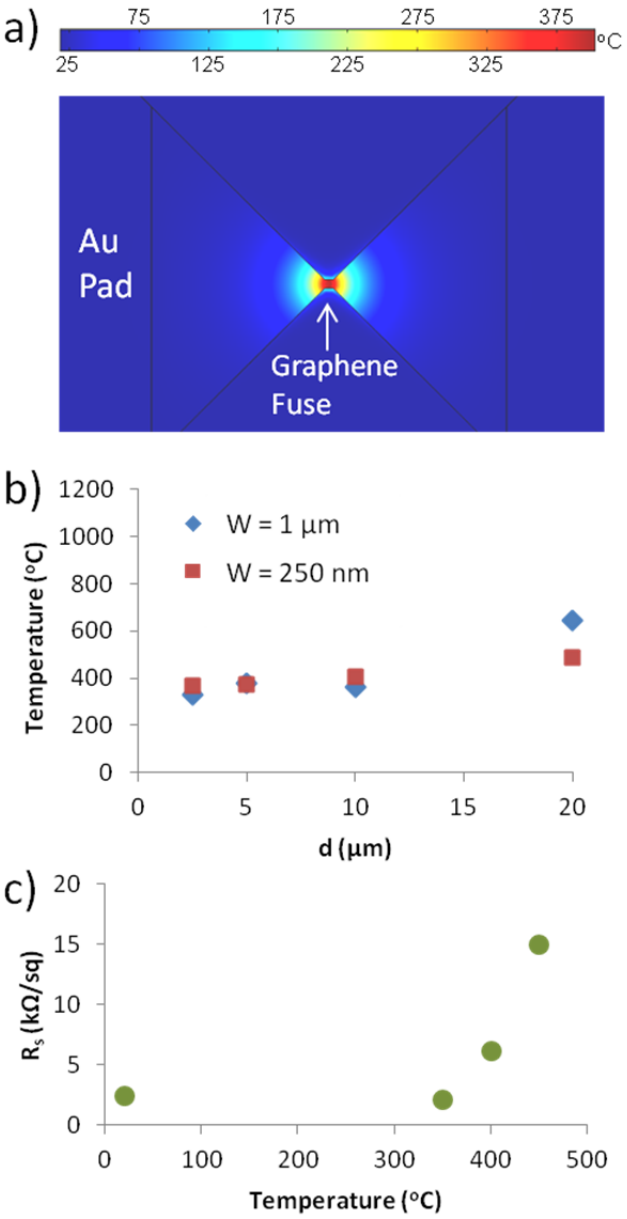

Figure 5.5. Expected fuse temperatures from finite element analysis and experimental verification. a) Shows a result for a finite element analysis simulation using a 250 nm wide fuse with a 10 µm distance between Au pads. For this fuse the simulated temperature was 404 ^{o}C. b) The computed temperature values for fuses of each geometry with the respective programming voltage applied. c) Experimental results showing the sheet resistance for a graphene sheet at after being heated to temperatures ranging from 350 ^{o}C to 500 ^{o}C for 10 min at each interval. The plot shows a large increase in R_s at 400 ^{o}C and further increase until the sheet resistance was too high to measure at 500 ^{o}C (>1 MΩ/sq).

Using the estimated programming temperature of 400 ^{o}C I used the finite element analysis method discussed above to verify that the voltage and power necessary for fuses to reach this temperature continue to decrease as feature sizes are decreased. For the electrical and thermal conductivity of graphene in these simulations average values of those described above were used. The fuse width was varied from 250 nm to 20 nm and the distance between contact pads was varied between 2.5 μm and 100 nm. In these simulations I saw that for a given contact pad separation, the programming voltage was constant over the range of fuse widths. As the contact pad separation was adjusted the programming voltage decreased slowly to a minimum of 4.05 V for a spacing of 100 nm (using a 20 nm fuse width). The programming power was seen to decrease with fuse width and contact pad separation until the contact pad separation decreased below 1.5 μm, where the required power and voltage were 900 μW and 4.4 V respectively for a 20 nm width. As the contact pad separation was decreased below 1.5 μm for each fuse width the programming power began to increase, where for a 20 nm fuse width the required power was 1.5 mW when the spacing between Au contact pads was decreased to 100 nm. I expect that this is due to increased temperature flow through the contact pads as they near the narrow portion of the fuse. It is not expected that the increased power requirement will limit the possible bit density of these devices, since the power requirement for the smallest geometry tested (20 nm width, 100 nm Au contact pad separation) was still low compared to other WORM devices (approx. 10 mW).[115] However, a vertical fuse geometry may be useful to increase the bit density beyond capabilities of this geometry.

In addition to developing WORM devices that can be programmed efficiently with low voltage and power requirements, the goal of this work is to create devices which will be stable for long periods of time. For stability in the non-programmed state fuses should not be

programmed unintentionally by exposure to high temperature environments or during reading. A programming temperature nearly 400^{o}C is sufficiently high that no high temperature environmental conditions can cause oxidation in non-programmed fuses.

To create fuses that are highly stable in the off state it is desirable that the break across the fuse is as large as possible. A step voltage of 15V in amplitude was applied across a fuse which was 250 nm in width with Au pads spaced at 2.5 μm. This voltage is approximately 3 times larger than the minimum required programming voltage for this geometry (see Figure 5.4a). Figure 5.6a shows the 250 nm fuse before it was introduced to the step voltage. Figure 5.6b shows the fuse from Figure 5.6a after the step voltage was applied. A gap measured to be 95 nm in width was formed in the center of the fuse after the applied step voltage. This gap is much larger than any formed during voltage ramping experiments (~5 nm), showing that larger gaps can be formed by increasing the applied voltage and by using a voltage step rather than ramping.

Stability of the programmed and non-programmed fuses was tested by applying 10 V across the programmed fuse shown in Figure 5.6b and 1 V across a non-programmed fuse for 90 hours each. Assuming a read time of 100 ns, this amount of time corresponds to more than 3×10^{12}read cycles. The results of these tests are shown in Figure 5.6c. Over the test period, although the on current fluctuates a little, an on to off ratio of greater than 10^6 is maintained.

Both the programmed and non-programmed fuses showed high stability throughout the experiment. The temperature of the non-programmed fuse at 1V was estimated using the finite element analysis method to be approximately 40^{o}C. At this temperature the fuse can be expected to be stable for very long periods of time, since no oxidation will occur at such a low temperature. Additionally the stability of the programmed fuse appeared very good as no current above the noise level was measured throughout the experiment.

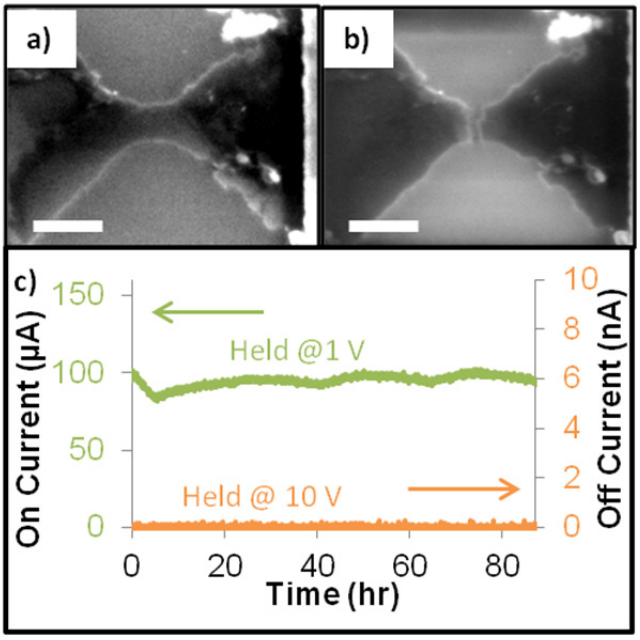

Figure 5.6. Programming fuses with larger gaps and stability measurements. a) Shows SEM images of a 250 nm wide fuse with Au contact pads spaced at 2.5 μm. b) Shows the fuse from a) after it has been programmed with a step voltage of 15 V. c) Shows a plot of the programmed fuse from b) and a fuse of the same geometry which had not been programmed with as the indicated voltage is applied for 90 hours. A fuse with the same geometry as a) and b) was used as the on state fuse. Scale bars are 500 nm.

In conclusion, I have performed experiments demonstrating that graphene fuses for use in WORM applications can be written with very low voltage and power requirements, where scaling the fuse dimensions to those available with state-of-the-art optical lithography will further decrease the required power and voltage. Next, using finite element analysis the temperature necessary to program these fuses was determined to be near 400^{o}C. Additionally, I showed that large breaks in fuses can be created by increasing the programming voltage. Finally, the fuse stability was verified by applying 10 V across a programmed fuse and 1 V across a non-programmed fuse for 90 hours each, and found both to be extremely stable over this test period.

Chapter 6

The Effect of Material Properties and Geometry on the Performance of Nanoscale Fuses for Long Term Write-Once-Read-Many times Data Storage

6.1 Introduction

A nanoscale fuse structure is a geometry that is commonly used for write-once-read-many times data storage devices.[114-115, 124] In In the geometry shown in Figure 6.1, the narrowest region of the fuse is the portion with the highest resistance. Programming of a fuse structure occurs by applying a voltage accross the fuse, which causes the temperature to rise in the narrow region due to Joule heating. If the voltage is large enough in magnitude this region will heat up sufficiently to cause disconnection across the fuse, which can occur as a result of melting and moving, oxidation, electromigration, etc.

For an effective long term memory device, a fuse material must be chosen that, when programmed, will undergo a large physical or structural change which will inhibit reconnection across the blown portion of the fuse. Additionally, low power and voltage requirements would be beneficial for a more efficient device.

The necessary fuse temperature for programming is dependent on the programming mechanism, which can vary depending on the material chosen as fuse material. The temperature of a given fuse is influenced by the magnitude of the applied voltage, the electrical and thermal

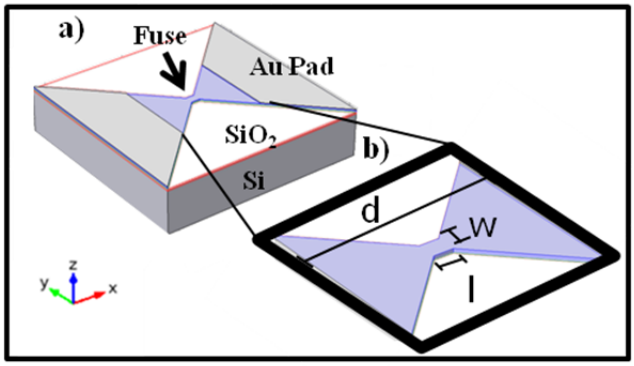

Figure 6.1. Fuse Geometry. (a) The entire fuse, with Au contact pads at each end of the fuse region, and (b) an expanded view of the fuse region. Marked are some geometric parameters of interest including the fuse width (w), length (l), and distance between Au pads (d).

transport properties of the fuse material, the size and shape of the fuse region, and the distance of the fuse from contact electrodes, which generally have good heat transfer properties. To determine optimal fuse material properties and geometry, I report a study on the effect of material properties, fuse geometry, and applied voltage on fuse programming, where two methods were used to analyze fuse properties: a simple analytic model and finite element analysis simulations. Additionally, a comparison is shown of these results to data from micro and nanoscale fuses I have fabricated.

My results suggest that materials with low thermal conductivity and high electrical conductivity are ideal for fuses to reach high temperatures under a low voltage bias. Additionally, results show that in general, fuse temperature increases for decreasing fuse dimensions.

6.2 Methods

To determine the effect of electrical and thermal conductivity of the material on the fuse temperature the fuse geometry shown in Figure 6.1 was used. To estimate the temperature of a fuse under a 10 V bias the fact is used that at steady-state:

$$P_{in} = P_{out}, \tag{6.1}$$

where P_{in} is the power created by Joule heating of the fuse held at 10 V, and P_{out} is the heat flow out of the fuse. P_{in} can be expressed as:

$$P_{in} = \frac{V^2}{R}, \tag{6.2}$$

where V is the voltage drop across the fuse region and R is the resistance of the fuse, which is dependent upon the electrical conductivity, the fuse width (w), length (l), and distance between electrical contacts to the fuse (d; see Figure 6.1).

To determine P_{out} Newton's law of cooling was used which describes heat flow from regions of high temperature to regions of low temperature. An example of Newton's Law of cooling for a simple geometry is shown in figure 6.2a, where the heat flow (dQ/dt), from the hot to cold region can be described by:

$$\frac{dQ}{dt} = P = C\Delta T, \tag{6.3}$$

where P is the power, C is the thermal conductance (based on the thermal conductivity, cross sectional area (A) and length of the material (L)), and ΔT is the difference between T_{hot} and T_{cold}. For the geometry shown in Figure 6.2a the thermal conductance is simply $C = kA/L$, where k is the thermal conductivity of the material, A is the cross sectional area, and L is the length. To use

this law to obtain a simple expression for P_{out} it was assumed that there is negligible heat transfer in the +z-direction and y-directions. For the + z direction this is expected since heat will not be transferred quickly through the air due to its low thermal conduction and the slow nature of convective heat transfer. For the y-directions minimal heat flow is expected since near the center of the fuse (where the Joule heating occurs) most of the fuse material lies in the x-directions, limiting heat transfer in the y-direction. Using these assumptions a simplified fuse geometry can be used as shown if Figure 6.2c. By applying equation (6.2) to this geometry the power out of the center of the fuse in the x ($P_{out,x}$) and z ($P_{out,z}$) directions can be defined as:

$$P_{out,x} = 2C_x\Delta T, \text{ and} \tag{6.4}$$

$$P_{out,z} = C_z\Delta T, \tag{6.5}$$

where now ΔT is the difference between the temperature of the heated fuse (T_{fuse}) and room temperature (T_{room}), and C_x and C_z are the thermal conduction in the x-direction (through the fuse material), and z-direction (through the SiO_2 substrate), respectively. C_x is dependent upon the thermal conductivity of the fuse material, the thickness of the fuse material, and the effective length (L_{eff}) shown in Figure 6.2c. C_z is dependent on the thermal conductivity of the SiO_2 substrate, the SiO_2 thickness, and the effective area of the heated region. Using Equations (6.4) and (6.5), the total power out of the center of the fuse can be defined as,

$$P_{out} = C_z\Delta T + 2C_x\Delta T. \tag{6.6}$$

By inserting Equations (6.6) and (6.2) into Equation (6.1) and using $\Delta T = T_{fuse} - T_{room}$, T_{fuse} can be determined to be:

$$T_{fuse} = \frac{V^2}{R(C_z+2C_x)} + T_{room}. \tag{6.7}$$

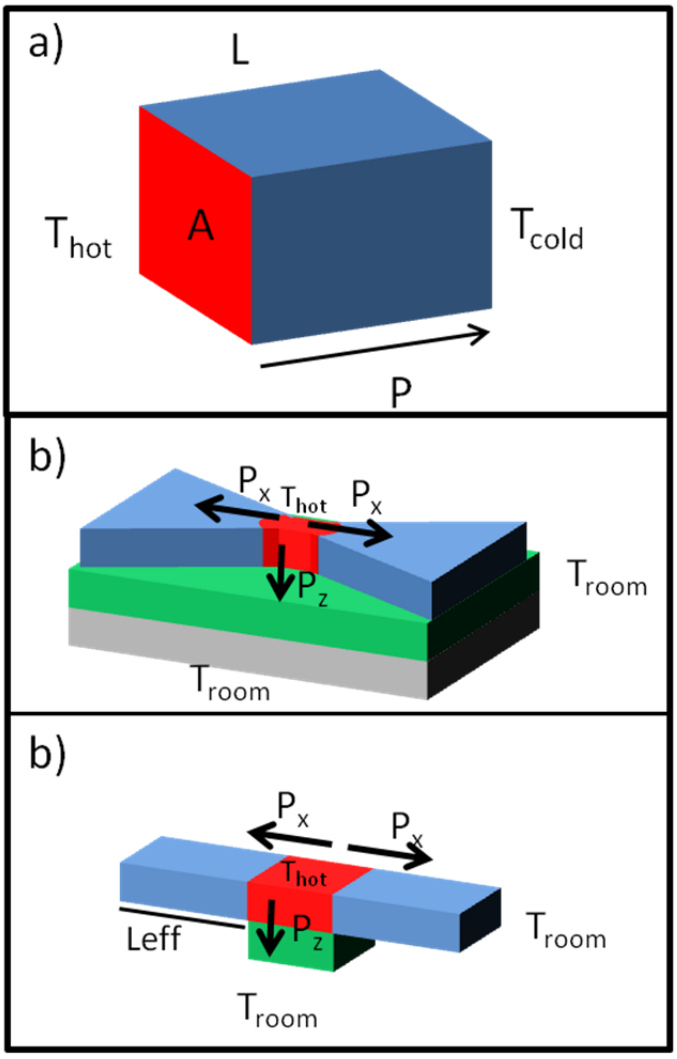

Figure 6.2. Applying Newton's law of cooling to aid in temperature modeling of the fuse material. a) Shows a simple geometry demonstrating heat transfer from regions of high temperature to low temperature based on Newton's law of cooling. The power loss is dependent on the temperature difference between the hot and cold region (T_{hot}-T_{cold}), the length (L) and cross sectional area (A) of the material between the hot and cold regions. b) Shows the expected heat flow outward in the x-directions (P_x) and z-direction (P_z) from the region in the center of the fuse which is heated by Joule heating. c) Shows the simplified fuse geometry used to calculate power transfer from the heated region of the fuse using Newton's law of cooling.

6.3 Results and Discussion

Using Equation (6.7), the temperature was plotted as a function of electrical and thermal conductivity for a fixed fuse geometry under a 10 V bias (see Figure 6.3). This plot shows that

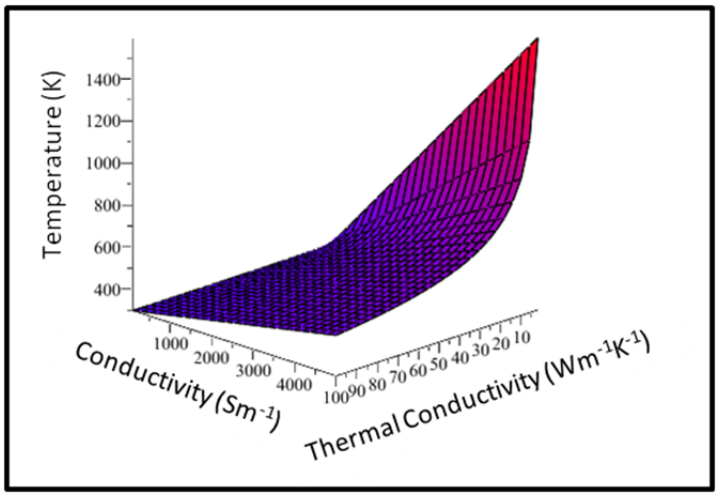

Figure 6.3. 3D surface plot of temperature vs. material thermal and electrical conductivity for a nanoscale fuse with 10 V applied across the fuse.

materials with high thermal conductivity and low electrical conductivity do not reach high temperatures under this applied voltage, while fuses with low thermal and high electrical conductivity reach much higher temperatures. One useful application of this model is to estimate the required programming voltage if the required temperature to program a fuse in known. For example, assuming the fuse material must reach 1000 K before being programmed and has electrical conductivity and thermal conductivity values of 3000 S/m and 10 W/mK, respectively, the voltage required for the fuse to reach this temperature can be calculated to be approximately 13 V.

To verify these predictions, I fabricated nanoscale fuses from Te, a higher electrical conductivity proprietary Te alloy, and W on silicon surfaces that had 200 nm of thermally grown SiO_2. Prior to fuse fabrication Au contact pads were fabricated using conventional electron beam lithography techniques. The fuses were fabricated, also using electron beam lithography, to allow connection between Au pads as shown in Figure 6.4. Next, the fuses between the Au pads were defined. The fuse materials were then sputtered at thickness of 200 nm of Te, 200 nm of Te

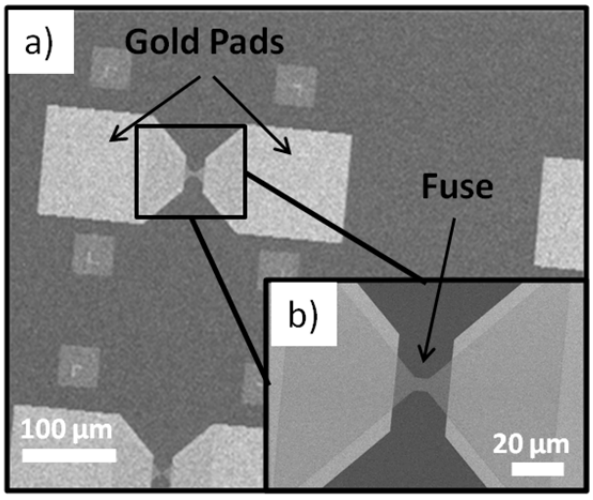

Figure 6.4. Fuses fabricated using electron beam lithography. a) Shows the entire structure where Au pads are fabricated to provide low resistance contact for probing using micromanipulator probes. The Te fuse is fabricated between the Au pads. b) Shows a closer view of the fuse geometry between the Au pads. The fuse in this image is 5 µm wide at the narrowest point. The fuses in this figure are made from Te.

alloy, or 50 nm of W. The remaining e-beam resist was then removed by immersion in 1165 Microposit remover. After lift-off, samples were rinsed in isopropyl alcohol and dried in a stream of air.

Fuses were programmed by placing micromanipulator probes on the Au contact pads and connecting to an external power supply. The current was monitored as a voltage was applied across each fuse. The voltage was applied by ramping at a rate of 100 mV/s until the current dropped precipitously. The voltage where the current drop occurred was recorded and compared with voltages predicted by the simple analytic model. During ramping, the Te and Te alloys showed a drop from a high current to a current too small to measure with the picoammeter. This occurred at 7.5 V and 2 V for the Te and Te alloy, respectively. The tungsten fuses had a resistance change of about 1 order of magnitude after ramping to 4 V, but the current never dropped to zero. Figure 6.5a,c, and e show scanning electron microscopy (SEM) images of Te, Te alloy, and W fuses after programming. Interestingly, fuses programmed by ramping had a gap

that was offset from the center of the fuse, probably due to electromigration of the material as it heated up.

The simple analytical model discussed above was used to estimate voltages required to program fuses. Results of these tests are shown in Table 6.1 as well as the electrical conductivity (σ), thermal conductivity (k), and melting point (M.P.) of each material. These results show close agreement between the voltage predicted by the model and the voltages determined from ramping experiments.

Material	k (W/mK)	σ (S/m)	M.P. (K)	Voltage (V)	Predicted Voltage (V)
W	170	2×10^7	3700	4	3.4
Te Alloy	5*	1.6×10^5**	670*	2	2.2
Te	3	1×10^4	750	7.5	8.3

* Value estimated
** Value measured

Table 6.1. Shows material properties of each fuse material tested. The column labeled "Voltage" shows the programming voltages determined by ramping experiments of fabricated fuses. The "Predicted Voltage" column shows the programming voltage predicted by the simple analytic model based on the electrical conductivity (σ), thermal conductivity (k), and melting point (M.P.) of the fuse material.

To determine the effect of larger applied voltages on fuse programming, step voltages of 20 V, 7.5 V , and 10 V were used for the Te, Te alloy, and W, respectively. SEM imaging of fuses following application of a step voltage (see Figure 6.5b, d and f) showed formation of much larger openings than those programmed by voltage ramping. Holes formed in this process were located directly in the center of fuses. This may be explained by the higher voltage causing rapid melting and movement of material which caused disconnection across the fuse in a shorter time than required for electromigration to occur.

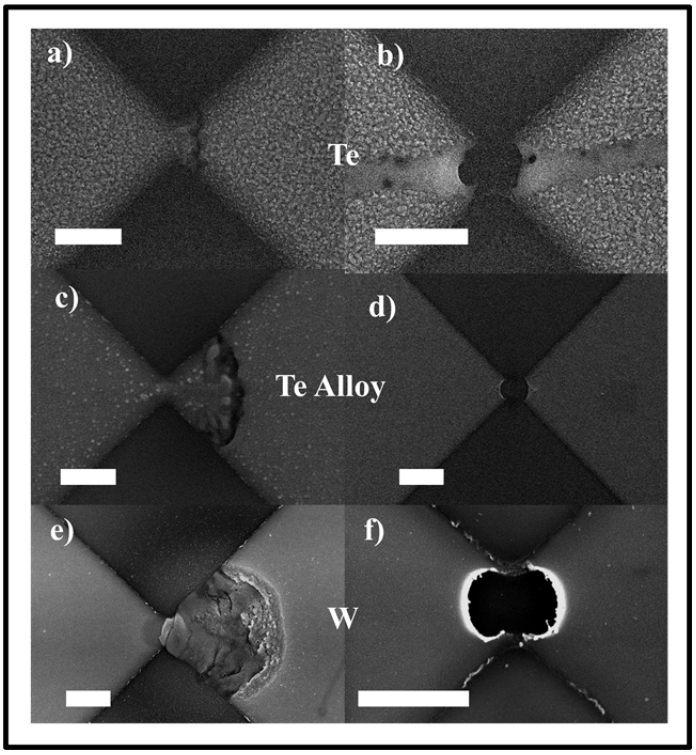

Figure 6.5. Programming of fuses composed of Te, Te alloy, and W. (a), (c), and (e) show Te, Te alloy, and W fuses, respectively, which were blown by ramping the voltage until an order of magnitude or more change in current was seen. (b), (d), And (e) show Te, Te alloy, and W fuses, respectively, which were blown by applying a step voltage of 20 V ,7.5 V, and 10 V for (b), (d), and (f), respectively. Scale bars are 1 um.

Finite element analysis was done using COMSOL Multiphysics software version 4.2, to determine the effects of the width of the narrowest region of the fuse (w), the length of the narrow region (l), and the distance between gold contact pads (d) (see Figure 6.1). The properties of Te were used for the fuse material in all simulations.

To determine the effect of applied voltage on fuse temperature, the steady-state temperature was recorded as the voltage was varied between 1 V and 15 V. The geometry was held constant for each of these simulations. Figure 6.6a shows the results of this study. This plot shows that the temperature increase like V^2, which is consistent with Equation (6.7).

Next, the effect of fuse width was determined using finite element analysis. In these simulations the width was varied from 500 nm to 10 μm. The narrow portion of the fuse was held square (w = l), while the voltage and other geometry parameters remained constant. Results displaying the effect of fuse width on fuse temperature are displayed in Figure 6.6b. These results show an inverse relationship between the temperature and fuse width. This can be expected from Equation (6.7) where the fuse resistance is inversely proportional to the fuse width, and the thermal conductance (in the z-direction) is proportional to the fuse area (w^2) . From this the following relationship between the temperature and width is expected.

$$T_{fuse}(w) \propto \frac{1}{R\left(\frac{1}{w}\right)C_z(w^2)} \rightarrow T_{fuse}(w) \propto \frac{1}{w}, \tag{6.8}$$

which shows the expected inverse relation between temperature and width.

To determine the effect of fuse length on temperature, the length of the narrow portion of the fuse was varied from 500 nm to 10 μm. The results of finite element simulations determining the effect of fuse length on temperature are displayed in Figure 6.6c, where there appears to also be an inverse relationship with the fuse length; however, by comparing Figure 6.6b and 6.6c I find that variation in length does not have as high of an impact on the fuse temperature as does the width.

Finally, the dependence of temperature on spacing between contact pads was examined by varying the spacing between 500 nm and 20 μm. These results are displayed in Figure 6.6d. Here a large dependence of the temperature on spacing between Au pads is seen. From the model, the resistance of the fuse is proportional to the spacing between Au pads. However, I do not expect the heat flow out of the fuse to be dependant on the Au pad spacing (d), which is accurate in cases where d>>w. Thus the finite element simulations match expected results based on the analytical model.

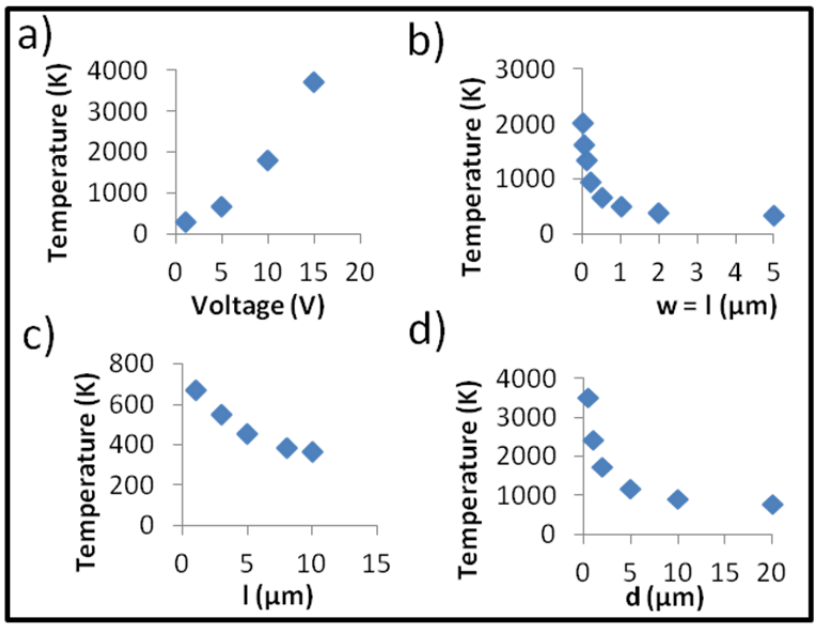

Figure 6.6. Simulated temperatures across fuses as: (a) the voltage is varied from 1 to 15 V; (b) the width and length (w and l) are varied from 20 nm to 5 µm; (c) the length of the fuse is varied from 500 nm to 10 µm; and (d) the separation between contact pads is varied from 500 nm to 20 µm.

The goal of these simulations was to aid in the optimization of fuse geometry to decrease power and voltage requirements. From simulations, which agree qualitatively with the simple analytical model, it is expected that decreasing fuse dimensions (including width, length, and separation between contact pads) will allow lower programming voltages to be used.

To verify that the required writing voltage and power should decrease with fuse size, I have fabricated Te fuses using electron beam lithography as described above. The fuses were fabricated so the narrow portion remained square (l = w), and the width was varied from 10 µm to 500 nm. The value of d for each device was fixed at 20 µm. The required programming voltage was determined by ramping the voltage across the fuses as described above. Figure 6.7a-d show SEM images of the fuses after they were programmed. It can be seen from Figure 6.7e that the voltage required to blow fuses decreased as the fuse size decreased, which follows the

predictions of the simulations. Interestingly, analysis of the fuse blowing data showed that each fuse was programmed at the same P/w ratio. This empircal relationship indicates that for this range of geometries Equation (6.6) can be simplified to be:

$$P_{out} = BwT_{Fuse}, \tag{6.9}$$

where w is the fuse width and B is a constant depending on the thermal conductivity and thickness of the SiO_2 substrate and fuse material. Putting Equations (6.9) and (6.2) into (6.1) and and solving for the fuse temperature gives:

$$T_{fuse} = B\frac{V^2}{wR}. \tag{6.10}$$

We expect that the temperature required to blow the fuse is constant for all fuse sizes for a given fuse material. This allows this relationship to be used to predict the voltage required to blow Te fuse by setting the right-hand-side of Equation (6.10) equal to a constant. Combining all of the constants and solving for the voltage results in the following relation:

$$V = \sqrt{CwR}, \tag{6.11}$$

where C is now the power per width that was measured in my experiments. To predict the programming voltage the fuse resistance must be used, which for the bowtie geometry in Figure 1b is:

$$R = {}^{\rho}/_{t}\left[1 + \ln\left({}^{d}/_{w}\right)\right], \tag{6.12}$$

where ρ is the resistivity of the fuse material and t is the thickness of the fuse material. Inserting Equation (6.12) into (6.11) results in a simple expression for the voltage required to blow each fuse as a function of the geometry (for fuses where w = l) as follows:

$$V = \sqrt{{Cw\rho}/{t}\left[1 + \ln\left({}^{d}/_{w}\right)\right]}. \tag{6.13}$$

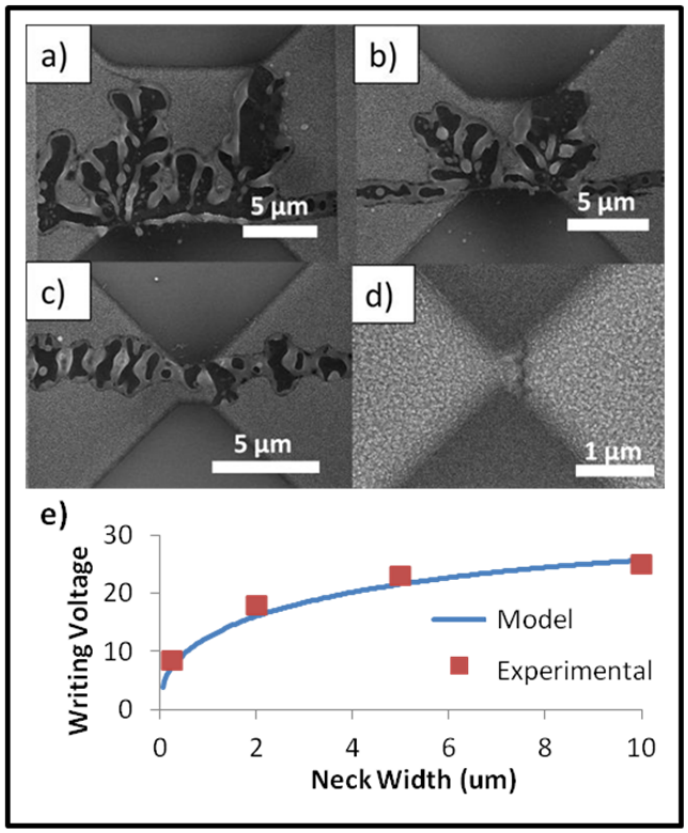

Figure 6.7. (a), (b), (c), (d) Blown Te fuses with original widths of 10 µm, 5 µm, 2 µm, and 500 nm, respectively. (e) Theoretically and experimentally obtained voltages required to blow fuses with these widths.

Figure 6.7e shows the experimentally obtained voltages and the voltages predicted using Equation (6.13), Good agreement is seen for each fuse size, indicating the utility of this model for predicting programming voltages of fuses with dimensions in this range.

To determine the expected voltage and power requirements for fuses which are smaller than those fabricated here I have used finite element analysis to estimate the voltage required to program fuses between 250 nm and 20 nm in width and spacing between Au pads down to 100 nm. In Figure 6.8a it can be seen that required programming voltage for fuses with widths between 250 nm and 20 nm is fairly independent of fuse width but, decreases slightly as the gap between Au pads is decreased. The required programming power shown in Figure 6.8b is seen to

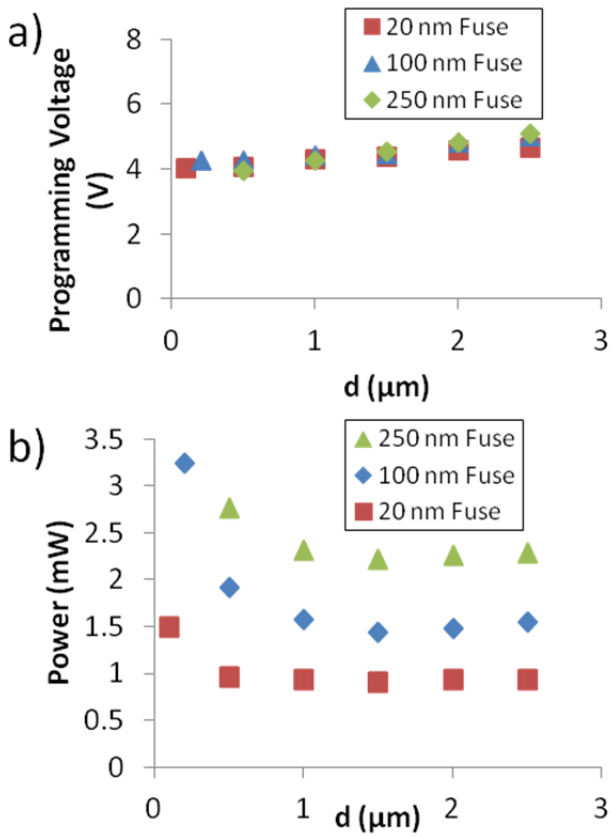

Figure 6.8. Simulated programming voltage and power for nanoscale fuse geometries obtained by finite element analysis. (a) Shows simulated programming voltages for 20, 100, and 250 nm fuses as the spacing between Au pads (d) is decreased. b) Shows the power required to program fuses of the same geometries as shown in (a). It is seen that as Au pads are brought closer than 1.5 µm, the required programming power begins to increase.

consistently decrease for decreasing fuse. As the gap between Au pads was decreased a decrease in required power is seen until the Au pads are 1.5 µm apart. However, for Au contact pad spacings below 1.5 µm the required power began to increase. It is expected that this increase in power as the Au pads become closer is a result of increased heat flowing into the Au pads.

The finite elements analysis results which show increase in power as the Au contact pads are moved closer than 1.5 µm cannot be predicted by the simple analytical model, and therefore provides a good example of an advantage of finite element analysis over the analytical model.

Finite element analysis provides accurate solutions based on a correct representation of the fuse geometry, which allows more reliable prediction of device behavior over a more broad range of geometries. In contrast, the analytical model provides useful qualitative information and accurate estimations for certain ranges of geometries (as shown in Table 6.1), and provides convenience since results can be obtained much more quickly than with finite element analysis.

In conclusion, I have determined that the electrical and thermal conductivity of the material chosen for nanoscale fuses strongly affect the fuse performance. Fuse materials with high electrical and low thermal conductivity allow fuses to be programmed with lower power. In addition to electrical and heat transport properties, other material properties, such as melting point, are important to consider.

Additionally, I have performed finite element analysis simulations to determine the influence of the applied voltage and geometry of nanoscale fuses on the temperature of fuses for applications in solid state data storage. I have determined that decreasing fuse size allows programming at lower voltages and have verified this experimentally. Additionally, simulations suggested that the distance between contact pads plays a large role in the heating of the fuse, where optimized spacing allows more heating and consequently lower power is required for programming.

Chapter 7

Conclusions and Future work

This work has allowed a great deal of progress in the fields of self-assembled electronic device fabrication and archival data storage. The goal of each project was to develop processes which will aid in efforts to allow integration of DNA origami, block copolymers, and graphene into nanoscale electronic device manufacturing. In efforts to fabricate DNA templated electronics I have worked to enable device fabrication in 3 ways: (1) development of a DNA origami surface attachment method to nanoscale binding sites and analysis of attachment to these sites; (2) development of a technique which can accurately control the location of binding sites; and (3) development of methods to fabricate and characterize conductive nanowires from a DNA origami template, which was done in a collaborative effort with other students and faculty. These processes are essential to allow fabrication of functional electronic devices which can be wired both locally and globally.

My work on development of archival data storage devices has shown that graphene is a promising material based on its high chemical and thermal stability as well as its electrical properties. This work showed that graphene fuses can be programmed with low voltage and high conductivity and exhibit high stability under an applied voltage for up to 90 hours.

Although significant progress has been made to fabricate nanoscale electronic devices, there is a great deal which can be done to improve and develop processes to enable fabrication of high yields of functional devices. Below I have listed future projects that could be done based on the

DNA origami and block copolymer work presented in chapters 2 - 4 , the graphene memory devices discussed in chapter 5, and the nanoscale fuse modeling discussed in chapter 6.

7.1 DNA Origami and Block Copolymers

To fabricate functional electronic circuits using DNA origami templates, additional methods must be developed to:

(1) refine methods used for placement and orientation control of DNA origami on a surface,

(2) allow the use of DNA origami as a template for patterning highly conductive nanowires and semiconducting materials, and

(3) enable electrical connection to DNA origami templated circuits to allow both local and global wiring.

7.1.1 Refinement of DNA Origami Placement and Orientation Control

Refinement of the processes which I have presented will require a study of DNA origami attachment to the patterned nanoparticles which I have discussed in chapter 3. Attachment to the patterned lines or groups of particles will likely require different process conditions than shown in chapter 2, where attachment was done to arrays of particles across entire surfaces. The two main differences between attachment sites discussed in chapter 2 from those discussed in chapter 3 are their composition and density on the surface. The differing composition (Au in chapter 2 vs. Pd in chapter 3) will require a study to ensure complete reduction of the Pd prior to attachment. Additionally, the time necessary for thiol reaction to occur on Pd may differ from

times used for gold nanoparticles. Next, the substantially lower densities of nanoparticles on the patterned surfaces will likely require longer attachment times or higher origami concentrations will increase the probability of interaction and binding between the origami and the nanoparticles.

To gain precise control of the location of origami, there must be optimization of the BCP generated nanoparticle patterning process to ensure that the particles are positioned accurately with no defects. This will require optimization of the sizes of electron beam lithography patterns; additionally, an annealing step may be required to remove the defects inherent in micelle patterning. Investigation of non-micelle based BCP patterning techniques may be necessary to form patterns with fewer defects.

Orientational control of the DNA origami is also necessary when fabricating electrical devices which are not symmetric. In order to use the BCP generated nanoparticle binding sites for orientational control a technique must be developed which will allow modification of individual nanoparticles within a particle pair with a different attachment sequence. This can likely be done using a top-down lithography method. Next, modification of origami to have two different sticky end sequences, each complementary with one of the sequences on the nanoparticles, base pairing attachment will allow the origami to attach in only the one orientation.

7.1.2 DNA Origami as a Template for Highly Conductive Nanowires and Semiconducting Materials

In order to allow sufficient current to pass through DNA templated nanowires, it is desirable that the conductive portions in the origami be as conductive as possible; however, the resistivity of the DNA origami templated nanowires measured in chapter 4 was ~2.5 orders of magnitude higher than expected for bulk gold. One route to reduce the resistivity is to optimize the metallization process. To accomplish this, a careful study of the attachment of the Au seeds to the origami is necessary. This would help determine which parameters are most important to increase the seed density. Likely parameters include: Au nanoparticle solution concentration, attachment time, attachment temperature, length of the DNA attachment sequences, and size of the Au nanoparticles. Additionally, the plating solution must be optimized to allow good contact to form between grains.

Another possible way to create highly conductive nanowires is to use the metallized DNA as an etch mask rather than as a wire. By placing a metallized DNA origami on a highly conductive surface, such as graphene or a thin metal film, a subsequent plasma etching process could transfer the DNA origami pattern into the underlying material which would result in higher conductivity nanowires due to the absence of grain boundaries in the underlying film.

Finally, methods must also be developed to integrate semiconducting materials into the correct locations on the DNA origami. Materials such as semiconducting carbon nanotubes have been attached to DNA origami, but not yet integrated into a metallized DNA circuit template.

7.1.3 Local and Global Wiring of DNA Origami Templated Electronics

Connection to DNA origami templated electronic devices will likely need to be accomplished using a top down lithography process. While the semiconductor industry has the capability to align with and connect to existing features extremely precisely when their precise position is known, the ability to connect to origami is complicated by the fact that DNA is not rigid and precise placement has yet to be achieved. These problems can be solved by increasing the rigidity of the origami structures by chemical modification, perfecting surface binding to limit the variability during surface placement, or developing top-down processes which can connect to origami regardless of some variability in positioning.

7.2 Fabrication and modeling of Graphene Based Archival Data Storage Devices

In order for graphene nanofuses to be useful as memory cells for archival data storage, significant work is necessary in the area of growth or deposition of graphene films. The transfer processes which have been used recently are effective for proof-of-concept devices in a research environment. However, these processes are not ideal for large scale integration in a manufacturing environment. The process is long and is difficult to perform without generating defects in the deposited graphene film. Ideally, the graphene film should be able to be directly grown on a substrate that contains reading and programming components. Some work has been done to grow graphene directly on such substrates; however, current processes require extremely high temperatures, which presents problems when growth is done on a substrate that contains electronic devices. Thus more manufacture friendly processes are necessary.

Alternately, some other forms of carbon are highly stable to oxidation and should also be considered for long term data storage devices. Amorphous carbon for example is promising because it is sufficiently conductive and can be deposited using more conventional techniques such as sputtering, evaporation, etc.

To allow estimation of fuse lifetime further stability testing than shown in chapter 5 should be conducted. Testing should be done in more harsh environments consisting of high temperature and humidity.

The programming of nanoscale graphene fuses occurs by oxidation of the graphene as fuses are heated via Joule heating. This means that a source of oxygen must be available during device operation in order for programming to occur. The supply must be large enough so the oxygen concentration does not limit the speed which the fuses can be written or cause errors in the writing process. This can be solved by either having an oxygen source locally available or by development of a packaging technique which will allow a sufficient amount of oxygen to diffuse into the fuse region from the environment. The escape or capture of carbon based gases which are a byproduct of the graphene oxidation process must also be considered in fabrication and packaging processes.

Finally, in order to fabricate high bit density devices, an alternate fuse geometry must be developed where the fuse structure is oriented vertically and locally wired using a crossbar electrode geometry This will allow much higher density device packing. Such a device geometry will result in close spacing between neighboring fuses, close contact with the fuse region and crossbar electrodes. This will cause increased thermal flow into contacts and neighboring fuses. Due to the higher thermal flow outward from the fuse, more power or voltage may be required to heat fuses to sufficient temperatures. Analytical models or finite element

analysis techniques which I have discussed in chapters 5 and 6 will need to be implemented to determine the effect of a higher density geometry on required programming voltages and powers. Each of these analysis techniques will need adjustment based on tighter packed electrodes in order to accurately account for higher thermal flow from fuse regions.

Bibliography

1. Biswas, A., et al. *Advances in Colloid and Interface Science* **2012,** *170*, 2-27.
2. Liddle, J. A.; Gallatin, G. M. *Nanoscale* **2011,** *3*, 2679-2688.
3. Schwierz, F. *Nature Nanotechnology* **2010,** *5*, 487-496.
4. Cheng, J. Y., et al. *Nat. Mater.* **2004,** *3*, 823-828.
5. Torring, T., et al. *Chemical Society Reviews* **2011,** *40*, 5636-5646.
6. Zakharchenko, K. V., et al. *Journal of Physics-Condensed Matter* **2011,** *23*.
7. Liu, L., et al. *Nano Letters* **2008,** *8*, 1965-1970.
8. French, R. H.; Tran, H. V., Immersion Lithography: Photomask and Wafer-Level Materials. In *Annual Review of Materials Research*, Annual Reviews: Palo Alto, 2009; Vol. 39, pp 93-126.
9. 2011 International Technology Roadmap for Semiconductors. http://www.itrs.net/reports.html.
10. Yang, L., et al. *Accounts of Chemical Research* **2005,** *38*, 933-942.
11. Liu, J. F., et al. *Nano Letters* **2002,** *2*, 937-940.
12. Piner, R. D., et al. *Science* **1999,** *283*, 661-663.
13. Rosa, L. G.; Liang, J. *Journal of Physics-Condensed Matter* **2009,** *21*.
14. Shi, J. J., et al. *Journal of the American Chemical Society* **2008,** *130*, 2718-+.
15. Zankovych, S., et al. *Nanotechnology* **2001,** *12*, 91-95.
16. Chou, S. Y., et al. *Appl. Phys. Lett.* **1995,** *67*, 3114-3116.
17. Heuberger, A. *Journal of Vacuum Science & Technology B* **1988,** *6*, 107-121.
18. Gwyn, C. W., et al. *Journal of Vacuum Science & Technology B* **1998,** *16*, 3142-3149.

19. Vieu, C., et al. *Applied Surface Science* **2000,** *164*, 111-117.

20. Mirkin, C. A. *Acs Nano* **2007,** *1*, 79-83.

21. Cheng, J. Y., et al. *Advanced Materials* **2006,** *18*, 2505-2521.

22. Kitano, H., et al. *Langmuir* **2007,** *23*, 6404-6410.

23. Chai, J.; Buriak, J. M. *Acs Nano* **2008,** *2*, 489-501.

24. Black, C. T.; Bezencenet, O. *Ieee Transactions on Nanotechnology* **2004,** *3*, 412-415.

25. Bang, J., et al. *Advanced Materials* **2009,** *21*, 4769-4792.

26. Park, S., et al. *Nano Letters* **2008,** *8*, 1667-1672.

27. Ham, S., et al. *Macromolecules* **2008,** *41*, 6431-6437.

28. Huang, W.-H., et al. *Macromolecules* **2012,** *45*, 1562-1569.

29. Kim, S. H., et al. *Advanced Materials* **2004,** *16*, 226-+.

30. Kim, S. H., et al. *Advanced Materials* **2004,** *16*, 2119-+.

31. Bita, I., et al. *Science* **2008,** *321*, 939-943.

32. Kim, S. O., et al. *Nature* **2003,** *424*, 411-414.

33. Segalman, R. A., et al. *Advanced Materials* **2001,** *13*, 1152-+.

34. Spatz, J. P., et al. *Langmuir* **2000,** *16*, 407-415.

35. Krishnamoorthy, S., et al. *Advanced Functional Materials* **2006,** *16*, 1469-1475.

36. Rothemund, P. W. K. *Nature* **2006,** *440*, 297-302.

37. Douglas, S. M., et al. *Nature* **2009,** *459*, 1154-1154.

38. Pound, E., et al. *Nano Letters* **2009,** *9*, 4302-4305.

39. Balandin, A. A. *Nat. Mater.* **2011,** *10*, 569-581.

40. Cai, W., et al. *Nano Letters* **2010,** *10*, 1645-1651.

41. Soldano, C., et al. *Carbon* **2010,** *48*, 2127-2150.

42. Huang, P. Y., et al. *Nature* **2011,** *469*, 389-+.

43. Yang, J. K. W., et al. *Nature Nanotechnology* **2010,** *5*, 256-260.

44. Kershner, R. J., et al. *Nature Nanotechnology* **2009,** *4*, 557-561.

45. Gerdon, A. E., et al. *Small* **2009,** *5*, 1942-1946.

46. Ding, B., et al. *Nano Letters* **2010,** *10*, 5065-5069.

47. Douglas, S. M., et al. *Proc. Natl. Acad. Sci. U. S. A.* **2007,** *104*, 6644-6648.

48. Krishnamoorthy, S., et al. *Materials Today* **2006,** *9*, 40-47.

49. Stoykovich, M. P., et al. *Acs Nano* **2007,** *1*, 168-175.

50. Cheng, J. Y., et al. *Advanced Materials* **2008,** *20*, 3155-3158.

51. Glass, R., et al. *Nanotechnology* **2003,** *14*, 1153-1160.

52. Herne, T. M.; Tarlov, M. J. *Journal of the American Chemical Society* **1997,** *119*, 8916-8920.

53. Akbulut, O., et al. *Nano Letters* **2007,** *7*, 3493-3498.

54. Ding, B. Q., et al. *Journal of the American Chemical Society* **2010,** *132*, 3248-3249.

55. Hung, A. M., et al. *Nature Nanotechnology* **2010,** *5*, 121-126.

56. Kastle, G., et al. *Advanced Functional Materials* **2003,** *13*, 853-861.

57. Ono, L. K.; Cuenya, B. R. *J. Phys. Chem. C* **2008,** *112*, 4676-4686.

58. Boyen, H. G., et al. *Phys. Rev. Lett.* **2005,** *94*.

59. Park, C., et al. *Polymer* **2003,** *44*, 6725-6760.

60. Bosworth, J. K., et al. *Acs Nano* **2008,** *2*, 1396-1402.

61. Lohmuller, T., et al. *Biointerphases* **2011,** *6*, MR1-MR12.

62. Chai, J. A., et al. *Proc. Natl. Acad. Sci. U. S. A.* **2010,** *107*, 20202-20206.

63. Fu, Q., et al. *Applied Organometallic Chemistry* **2010,** *24*, 569-572.

64. Pearson, A. C., et al. *Nano Letters* **2011,** *11*, 1981-1987.

65. Mela, P., et al. *Small* **2007,** *3*, 1368-1373.

66. Aydin, D., et al. *Small* **2009,** *5*, 1014-1018.

67. Yun, S. H., et al. *Nanotechnology* **2006,** *17*, 450-454.

68. Arpin, K. A., et al. *Soft Matter* **2011,** *7*, 10252-10257.

69. Yap, F. L.; Krishnamoorthy, S. *J. Mater. Chem.* **2010,** *20*, 10211-10216.

70. Li, H. Y., et al. *Materials Today* **2009,** *12*, 24-32.

71. Becerril, H. A.; Woolley, A. T. *Chemical Society Reviews* **2009,** *38*, 329-337.

72. Andersen, E. S., et al. *Acs Nano* **2008,** *2*, 1213-1218.

73. Han, D. R., et al. *Science* **2011,** *332*, 342-346.

74. Andersen, E. S., et al. *Nature* **2009,** *459*, 73-U75.

75. Pinheiro, A. V., et al. *Nature Nanotechnology* **2011,** *6*, 763-772.

76. Ke, Y. G., et al. *Science* **2008,** *319*, 180-183.

77. Kuzuya, A., et al. *Chembiochem* **2009,** *10*, 1811-1815.

78. Chhabra, R., et al. *Journal of the American Chemical Society* **2007,** *129*, 10304-+.

79. Rinker, S., et al. *Nature Nanotechnology* **2008,** *3*, 418-422.

80. Kuzyk, A., et al. *Nanotechnology* **2009,** *20*.

81. Maune, H. T., et al. *Nature Nanotechnology* **2010,** *5*, 61-66.

82. Pal, S., et al. *Angew. Chem.-Int. Edit.* **2010,** *49*, 2700-2704.

83. Sharma, J., et al. *Journal of the American Chemical Society* **2008,** *130*, 7820.

84. Zheng, J. W., et al. *Nano Letters* **2006,** *6*, 1502-1504.

85. Ozbay, E. *Science* **2006,** *311*, 189-193.

86. Tan, S. J., et al. *Nature Nanotechnology* **2011,** *6*, 268-276.

87. Gu, Q., et al. *Nanotechnology* **2006,** *17*, R14-R25.

88. Braun, E., et al. *Nature* **1998,** *391*, 775-778.

89. Richter, J., et al. *Appl. Phys. Lett.* **2001,** *78*, 536-538.

90. Deng, Z. X.; Mao, C. D. *Nano Letters* **2003,** *3*, 1545-1548.

91. Liu, J. F., et al. *Acs Nano* **2011,** *5*, 2240-2247.

92. Geng, Y. L., et al. *J. Mater. Chem.* **2011,** *21*, 12126-12131.

93. Pilo-Pais, M., et al. *Nano Letters* **2011,** *11*, 3489-3492.

94. Schreiber, R., et al. *Small* **2011,** *7*, 1795-1799.

95. Loweth, C. J., et al. *Angew. Chem.-Int. Edit.* **1999,** *38*, 1808-1812.

96. Tinland, B., et al. *Macromolecules* **1997,** *30*, 5763-5765.

97. Satti, A., et al. *Chem. Mat.* **2007,** *19*, 1543-1545.

98. Brown, K. R.; Natan, M. J. *Langmuir* **1998,** *14*, 726-728.

99. Aherne, D., et al. *Nanotechnology* **2007,** *18*.

100. Park, S., et al. *Journal of the American Chemical Society* **2004,** *126*, 11772-11773.

101. Ongaro, A., et al. *Chem. Mat.* **2005,** *17*, 1959-1964.

102. Oliver Slattery, et al. *J. Res. Natl. Inst. Stand. Technol.* **2005,** *109*, 517-524.

103. S. A. Dobrusina, S. I. G., I. G. Tikhonova, T. D. Velikova and P. E. Zavalishin *Sci. Tech. Inf. Process* **2007,** *34*, 258-263.

104. J. S. Judge, et al. 20th IEEE/11th

NASA Goddard Conference on Mass Storage Systems and Technologies, San Diego, CA, April 7-10, 2003; San Diego, CA, 2003.

105. Abbott, J., et al. *ACS Appl. Mater. Interfaces* **2010,** *2*, 2373-2376.

106. Dong, G., et al. *Ieee Transactions on Circuits and Systems I-Regular Papers* **2011,** *58*, 429-439.

107. Li, S.; Zhang, T. *Ieee Transactions on Very Large Scale Integration (Vlsi) Systems* **2010,** *18*, 1412-1420.

108. Wang, Z., et al. *Ieee Transactions on Very Large Scale Integration (Vlsi) Systems* **2012,** *20*, 1221-1234.

109. Klove, T., et al. *Ieee Transactions on Information Theory* **2011,** *57*, 4477-4487.

110. Smith, S.; Forrest, S. R. *Appl. Phys. Lett.* **2004,** *84*, 5019-5021.

111. Moller, S., et al. *Nature* **2003,** *426*, 166-169.

112. Moller, S., et al. *Journal of Applied Physics* **2003,** *94*, 7811-7819.

113. Yi, M., et al. *Journal of Applied Physics* **2011,** *110*.

114. Kulkarni, S. H., et al. *IEEE J. Solid-State Circuit* **2010,** *45*, 863-868.

115. Norm Robson, et al. IEEE 2007 Custom Integrated Circuits Conference (CICC), San Jose, California, San Jose, California, 2007.

116. Zhu, W., et al. *Ieee Transactions on Electron Devices* **2011,** *58*, 960-965.

117. Franklin, P.; Burgess, D. Reliability Physics Symposium, 1974. 12th Annual, April 1974; 1974; pp 82-86.

118. Lambert, D., et al. Reliability Physics Symposium Proceedings, 2004. 42nd Annual. 2004 IEEE International, 25-29 April 2004; 2004; pp 543-546.

119. Alavi, M., et al. Electron Devices Meeting, 1997. IEDM '97. Technical Digest., International, 7-10 Dec 1997; 1997; pp 855-858.

120. Don, P., et al. Semiconductor Manufacturing, 2005. ISSM 2005, IEEE International Symposium on, 13-15 Sept. 2005; 2005; pp 420-421.

121. Geim, A. K. *Science* **2009,** *324*, 1530-1534.

122. Standley, B., et al. *Nano Letters* **2008,** *8*, 3345-3349.

123. Wang, X.; Dai, H. *Nature Chemistry* **2010,** *2*, 661-665.

124. Mohsen Alavi , et al. IEEE International Electron Devices Meeting, Dec. 1997; 1997; pp 855-858.